PROBING THE FORMATION OF MAMMALIAN CELL LIPID MICRODOMAINS WITH NANOMETER-SCALE IMAGING SECONDARY ION MASS SPECTROMETRY

BY

HALEY ANN KLITZING

DISSERTATION

Submitted in partial fulfillment of the requirements
for the degree of Doctor of Philosophy in Chemistry
in the Graduate College of the
University of Illinois at Urbana-Champaign, 2015

Urbana, Illinois

Doctoral Committee:

Associate Professor Mary L. Kraft, Chair
Associate Professor Ryan C. Bailey
Assistant Professor Brendan Harley
Professor Jonathan V. Sweedler

ABSTRACT

Over forty years ago, Singer and Nicholson began studying the organization of the plasma membranes on mammalian cells. Since then, our understanding of this membrane has shifted from that of a homogeneous to a more heterogenous environment of proteins and lipids. The complexity of living cells have made for difficulties in obtaining a complete understanding of the plasma membrane, especially that of the sphingolipids' organization.

The recent application of imaging mass spectrometry to biological samples has enabled for the chemical analysis of the plasma membrane. Through the use of a high resolution imaging secondary ion mass spectrometer (NanoSIMS 50, Cameca), we have been able to chemically map the distributions of sphingolipids on the plasma membrane of murine fibroblast cells with an astonishing sub-100 nm resolution. This required us to metabolically incorporate a rare, stable label into the molecules of interest and chemically preserving the cells in an effort to maintain close to a native organization of the membrane. The labeled lipid species could then be visualized with the NanoSIMS, providing us with a closer understanding of lipids within the plasma membrane.

These experiments have revealed that sphingolipid-enriched domains exist in the plasma membrane on a length scale of ~200 nm, and they form non-random clustering on the cell surface. Disruption of the cellular cytoskeleton resulted in a loss of detectable statistically significant domains. In addition, the rapid transport of sphingolipids to the plasma membrane has made for complex interpretation of the role that vesicle transport plays in domain formation. Further studies using this methodology of chemically imaging mammalian cells, most importantly disruption of vesicle trafficking, may help to definitively identify the mechanisms

behind the formation of these lipid domains as well as elucidate the full purpose they serve in the cell.

ACKNOWLEDGEMENTS

I owe a great deal of thanks to Professor Scott "Doc" Luaders at Quincy University for helping me to fully understand chemistry when my high school teacher had failed me. Further thanks goes to Doc for encouraging me to change my major and pursue a graduate degree in Chemistry.

Many thanks go to my advisor, Professor Mary Kraft, for taking me into her lab and providing me with an environment of thought provoking, if not often frustrating, research. I could not have asked for a better advisor to help lead me through my doctoral career.

Thanks also goes to my labmates, both past and present: to Dr. Kaiyan Lou and Dr. Robbie Wilson for their help with my projects; to Dr. Chris Anderton for his much needed conversations and ponderings of life; to Dr. Jessica Frisz for being a wonderful teacher and the best roommate one could ask for during our days away at Lawrence Livermore National Laboratory; to Bill Hanafin for his teaching ways and his unbending desire to help; to Rayna Kim for always being a calming, logical presence in the lab; to Vahid "Vee-haad" Mirshafiee for becoming like a loveable brother with whom I could kid-around with in the lab; to Ashley "Oshley" Yeager for the ever present discussions ranging from television to research and for sharing in the "Livermore" experience; and to Yelena Ilin and Brent Denton for making the lab a more enjoyable environment by being wonderfully friendly people, and for successfully allowing me avoid speaking to undergraduates during poster sessions.

Thank you to my closest friends, Diana Kinkelaar, Hannah Kennedy, and Nicole Mette, for always being supportive, encouraging, and lending an ear when I needed to vent and seek worldly advice. Thanks to my family for being equally supportive, for providing me with my very first sources of education, and for shaping me into the person I've become today.

And finally, I would like to thank the many staff members who have helped me along during my PhD career. In particular, I want to thank Julie Sides and Becky Duffield for being extremely helpful and knowledgeable; Professor Alexander Scheeline for his support and advice during my first years of graduate school attendance; to Vania Petrova and Tim Spila at the Frederick Seitz Materials Research Laboratory for their teaching and help with instrumentation; and to Drs. Peter Weber and Ian Hutcheon at Lawrence Livermore National Lab for allowing us access to their laboratory and equipment that enabled our work.

R.I.P. Dr. Alpha Mac ‘n Cheese Fish, DVM. You were the best betta fish a lab could ask for, always a pleasure to gaze upon, and always offered valuable research insight. Your replacement, Forrest, leaves much to be desired.

“That’s what.” ~She

TABLE OF CONTENTS

CHAPTER 1.
INTRODUCTION[1]

The Plasma Membrane

The plasma membrane is the outermost structure of mammalian cells. It is involved in many key cell functions including cell-cell recognition, signal transduction, and nutrient uptake.[2–6] The plasma membrane is comprised of a lipid bilayer that contains hundreds of different lipid species, sterols, proteins, and complex carbohydrates. Because of the membrane's importance in multiple cellular processes, many studies have focused on elucidating plasma membrane organization and how this organization changes in response to internal and external stimuli, such as protein signaling, cholesterol depletion, and mutations in integral membrane proteins.[7–10]

The fluid mosaic model was one of the initial guiding principles for understanding cell membrane organization. Singer and Nicolson described the membrane as a two-dimensional fluid in which components freely diffuse in the lateral direction, implying homogeneous mixing.[5] This concept of homogeneous mixing was contradicted by the finding that lipid composition within viral envelopes often differed from that of the host cell.[11] Enveloped viruses, such as influenza, are coated with a portion of the host cell's plasma membrane when they bud from the host cell. If the lipid composition of the host cell's plasma membrane was homogeneous, as suggested by the fluid mosaic model, then the resulting viral envelope should have a more representative lipid composition of the host cell. Biochemical analysis, however, indicated that

[1] This chapter features portions of work which originally appeared in a published manuscript[1] and has been reprinted with permissions from:
Molecular and Cell Biology of Lipids. Kraft, M. L.; Klitzing, H. A. Imaging Lipids with Secondary Ion Mass Spectrometry. *Biochim. Biophys. Acta BBA - Mol. Cell Biol. Lipids* **2014**, *1841* (8), 1108–1119. Both Mary L. Kraft and Haley A. Klitzing contributed to writing the manuscript.

the influenza viral envelopes are enriched with sphingolipids and cholesterol when compared to the bulk membrane of the host cell.[12,13] These results, among other, have led to the hypothesis that there are regions within the plasma membrane, often referred to as lipid rafts, which are cholesterol and sphingolipid enriched.[14] Since then, a growing body of data suggests that cholesterol- and sphingolipid-rich domains play important roles in many other processes, including protein recruitment, signal transduction, intracellular sorting, and viral entry, assembly, and budding.[4,6,13,15,16] These domains are believed to form due to energetically favorable interactions (in the form of hydrogen bond formation) between certain membrane proteins and lipid species, specifically cholesterol and sphingolipids.[3,13,14,16–20] Despite their importance, compositionally distinct lipid domains remain controversial because it is necessary to unambiguously detect /visualize these microdomains in order to test either hypothesis.

The abundances and distributions of various lipid species within tissues and cells are linked to both health and disease.[21–25,25–27] In mammalian cells, lipids are not only the building blocks of cellular membranes, but they also function as ligands that selectively bind to and regulate the activity of certain protein components in signaling pathways.[28–37] This is especially true of sphingolipids, as ceramide, the product of sphingomyelin hydrolysis, is involved in the signaling pathways that regulate apoptosis, cytoskeletal reorganization, and other important cellular processes.[23,38–41]

The three most prominent hypotheses for sphingolipid domain formation in the plasma membrane involve protein-lipid interactions, intracellular transport of materials to the cell surface, and diffusional barriers due to the cell's actin cytoskeleton. As mentioned above, the protein-lipid interaction hypothesis suggests that certain membrane proteins and specific lipid species, namely sphingolipids and cholesterol, have energetically favorable interactions that

result in the formation of compositionally distinct lipid microdomains.[3,13,14,16–20] Second, the intracellular transport of vesicles composed of newly synthesized sphingolipids and membrane proteins to the cell surface is hypothesized to result in membrane domains that are enriched with the vesicle's cargo. The lifetime of the resulting compositionally distinct lipids domains may be very short unless the lateral diffusion of lipid components away from the fusion site is obstructed.[3,9,16,42–44] The third hypothesis for compositionally distinct membrane domain formation involves the cellular cytoskeleton, which is the protein network that underlies the plasma membrane. The cytoskeleton is composed of actin filaments, and it gives the cell its shape and support, assists in cell movement, and participates in creating cell-cell junctions.[45,46] The actin cytoskeleton is hypothesized to hinder the lateral diffusion of proteins and lipids within the plasma membrane, and thereby stabilize compositionally distinct lipid microdomains that form in the plasma membrane due to membrane trafficking or selective protein-lipid or lipid-lipid interactions.[2,16,19,42,46–49] When the research reported in this thesis was initiated, there is no consensus on the extent to which each mechanism contributes to lipid domain formation, as the indirect methods used to detect lipid domains have produced various and often conflicting results.

Imaging Lipid Distribution in Membranes

Insight into lipid metabolism, transport, and function has been acquired by studying their distributions within tissues and cells. The locations and abundances of various lipid species are often probed by using fluorescent lipid analogs, lipophilic dyes, or lipid-specific functionalized antibodies that can be detected with light, fluorescence, or electron microscopy.[50–54] The distributions of various lipid species in biological samples can also be mapped with high

chemical specificity and without the use of complex labels, such as fluorophores or antibodies, with imaging mass spectrometry.

Matrix-assisted laser desorption ionization (MALDI) is perhaps the most popular imaging mass spectrometry technique that has been used to analyze biological samples. As the name implies, the sample is coated with a matrix that promotes biomolecule desorption and ionization, and a laser is used to ionize the molecules within its focal area. This ionization process minimizes molecular fragmentation, enabling the detection of molecular ions with high mass-to-charge ratios (m/z 500–20,000).[55,56] MALDI has been used to image a wide range of biomolecules, including lipids and proteins, with a lateral resolution that is typically > 10 μm and a sampling depth in the micron range.[56–61] This spatial resolution renders MALDI imaging appropriate for analyzing the lipid distributions within tissues. MALDI imaging of biomolecules, including lipids, in tissues has been the subject of recent reviews[55,57,62–64] and will not be discussed further herein.

This dissertation will focus on a complementary imaging mass spectrometry technique, secondary ion mass spectrometry (SIMS). SIMS offers higher spatial resolution than MALDI, but typically at the expense of higher molecular fragmentation, which results in lower chemical specificity. SIMS can achieve the sub-micrometer lateral resolution that enables studying the lipid distribution within a single cell. Moreover, the analysis depth of SIMS is ultimately limited by the escape depth of the secondary ions, which is generally limited to the upper one to two monolayers of the sample.[65] Thus, when performed at the surface of the sample, SIMS has the shallow sampling depth (top $\leq$ 5 nm) that permits imaging the lipids in the plasma membrane with little interference from intracellular membranes.

SIMS Techniques

SIMS imaging of lipids has been primarily performed using two different types of instrumentation, time-of-flight SIMS (TOF-SIMS) and magnetic sector SIMS with high lateral resolution. Both TOF-SIMS and high-resolution magnetic sector SIMS are performed under ultra-high vacuum (UHV), which is the techniques' greatest limitation. During analysis, a focused primary ion beam sputters neutral and ionized molecules and molecular fragments from the surface of the sample. This primary ion beam is scanned across the sample, and the secondary ions that are ejected at each beam position are collected. The intensities of the secondary ions that are characteristic of specific components are then used to create a map of that component's distribution on the surface of the sample. Additionally, because material is sputtered from the surface of the sample during SIMS analysis, maps of component distribution at progressively increasing depth in the sample can be generated by repeatedly acquiring SIMS images at the same sample location. When depth profiling is performed with TOF-SIMS, a sputtering scan that removes the damaged material is often inserted after each imaging scan in order to reduce the fragmentation of the species detected during image acquisition.

The intensities of the secondary ions detected at each pixel are affected by the concentration of the parent molecule that produced the secondary ions, as well as by concentration-independent factors.[66–74] The first concentration-independent factor, which is referred to as matrix effects, arises because the local chemical environment affects the probability that a species will become ionized.[66–71] The second concentration-independent factor is sample topography; differences in the incidence angle of the primary ion beam affect both the absolute and relative intensities of the ions.[72,73] These concentration-independent variations in ion intensity complicate quantitatively imaging lipid distribution with either TOF-SIMS or high-

resolution magnetic sector SIMS. Normalization methods have been developed to minimize these concentration-independent variations and produce a SIMS signal whose intensity is proportional to the concentration of the analyte. TOF-SIMS and high-resolution magnetic sector SIMS instruments differ in the configurations of their ion optics, primary ion sources, and mass analyzers (Table 1.1). These differences impart each approach with complementary strengths and weaknesses. In the following sections, a closer look will be taken of these imaging methods.

TOF-SIMS

TOF-SIMS instruments typically employ a pulsed primary ion beam that is oriented with oblique incidence to the plane of the sample.[62] The secondary ions that are ejected from the sample are then collected by a TOF mass analyzer that generates a mass spectrum at each pixel. The spectra can have a mass range of 1 to 1500 *m*/*z*, but the ion counts generally decrease with increasing mass due to fragmentation. Variations in the secondary ion signal intensity that are caused by matrix effects and sample topography can be reduced, but not eliminated, by normalizing the counts of the signal of interest to that of an abundant ion or all of the ions detected at the same pixel.[75,76] The collection of a mass spectrum at every pixel is advantageous because it negates the need for labels, as any unlabeled molecule that produces secondary ions with distinctive *m*/*z* can be detected and imaged. Other advantages are that multiple components of interest can be imaged in parallel, and the spectra contain information about both known and unknown components that are present in the sample.

The lateral resolution of any SIMS technique is ultimately limited by the diameter of the primary ion beam, which can be 200 nm or less, depending on the instrument. However, for imaging lipids with TOF-SIMS, the working lateral resolution is often larger than the beam diameter because the numbers of lipid-specific secondary ions detected at each beam position are

insufficient for resolving features in an image.[77] Therefore, TOF-SIMS analyses must be optimized to increase the ejection of secondary ions that are characteristic of each lipid species of interest. Intact molecular ion species are most useful for this purpose. To maximize the detection of intact molecular ions and reduce the ejection of fragment ions from the sample, the amount of chemical damage at the surface of the sample must be minimized. Note that the term chemical damage is used to refer to molecular fragmentation, and does not refer to structural reorganization at length scales that are accessible to detection with SIMS. A common approach for minimizing molecular fragmentation is to limit the primary ion dose so that each primary ion impacts a pristine region on the sample, and not a region where the molecules were already fragmented by collision with a primary ion[78,79] This is referred to as static SIMS analysis, where the static limit is typically estimated to be below 10^{13} ions/cm^2.[79,80] Even when TOF-SIMS is performed under static conditions, molecular fragmentation can limit the selectivity and working lateral resolution of lipid imaging. When this occurs, fragment ions that are common to multiple species from a common lipid class, such as the phosphocholine headgroup-containing ions at *m*/*z* 184 $[C_5H_{15}NPO_4]^+$ and 224 $[C_8H_{19}NPO_4]^+$, can be detected to achieve a working lateral resolution ≤ 1 μm.[76,81,82] However, lipids from the same class cannot be discriminated by these fragment ions. Several strategies have been developed to increase the detection of secondary ion signals that are useful for lipid identification including the use of cluster ion sources,[71–84] processing with multivariate analysis techniques,[83–102] and the use of MALDI matrices.[103–109]

Given the current capabilities of TOF-SIMS, this approach is most advantageous for detecting, identifying, and imaging multiple unlabeled lipids, including those with unknown structures, within tissues. TOF-SIMS imaging of lipids in individual cells is possible, though detection is now typically limited to the most abundant lipid species and a lateral resolution

≥ 1 μm. This lateral resolution was not expected to be sufficient for assessing cholesterol and sphingolipid distribution in the plasma membrane, so we opted for the following approach.

High-Resolution Magnetic Sector SIMS Performed with a Cameca NanoSIMS 50

An alternative strategy to overcoming the low yields of component-specific secondary ions that limit the working lateral resolution is to exploit the higher-yielding monoatomic and diatomic ions for component detection. This strategy is implemented in a commercial magnetic sector SIMS instrument, the Cameca NanoSIMS 50(L). SIMS performed with this instrument is often referred to as high-resolution SIMS or NanoSIMS.

The NanoSIMS differs from conventional TOF-SIMS instruments in a few ways. First, it reveals the elemental and isotopic compositions in a sample by detecting monoatomic and diatomic secondary ions, which have higher yields than the molecular ions and high mass fragment ions used for TOF-SIMS analysis. Second, the NanoSIMS employs co-axial optics to direct the primary and secondary ions, which must have opposite polarities. The advantage of the co-axial configuration is it enables a shorter working distance, which simultaneously enhances focusing the reactive primary ions (Cs^+ or O^-) onto the sample and extracting the resulting secondary ions (Fig. 1.1). Instead of acquiring a complete mass spectrum, monoatomic and diatomic secondary ions with up to five or seven (depending on the NanoSIMS model) different *m*/*z* ratios are detected in parallel by a magnetic sector mass spectrometer that can differentiate isobars of the same nominal mass (i.e., $^{12}C^{15}N^-$, 26.9996 amu; and $^{13}C^{14}N^-$, 27.0059 amu can be separated). The intensities of the ions detected at each beam position are used to construct a map of the elemental and isotopic compositions of the sample's surface. The microcesium primary ion source developed by Cameca enables imaging negative secondary ions with a lateral resolution as good as 30 nm.[110] However, the working lateral resolution achieved for imaging lipids in

membranes is typically around 100 nm due to the relatively low secondary ion counts obtained when biological samples are analyzed with small diameter primary ion beams that have low currents.

Because monoatomic and diatomic secondary ions are collected by the NanoSIMS, the molecules of interest must contain a distinct element or isotope so that they produce elementally or isotopically distinct secondary ions that can be used for component identification.[111,112] To detect and image lipids, labeling with distinct stable isotopes is advantageous because the isotope-labeled lipid has the same chemical structure as the unlabeled native lipid molecule. This helps to ensure that the labeling will not alter the molecular interactions or intracellular trafficking that may contribute to lipid distribution in the sample. For studies of model lipid membranes, lipids that contain stable isotope labels can be obtained from commercial sources or synthesized with chemical methods. To image specific lipid species within cellular membranes, metabolic labeling must be used to selectively incorporate distinct stable isotopes into the lipid species of interest within living cells.

NanoSIMS instruments are optimized for imaging with at high primary ion doses ($> 10^{15}$ ions/cm^2) that erode the sample surface. This mode of operation, which is called dynamic SIMS, enables the rapid acquisition of depth profiles. However, for the analysis of lipid distribution in the plasma membrane, the vast majority of secondary ions that are collected from the surface of the cell must be produced by the cell membrane, and few secondary ions should be collected from the underlying cytoplasm. This necessitates restricting the sputtering depth so it is less than the thicknesses of the plasma membrane (7.5 nm).[113]

The lateral resolution, sensitivity, and need for elemental or distinctive isotope-labels for lipid identification render NanoSIMS most advantageous for imaging a small number of known

lipid targets that can be metabolically or chemically labeled with stable isotopes, and high (~ 100 nm) lateral resolution is required. Its primary drawbacks are the need for isotope labels, only a limited number of lipid species can be imaged in parallel, and the cost of the NanoSIMS 50(L) instrument limits its availability.

The work described in this dissertation relates to the development and use of NanoSIMS techniques for studying lipids and their formation of domains in the plasma membrane.

References

(1) *T*his research was originally published in *Biochimica et Biophysica Acta (BBA) - Molecular and Cell Biology of Lipids*. Kraft, M. L.; Klitzing, H. A. Imaging Lipids with Secondary Ion Mass Spectrometry. *Biochim. Biophys. Acta BBA - Mol. Cell Biol. Lipids* **2014**, *1841* (8), 1108–1119.

(2) Doherty, G. J.; McMahon, H. T. Mediation, Modulation, and Consequences of Membrane-Cytoskeleton Interactions. *Annu. Rev. Biophys.* **2008**, *37* (1), 65–95.

(3) Holthuis, J. C. M.; Levine, T. P. Lipid Traffic: Floppy Drives and a Superhighway. *Nat. Rev. Mol. Cell Biol.* **2005**, *6* (3), 209–220.

(4) Shaw, J. E.; Epand, R. F.; Epand, R. M.; Li, Z.; Bittman, R.; Yip, C. M. Correlated Fluorescence-Atomic Force Microscopy of Membrane Domains: Structure of Fluorescence Probes Determines Lipid Localization. *Biophys. J.* **2006**, *90* (6), 2170–2178.

(5) Singer, S. J.; Nicolson, G. L. The Fluid Mosaic Model of the Structure of Cell Membranes. *Science* **1972**, *175* (4023), 720–731.

(6) Zhang, J.; Pekosz, A.; Lamb, R. A. Influenza Virus Assembly and Lipid Raft Microdomains: A Role for the Cytoplasmic Tails of the Spike Glycoproteins. *J. Virol.* **2000**, *74* (10), 4634–4644.

(7) Eggeling, C.; Ringemann, C.; Medda, R.; Schwarzmann, G.; Sandhoff, K.; Polyakova, S.; Belov, V. N.; Hein, B.; von Middendorff, C.; Schoenle, A.; et al. Direct Observation of the Nanoscale Dynamics of Membrane Lipids in a Living Cell. *Nature* **2009**, *457* (7233), 1159–U121.

(8) Shnyrova, A. V.; Frolov, V. A.; Zimmerberg, J. Domain-Driven Morphogenesis of Cellular Membranes. *Curr. Biol.* **2009**, *19* (17), R772–R780.

(9) Simons, K.; Toomre, D. Lipid Rafts and Signal Transduction. *Nat. Rev. Mol. Cell Biol.* **2000**, *1* (1), 31–39.

(10) Takeda, M.; Leser, G. P.; Russell, C. J.; Lamb, R. A. Influenza Virus Hemagglutinin Concentrates in Lipid Raft Microdomains for Efficient Viral Fusion. *Proc. Natl. Acad. Sci.* **2003**, *100* (25), 14610–14617.

(11) Van Meer, G.; Simons, K. Viruses Budding from Either the Apical or the Basolateral Plasma Membrane Domain of MDCK Cells Have Unique Phospholipid Compositions. *EMBO J.* **1982**, *1* (7), 847–852.

(12) Keller, P.; Simons, K. Cholesterol Is Required for Surface Transport of Influenza Virus Hemagglutinin. *J. Cell Biol.* **1998**, *140* (6), 1357–1367.

(13) Scheiffele, P.; Rietveld, A.; Wilk, T.; Simons, K. Influenza Viruses Select Ordered Lipid Domains during Budding from the Plasma Membrane. *J. Biol. Chem.* **1999**, *274* (4), 2038–2044.

(14) Simons, K.; Ikonen, E. Functional Rafts in Cell Membranes. *Nature* **1997**, *387* (6633), 569–572.

(15) Boxer, S. G.; Kraft, M. L.; Weber, P. K. Advances in Imaging Secondary Ion Mass Spectrometry for Biological Samples. *Annu. Rev. Biophys.* **2009**, *38*, 53–74.

(16) Fan, J.; Sammalkorpi, M.; Haataja, M. Formation and Regulation of Lipid Microdomains in Cell Membranes: Theory, Modeling, and Speculation. *FEBS Lett.* **2010**, *584* (9), 1678–1684.

(17) Lingwood, D.; Simons, K. Lipid Rafts As a Membrane-Organizing Principle. *Science* **2010**, *327* (5961), 46–50.

(18) Allen, J. A.; Halverson-Tamboli, R. A.; Rasenick, M. M. Lipid Raft Microdomains and Neurotransmitter Signalling. *Nat. Rev. Neurosci.* **2007**, *8* (2), 128–140.

(19) Lenne, P.-F.; Wawrezinieck, L.; Conchonaud, F.; Wurtz, O.; Boned, A.; Guo, X.-J.; Rigneault, H.; He, H.-T.; Marguet, D. Dynamic Molecular Confinement in the Plasma Membrane by Microdomains and the Cytoskeleton Meshwork. *EMBO J.* **2006**, *25* (14), 3245–3256.

(20) Nicolau, D. V.; Burrage, K.; Parton, R. G.; Hancock, J. F. Identifying Optimal Lipid Raft Characteristics Required To Promote Nanoscale Protein-Protein Interactions on the Plasma Membrane. *Mol. Cell. Biol.* **2006**, *26* (1), 313–323.

(21) Park, T.-S.; Rosebury, W.; Kindt, E. K.; Kowala, M. C.; Panek, R. L. Serine Palmitoyltransferase Inhibitor Myriocin Induces the Regression of Atherosclerotic Plaques in Hyperlipidemic ApoE-Deficient Mice. *Pharmacol. Res.* **2008**, *58* (1), 45–51.

(22) Bismuth, J.; Lin, P.; Yao, Q.; Chen, C. Ceramide: A Common Pathway for Atherosclerosis? *Atherosclerosis* **2008**, *196* (2), 497–504.

(23) Zeidan, Y. H.; Jenkins, R. W.; Hannun, Y. A. Remodeling of Cellular Cytoskeleton by the Acid Sphingomyelinase/ceramide Pathway. *J. Cell Biol.* **2008**, *181* (2), 335–350.

(24) Reagan, J. W.; Hubbert, M. L.; Shelness, G. S. Posttranslational Regulation of Acid Sphingomyelinase in Niemann-Pick Type C1 Fibroblasts and Free Cholesterol-Enriched Chinese Hamster Ovary Cells. *J. Biol. Chem.* **2000**, *275* (48), 38104–38110.

(25) Kolter, T.; Sandhoff, K. Sphingolipid Metabolism Diseases. *Biochim. Biophys. Acta BBA - Biomembr.* **2006**, *1758* (12), 2057–2079.

(26) Hajduch, E.; Balendran, A.; Batty, I. H.; Litherland, G. J.; Blair, A. S.; Downes, C. P.; Hundal, H. S. Ceramide Impairs the Insulin-Dependent Membrane Recruitment of Protein Kinase B Leading to a Loss in Downstream Signalling in L6 Skeletal Muscle Cells. *Diabetologia* **2001**, *44* (2), 173–183.

(27) Ghosh, N.; Patel, N.; Jiang, K.; Watson, J. E.; Cheng, J.; Chalfant, C. E.; Cooper, D. R. Ceramide-Activated Protein Phosphatase Involvement in Insulin Resistance via Akt, Serine/Arginine-Rich Protein 40, and Ribonucleic Acid Splicing in L6 Skeletal Muscle Cells. *Endocrinology* **2007**, *148* (3), 1359–1366.

(28) Hannun, Y. A.; Obeid, L. M. Principles of Bioactive Lipid Signalling: Lessons from Sphingolipids. *Nat. Rev. Mol. Cell Biol.* **2008**, *9* (2), 139–150.

(29) Lucki, N. C.; Sewer, M. B. Nuclear Sphingolipid Metabolism. *Annu. Rev. Physiol.* **2012**, *74* (1), 131–151.

(30) Chipuk, J. E.; McStay, G. P.; Bharti, A.; Kuwana, T.; Clarke, C. J.; Siskind, L. J.; Obeid, L. M.; Green, D. R. Sphingolipid Metabolism Cooperates with BAK and BAX to Promote the Mitochondrial Pathway of Apoptosis. *Cell* **2012**, *148* (5), 988–1000.

(31) Hait, N. C.; Allegood, J.; Maceyka, M.; Strub, G. M.; Harikumar, K. B.; Singh, S. K.; Luo, C.; Marmorstein, R.; Kordula, T.; Milstien, S.; et al. Regulation of Histone Acetylation in the Nucleus by Sphingosine-1-Phosphate. *Science* **2009**, *325* (5945), 1254–1257.

(32) Bieberich, E. Ceramide in Stem Cell Differentiation and Embryo Development: Novel Functions of a Topological Cell-Signaling Lipid and the Concept of Ceramide Compartments. *J. Lipids* **2010**, *2011*, e610306.

(33) Romanenko, V. G.; Rothblat, G. H.; Levitan, I. Modulation of Endothelial Inward-Rectifier K+ Current by Optical Isomers of Cholesterol. *Biophys. J.* **2002**, *83* (6), 3211–3222.

(34) Wang, P.; Liu, P.; Weng, J.; Sontag, E.; Anderson, R. G. W. A Cholesterol-regulated PP2A/HePTP Complex with Dual Specificity ERK1/2 Phosphatase Activity. *EMBO J.* **2003**, *22* (11), 2658–2667.

(35) Wang, P.; Weng, J.; Anderson, R. G. W. OSBP Is a Cholesterol-Regulated Scaffolding Protein in Control of ERK1/2 Activation. *Science* **2005**, *307* (5714), 1472–1476.

(36) Wang, P.-Y.; Weng, J.; Lee, S.; Anderson, R. G. W. The N Terminus Controls Sterol Binding While the C Terminus Regulates the Scaffolding Function of OSBP. *J. Biol. Chem.* **2008**, *283* (12), 8034–8045.

(37) Burger, K.; Gimpl, G.; Fahrenholz, F. Regulation of Receptor Function by Cholesterol. *Cell. Mol. Life Sci. CMLS* **2000**, *57* (11), 1577–1592.

(38) Adada, M.; Canals, D.; Hannun, Y. A.; Obeid, L. M. Sphingolipid Regulation of Ezrin, Radixin, and Moesin Proteins Family: Implications for Cell Dynamics. *Biochim. Biophys. Acta BBA - Mol. Cell Biol. Lipids* **2014**, *1841* (5), 727–737.

(39) Jenkins, R. W.; Canals, D.; Hannun, Y. A. Roles and Regulation of Secretory and Lysosomal Acid Sphingomyelinase. *Cell. Signal.* **2009**, *21* (6), 836–846.

(40) Bartke, N.; Hannun, Y. A. Bioactive Sphingolipids: Metabolism and Function. *J. Lipid Res.* **2009**, *50* (Supplement), S91–S96.

(41) Chalfant, C. E.; Kishikawa, K.; Mumby, M. C.; Kamibayashi, C.; Bielawska, A.; Hannun, Y. A. Long Chain Ceramides Activate Protein Phosphatase-1 and Protein Phosphatase-2A ACTIVATION IS STEREOSPECIFIC AND REGULATED BY PHOSPHATIDIC ACID. *J. Biol. Chem.* **1999**, *274* (29), 20313–20317.

(42) Fan, J.; Sammalkorpi, M.; Haataja, M. Influence of Nonequilibrium Lipid Transport, Membrane Compartmentalization, and Membrane Proteins on the Lateral Organization of the Plasma Membrane. *Phys. Rev. E* **2010**, *81* (1), 011908.

(43) Gheber, L. A.; Edidin, M. A Model for Membrane Patchiness: Lateral Diffusion in the Presence of Barriers and Vesicle Traffic. *Biophys. J.* **1999**, *77* (6), 3163–3175.

(44) Klemm, R. W.; Ejsing, C. S.; Surma, M. A.; Kaiser, H.-J.; Gerl, M. J.; Sampaio, J. L.; Robillard, Q. de; Ferguson, C.; Proszynski, T. J.; Shevchenko, A.; et al. Segregation of Sphingolipids and Sterols during Formation of Secretory Vesicles at the Trans-Golgi Network. *J. Cell Biol.* **2009**, *185* (4), 601–612.

(45) Revenu, C.; Athman, R.; Robine, S.; Louvard, D. The Co-Workers of Actin Filaments: From Cell Structures to Signals. *Nat. Rev. Mol. Cell Biol.* **2004**, *5* (8), 635–646.

(46) Saarikangas, J.; Zhao, H.; Lappalainen, P. Regulation of the Actin Cytoskeleton-Plasma Membrane Interplay by Phosphoinositides. *Physiol. Rev.* **2010**, *90* (1), 259–289.

(47) Fujiwara, T.; Ritchie, K.; Murakoshi, H.; Jacobson, K.; Kusumi, A. Phospholipids Undergo Hop Diffusion in Compartmentalized Cell Membrane. *J. Cell Biol.* **2002**, *157* (6), 1071–1082.

(48) Nakada, C.; Ritchie, K.; Oba, Y.; Nakamura, M.; Hotta, Y.; Iino, R.; Kasai, R. S.; Yamaguchi, K.; Fujiwara, T.; Kusumi, A. Accumulation of Anchored Proteins Forms Membrane Diffusion Barriers during Neuronal Polarization. *Nat. Cell Biol.* **2003**, *5* (7), 626–632.

(49) Ritchie, K.; Iino, R.; Fujiwara, T.; Murase, K.; Kusumi, A. The Fence and Picket Structure of the Plasma Membrane of Live Cells as Revealed by Single Molecule Techniques (Review). *Mol. Membr. Biol.* **2003**, *20* (1), 13–18.

(50) Owen, D. M.; Neil, M. A. A.; French, P. M. W.; Magee, A. I. Optical Techniques for Imaging Membrane Lipid Microdomains in Living Cells. *Semin. Cell Dev. Biol.* **2007**, *18* (5), 591–598.

(51) Wüstner, D.; Brewer, J. R.; Bagatolli, L.; Sage, D. Potential of Ultraviolet Wide-Field Imaging and Multiphoton Microscopy for Analysis of Dehydroergosterol in Cellular Membranes. *Microsc. Res. Tech.* **2011**, *74* (1), 92–108.

(52) Fujita, A.; Cheng, J.; Fujimoto, T. Segregation of GM1 and GM3 Clusters in the Cell Membrane Depends on the Intact Actin Cytoskeleton. *Biochim. Biophys. Acta-Mol. Cell Biol. Lipids* **2009**, *1791* (5), 388–396.

(53) Sahl, S. J.; Leutenegger, M.; Hilbert, M.; Hell, S. W.; Eggeling, C. Fast Molecular Tracking Maps Nanoscale Dynamics of Plasma Membrane Lipids. *Proc. Natl. Acad. Sci.* **2010**, *107* (15), 6829–6834.

(54) Janich, P.; Corbeil, D. GM1 and GM3 Gangliosides Highlight Distinct Lipid Microdomains within the Apical Domain of Epithelial Cells. *FEBS Lett.* **2007**, *581* (9), 1783–1787.

(55) Touboul, D.; Brunelle, A.; Laprévote, O. Mass Spectrometry Imaging: Towards a Lipid Microscope? *Biochimie* **2011**, *93* (1), 113–119.

(56) Van Remoortere, A.; van Zeijl, R. J. M.; van den Oever, N.; Franck, J.; Longuespée, R.; Wisztorski, M.; Salzet, M.; Deelder, A. M.; Fournier, I.; McDonnell, L. A. MALDI Imaging and Profiling MS of Higher Mass Proteins from Tissue. *J. Am. Soc. Mass Spectrom.* **2010**, *21* (11), 1922–1929.

(57) Murphy, R. C.; Hankin, J. A.; Barkley, R. M.; Zemski Berry, K. A. MALDI Imaging of Lipids after Matrix Sublimation/deposition. *Biochim. Biophys. Acta BBA - Mol. Cell Biol. Lipids* **2011**, *1811* (11), 970–975.

(58) Touboul, D.; Roy, S.; Germain, D. P.; Chaminade, P.; Brunelle, A.; Laprévote, O. MALDI-TOF and Cluster-TOF-SIMS Imaging of Fabry Disease Biomarkers. *Int. J. Mass Spectrom.* **2007**, *260* (2–3), 158–165.

(59) Reyzer, M. L.; Caprioli, R. M. MALDI-MS-Based Imaging of Small Molecules and Proteins in Tissues. *Curr. Opin. Chem. Biol.* **2007**, *11* (1), 29–35.

(60) Chaurand, P.; Cornett, D. S.; Angel, P. M.; Caprioli, R. M. From Whole-Body Sections Down to Cellular Level, Multiscale Imaging of Phospholipids by MALDI Mass Spectrometry. *Mol. Cell. Proteomics* **2011**, *10* (2), O110.004259.

(61) Li, H.; Hummon, A. B. Imaging Mass Spectrometry of Three-Dimensional Cell Culture Systems. *Anal. Chem.* **2011**, *83* (22), 8794–8801.

(62) Touboul, D.; Laprévote, O.; Brunelle, A. Micrometric Molecular Histology of Lipids by Mass Spectrometry Imaging. *Curr. Opin. Chem. Biol.* **2011**, *15* (5), 725–732.

(63) Balluff, B.; Schöne, C.; Höfler, H.; Walch, A. MALDI Imaging Mass Spectrometry for Direct Tissue Analysis: Technological Advancements and Recent Applications. *Histochem. Cell Biol.* **2011**, *136* (3), 227–244.

(64) Goto-Inoue, N.; Hayasaka, T.; Zaima, N.; Setou, M. Imaging Mass Spectrometry for Lipidomics. *Biochim. Biophys. Acta BBA - Mol. Cell Biol. Lipids* **2011**, *1811* (11), 961–969.

(65) Sigmund, P. Theory of Sputtering. I. Sputtering Yield of Amorphous and Polycrystalline Targets. *Phys. Rev.* **1969**, *184* (2), 383–416.

(66) Yu, M. L. Matrix Effects in the Work-Function Dependence of Negative-Secondary-Ion Emission. *Phys. Rev. B* **1982**, *26* (8), 4731–4734.

(67) Yu, M. L. Chemical Enhancement Effects in SIMS Analysis. *Nucl. Instrum. Methods Phys. Res. Sect. B Beam Interact. Mater. At.* **1986**, *15* (1–6), 151–158.

(68) Piwowar, A. M.; Lockyer, N. P.; Vickerman, J. C. Salt Effects on Ion Formation in Desorption Mass Spectrometry: An Investigation into the Role of Alkali Chlorides on Peak Suppression in Time-of-Flight-Secondary Ion Mass Spectrometry. *Anal. Chem.* **2009**, *81* (3), 1040–1048.

(69) Jones, E. A.; Lockyer, N. P.; Kordys, J.; Vickerman, J. C. Suppression and Enhancement of Secondary Ion Formation Due to the Chemical Environment in Static-Secondary Ion Mass Spectrometry. *J. Am. Soc. Mass Spectrom.* **2007**, *18* (8), 1559–1567.

(70) Altelaar, A. F. M.; van Minnen, J.; Heeren, R. M. A.; Piersma, S. R. The Influence of the Cholesterol Microenvironment in Tissue Sections on Molecular Ionization Efficiencies and Distributions in ToF-SIMS. *Appl. Surf. Sci.* **2006**, *252* (19), 6702–6705.

(71) Sostarecz, A. G.; Cannon, D. M.; McQuaw, C. M.; Sun, S.; Ewing, A. G.; Winograd, N. Influence of Molecular Environment on the Analysis of Phospholipids by Time-of-Flight Secondary Ion Mass Spectrometry. *Langmuir* **2004**, *20* (12), 4926–4932.

(72) Rangarajan, S.; Tyler, B. J. Topography in Secondary Ion Mass Spectroscopy Images. *J. Vac. Sci. Technol. A* **2006**, *24* (5), 1730–1736.

(73) Tyler, B. Interpretation of TOF-SIMS Images: Multivariate and Univariate Approaches to Image de-Noising, Image Segmentation and Compound Identification. *Appl. Surf. Sci.* **2003**, *203–204*, 825–831.

(74) Prinz, C.; Höök, F.; Malm, J.; Sjövall, P. Structural Effects in the Analysis of Supported Lipid Bilayers by Time-of-Flight Secondary Ion Mass Spectrometry. *Langmuir* **2007**, *23* (15), 8035–8041.

(75) Kurczy, M. E.; Piehowski, P. D.; Van Bell, C. T.; Heien, M. L.; Winograd, N.; Ewing, A. G. Mass Spectrometry Imaging of Mating Tetrahymena Show That Changes in Cell Morphology Regulate Lipid Domain Formation. *Proc. Natl. Acad. Sci. U. S. A.* **2010**, *107* (7), 2751–2756.

(76) Ostrowski, S. G.; Van Bell, C. T.; Winograd, N.; Ewing, A. G. Mass Spectrometric Imaging of Highly Curved Membranes during Tetrahymena Mating. *Science* **2004**, *305* (5680), 71–73.

(77) Piehowski, P. D.; Davey, A. M.; Kurczy, M. E.; Sheets, E. D.; Winograd, N.; Ewing, A. G.; Heien, M. L. Time-of-Flight Secondary Ion Mass Spectrometry Imaging of Subcellular Lipid Heterogeneity: Poisson Counting and Spatial Resolution. *Anal. Chem.* **2009**, *81* (14), 5593–5602.

(78) Benninghoven, A. Surface Investigation of Solids by the Statical Method of Secondary Ion Mass Spectroscopy (SIMS). *Surf. Sci.* **1973**, *35*, 427–457.

(79) Passarelli, M. K.; Winograd, N. Lipid Imaging with Time-of-Flight Secondary Ion Mass Spectrometry (ToF-SIMS). *Biochim. Biophys. Acta BBA - Mol. Cell Biol. Lipids* **2011**, *1811* (11), 976–990.

(80) Cannon, D. M.; Pacholski, M. L.; Winograd, N.; Ewing, A. G. Molecule Specific Imaging of Freeze-Fractured, Frozen-Hydrated Model Membrane Systems Using Mass Spectrometry. *J. Am. Chem. Soc.* **2000**, *122* (4), 603–610.

(81) Zheng, L.; McQuaw, C. M.; Ewing, A. G.; Winograd, N. Sphingomyelin/Phosphatidylcholine and Cholesterol Interactions Studied by Imaging Mass Spectrometry. *J. Am. Chem. Soc.* **2007**, *129* (51), 15730–15731.

(82) McQuaw, C. M.; Zheng, L.; Ewing, A. G.; Winograd, N. Localization of Sphingomyelin in Cholesterol Domains by Imaging Mass Spectrometry. *Langmuir* **2007**, *23* (10), 5645–5650.

(83) Biesinger, M. C.; Paepegaey, P.-Y.; McIntyre, N. S.; Harbottle, R. R.; Petersen, N. O. Principal Component Analysis of TOF-SIMS Images of Organic Monolayers. *Anal. Chem.* **2002**, *74* (22), 5711–5716.

(84) Biesinger, M. C.; Miller, D. J.; Harbottle, R. R.; Possmayer, F.; McIntyre, N. S.; Petersen, N. O. Imaging Lipid Distributions in Model Monolayers by ToF-SIMS with Selectively Deuterated Components and Principal Components Analysis. *Appl. Surf. Sci.* **2006**, *252* (19), 6957–6965.

(85) Vaezian, B.; Anderton, C. R.; Kraft, M. L. Discriminating and Imaging Different Phosphatidylcholine Species within Phase-Separated Model Membranes by Principal Component Analysis of TOF-Secondary Ion Mass Spectrometry Images. *Anal. Chem.* **2010**, *82* (24), 10006–10014.

(86) Anderton, C. R.; Vaezian, B.; Lou, K.; Frisz, J. F.; Kraft, M. L. Identification of a Lipid-Related Peak Set to Enhance the Interpretation of TOF-SIMS Data from Model and Cellular Membranes. *Surf. Interface Anal.* **2012**, *44* (3), 322–333.

(87) Berman, E. S. F.; Kulp, K. S.; Knize, M. G.; Wu, L.; Nelson, E. J.; Nelson, D. O.; Wu, K. J. Distinguishing Monosaccharide Stereo- and Structural Isomers with TOF-SIMS and Multivariate Statistical Analysis. *Anal. Chem.* **2006**, *78* (18), 6497–6503.

(88) Wagner, M. S.; Shen, M.; Horbett, T. A.; Castner, D. G. Quantitative Analysis of Binary Adsorbed Protein Films by Time of Flight Secondary Ion Mass Spectrometry. *J. Biomed. Mater. Res. A* **2003**, *64A* (1), 1–11.

(89) Wagner, M. S.; Tyler, B. J.; Castner, D. G. Interpretation of Static Time-of-Flight Secondary Ion Mass Spectra of Adsorbed Protein Films by Multivariate Pattern Recognition. *Anal. Chem.* **2002**, *74* (8), 1824–1835.

(90) Wagner, M. S.; Shen, M.; Horbett, T. A.; Castner, D. G. Quantitative Time-of-Flight Secondary Ion Mass Spectrometry for the Characterization of Multicomponent Adsorbed Protein Films. *Appl. Surf. Sci.* **2003**, *203–204*, 704–709.

(91) Graham, D. J.; Ratner, B. D. Multivariate Analysis of TOF-SIMS Spectra from Dodecanethiol SAM Assembly on Gold: Spectral Interpretation and TOF-SIMS Fragmentation Processes. *Langmuir* **2002**, *18* (15), 5861–5868.

(92) Belu, A. M.; Graham, D. J.; Castner, D. G. Time-of-Flight Secondary Ion Mass Spectrometry: Techniques and Applications for the Characterization of Biomaterial Surfaces. *Biomaterials* **2003**, *24* (21), 3635–3653.

(93) Graham, D. J.; Wagner, M. S.; Castner, D. G. Information from Complexity: Challenges of TOF-SIMS Data Interpretation. *Appl. Surf. Sci.* **2006**, *252* (19), 6860–6868.

(94) Mellinger, M. Multivariate Data Analysis: Its Methods. *Chemom. Intell. Lab. Syst.* **1987**, *2* (1–3), 29–36.

(95) Malinowski, E. R. *Factor Analysis in Chemistry*, 3rd ed.; John Wiley and Sons, Inc.: New York, 2002.

(96) Pachuta, S. J. Enhancing and Automating TOF-SIMS Data Interpretation Using Principal Component Analysis. *Appl. Surf. Sci.* **2004**, *231–232*, 217–223.

(97) Tyler, B. J.; Rayal, G.; Castner, D. G. Multivariate Analysis Strategies for Processing ToF-SIMS Images of Biomaterials. *Biomaterials* **2007**, *28* (15), 2412–2423.

(98) Baker, M. J.; Zheng, L.; Winograd, N.; Lockyer, N. P.; Vickerman, J. C. Mass Spectral Imaging of Glycophospholipids, Cholesterol, and Glycophorin A in Model Cell Membranes. *Langmuir* **2008**, *24* (20), 11803–11810.

(99) Sjövall, P.; Lausmaa, J.; Johansson, B. Mass Spectrometric Imaging of Lipids in Brain Tissue. *Anal. Chem.* **2004**, *76* (15), 4271–4278.

(100) Brulet, M.; Seyer, A.; Edelman, A.; Brunelle, A.; Fritsch, J.; Ollero, M.; Laprévote, O. Lipid Mapping of Colonic Mucosa by Cluster TOF-SIMS Imaging and Multivariate Analysis in Cftr Knockout Mice. *J. Lipid Res.* **2010**, *51* (10), 3034–3045.

(101) Park, J.-W.; Min, H.; Kim, Y.-P.; Kyong Shon, H.; Kim, J.; Moon, D. W.; Lee, T. G. Multivariate Analysis of ToF-SIMS Data for Biological Applications. *Surf. Interface Anal.* **2009**, *41* (8), 694–703.

(102) Wilson, R. L.; Kraft, M. L. Quantifying the Molar Percentages of Cholesterol in Supported Lipid Membranes by Time-of-Flight Secondary Ion Mass Spectrometry and Multivariate Analysis. *Anal. Chem.* **2013**, *85* (1), 91–97.

(103) Wu, K. J.; Odom, R. W. Matrix-Enhanced Secondary Ion Mass Spectrometry: A Method for Molecular Analysis of Solid Surfaces. *Anal. Chem.* **1996**, *68* (5), 873–882.

(104) McDonnell, L. A.; Piersma, S. R.; Altelaar, A. F. M.; Mize, T. H.; Luxembourg, S. L.; Verhaert, P. D. E. M.; van Minnen, J.; Heeren, R. M. A. Subcellular Imaging Mass Spectrometry of Brain Tissue. *J. Mass Spectrom.* **2005**, *40* (2), 160–168.

(105) Fitzgerald, J. J. D.; Kunnath, P.; Walker, A. V. Matrix-Enhanced Secondary Ion Mass Spectrometry (ME SIMS) Using Room Temperature Ionic Liquid Matrices. *Anal. Chem.* **2010**, *82* (11), 4413–4419.

(106) Luxembourg, S. L.; McDonnell, L. A.; Duursma, M. C.; Guo, X.; Heeren, R. M. A. Effect of Local Matrix Crystal Variations in Matrix-Assisted Ionization Techniques for Mass Spectrometry. *Anal. Chem.* **2003**, *75* (10), 2333–2341.

(107) Altelaar, A. F. M.; Klinkert, I.; Jalink, K.; de Lange, R. P. J.; Adan, R. A. H.; Heeren, R. M. A.; Piersma, S. R. Gold-Enhanced Biomolecular Surface Imaging of Cells and Tissue by SIMS and MALDI Mass Spectrometry. *Anal. Chem.* **2006**, *78* (3), 734–742.

(108) Delcorte, A.; Bour, J.; Aubriet, F.; Muller, J.-F.; Bertrand, P. Sample Metallization for Performance Improvement in Desorption/Ionization of Kilodalton Molecules: Quantitative Evaluation, Imaging Secondary Ion MS, and Laser Ablation. *Anal. Chem.* **2003**, *75* (24), 6875–6885.

(109) Delcorte, A.; Yunus, S.; Wehbe, N.; Nieuwjaer, N.; Poleunis, C.; Felten, A.; Houssiau, L.; Pireaux, J.-J.; Bertrand, P. Metal-Assisted Secondary Ion Mass Spectrometry Using Atomic (Ga+, In+) and Fullerene Projectiles. *Anal. Chem.* **2007**, *79* (10), 3673–3689.

(110) Williams, P. Biological Imaging Using Secondary Ions. *J. Biol.* **2006**, *5* (6), 18.

(111) Wilson, R. L.; Frisz, J. F.; Hanafin, W. P.; Carpenter, K. J.; Hutcheon, I. D.; Weber, P. K.; Kraft, M. L. Fluorinated Colloidal Gold Immunolabels for Imaging Select Proteins in Parallel with Lipids Using High-Resolution Secondary Ion Mass Spectrometry. *Bioconjug. Chem.* **2012**, *23* (3), 450–460.

(112) Wilson, R. L.; Frisz, J. F.; Klitzing, H. A.; Zimmerberg, J.; Weber, P. K.; Kraft, M. L. Hemagglutinin Clusters in the Plasma Membrane Are Not Enriched with Cholesterol and Sphingolipids. *Biophys. J.* **2015**, *108* (7), 1652–1659.

(113) Edidin, M. Lipids on the Frontier: A Century of Cell-Membrane Bilayers. *Nat. Rev. Mol. Cell Biol.* **2003**, *4* (5), 414–418.

Figures and Tables

	TOF-SIMS	NanoSIMS
Lateral resolution	≥ 500 nm	≥ 100 nm
Information	Molecular	Elemental & isotopic
Typical strategy for lipid identification	*m/z* of ions is characteristic to the component of interest	Isotope labeling is used to encode the lipid species of interest with a distinctive isotope signature
Primary ion source	Cluster ion sources (C_{60+}, Bi_{3+}, Au_{3+}, SF_{5+})	Cs or oxygen
Mass analyzer	TOF	Magnetic sector
Secondary ion size	Molecular & high mass fragments	Monotomic & diatomic
Number of collected ions	Entire spectra	5–7 different m/z ratios
Requires a priori selection of target component(s)?	No	Yes
Unique capabilities	Identification of unknown lipid structures at specific locations in tissues; imaging unlabeled lipids with moderate (≥ 1 μm) lateral resolution	Imaging known lipids of interest within model or cellular membranes with high (~ 100 nm) lateral resolution
Major challenge	Low yields of intact molecular ions<comma> interpretation of the mass spectra	Selective incorporation of distinct isotopes or elements into specific lipid species

Table 1.1 Comparison of SIMS approaches.

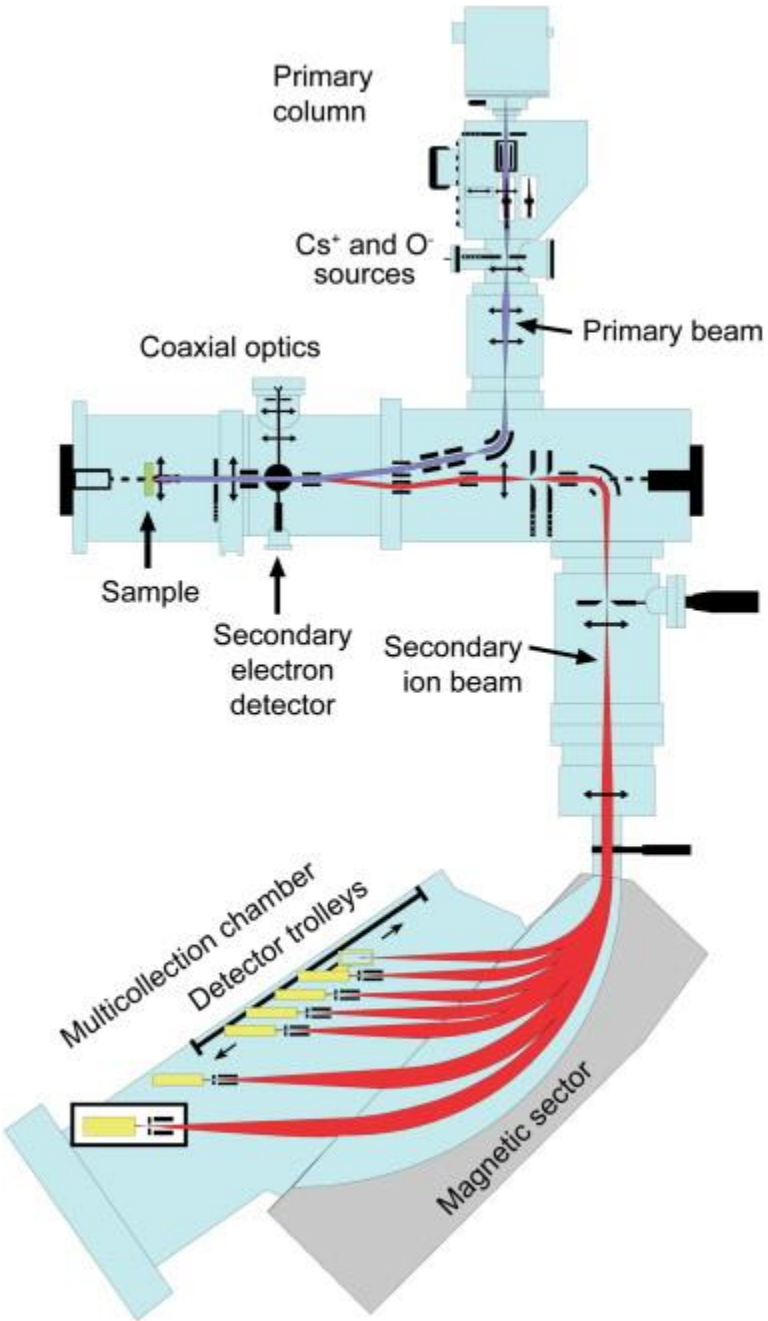

Figure 1.1 Schematic of the Cameca NanoSIMS 50. An oxygen or cesium primary ion beam is focused onto the sample. Positive or negative secondary ions, respectively, are collected by coaxial optics. Monoatomic and diatomic secondary ions with up to five different *m*/*z* ratios can be collected in parallel by the magnetic sector.
Reproduced with permission from Annu. Rev. Biophys. 38 (2009) 53–74.

CHAPTER 2.
DEVELOPMENT OF HIGH-RESOLUTION SECONDARY ION MASS SPECTROMETRY TECHNIQUES FOR THE VISUALIZATION OF SPHINGOLIPIDS ON PLASMA MEMBRANES

Notes and Acknowledgements[2]

This chapter features portions of work co-authored by Haley A. Klitzing, Peter K. Weber, and Mary L. Kraft that originally appeared in a published manuscript and has been reprinted with permissions from: Nanoimaging: Methods and Protocols (© Springer Science+Business Media, LLC 2013).[1]

We thank A. Ulanov for his valuable comments on the evaluation of isotope incorporation, C. Ramon for technical assistance, and L. Nittler for software development. MLK holds a Career Award at the Scientific Interface from the Burroughs Wellcome Fund. Portions of this work were carried out in the Metabolomics Center in the Roy J. Carver Biotechnology Center, Univ. of Illinois, and in the Frederick Seitz Materials Research Laboratory Central Facilities, Univ. of Illinois, which are partially supported by the U.S. Department of Energy (DOE) under grants DE-FG02-07ER46453 and DE-FG02-07ER46471. Work at Lawrence Livermore National Laboratory was supported by Laboratory Directed Research and Development funding and performed under the auspices of the U.S. DOE under contract DE-

[2] This chapter features portions of work which originally appeared in:
Klitzing, H. A.; Weber, P. K.; Kraft, M. L. Secondary Ion Mass Spectrometry Imaging of Biological Membranes at High Spatial Resolution. In *Nanoimaging*; Sousa, A. A., Kruhlak, M. J., Eds.; Humana Press: Totowa, NJ, 2013; pp 483–501.
This work has been reprinted with permissions from: Nanoimaging: Methods and Protocols (© Springer Science+Business Media, LLC 2013). Individual contributions to this work are: HAK cultured, preserved, and characterized cell samples, assisted with NanoSIMS analysis, and performed data analysis. PKW planned experiments and assisted with NanoSIMS analysis and data interpretation. MLK planned experiments, assisted with NanoSIMS analysis, and assisted with data analysis and interpretation. All authors contributed to writing the manuscript, with PKW focusing on aspects of the instrumentation and MLK and HAK focusing on preparation of samples.

AC52-07NA27344. This material was supported in part by the National Science Foundation under CHE—1058809.

Introduction

The distributions of cholesterol and specific lipid species within the plasma membrane are hypothesized to be linked to cellular function. However, characterizing the lateral variations in lipid abundance within biological membranes is especially challenging because few techniques provide the location-specific compositional information that is required for conclusive identification. Imaging secondary ion mass spectrometry (SIMS) offers a direct approach to imaging the lipid distribution within biological membranes in a chemically specific manner. In this method, a primary ion beam is used to produce neutral and ionized molecules and molecular fragments from the sample surface. The ionized species, which are called secondary ions, are analyzed in a mass spectrometer, providing chemical information about the molecules located within the primary beam. By scanning a focused primary ion beam across the sample and collecting the secondary ions, the intensities of the component-specific secondary ions detected at each position can be used to construct a map of the sample's surface composition. Several different approaches have been used to image lipid membranes with SIMS.[2–10] This chapter will focus on the use of high-resolution SIMS performed with a Cameca NanoSIMS 50 or 50 L. The NanoSIMS provides the optimum combination of spatial resolution, mass resolution (mass specificity), and ion transmission (sensitivity) for these experiments. Its short-comings are that a limited number of species can be detected simultaneously, and isotopic labels are necessary to distinguish most cellular molecules.

Proper preparation of biological membranes is critical for NanoSIMS analysis. Distinct stable isotopes or nonnative elements must be substituted into each molecule of interest so that the monatomic and small molecular secondary ions generated during NanoSIMS analysis can be linked to a specific parent molecule. In addition, biological samples must also be preserved so

that the membrane retains its organization when subjected to the ultrahigh vacuum conditions within the NanoSIMS analysis chamber. Although NanoSIMS is not performed on living cells, it has advantages that are complementary to many techniques that can be performed on living cells, including fluorescence microscopy including: chemically specific information is used to *directly* visualize the lipid organization; isotope-labeled lipids have the same chemical structure as the analogous native lipid molecule, so the isotope labels do not alter the lipid distribution; analysis can be restricted to the outermost 1 to 2 monolayers (≤5 nm) at the sample surface;[11] and a lateral resolution of 30 nm can be achieved with optimization meaning approximately 100 nm lateral resolution is routinely acquired on biological membranes.[5,8]

This chapter describes the basic principles of assessing the distribution of a specific lipid species in the plasma membranes of intact cells with NanoSIMS. As an example, the sample preparation, NanoSIMS imaging, and image analysis required to image the distribution of sphingolipids and all cellular lipids (i.e., sphingolipids and glycerolipids) within the plasma membrane of intact mouse fibroblast cells is described. These protocols and methodologies can be extended to imaging other lipid species or cholesterol within the plasma membrane of various types of cells. The new understanding of cholesterol and sphingolipid distribution within the plasma membrane that we have obtained with this approach is described in subsequent chapters.

Materials and Methods

Preparation of Cell Substrates

The 5 mm × 5 mm silicon chips (Ted Pella) were lightly scratched to produce an asymmetric pattern. The silicon chips were then washed with soap and thoroughly rinsed with water to ensure the removal of any traces of soap. The chips were then sterilized by autoclaving. After sterilization, the surface of the chips were covered with a sterile poly-L-lysine, generated

by passing it through a 0.22 μm syringe driven filter unit and depositing the effluent directly onto the sterile chips (Electron Microscopy Sciences).

Preparation of ^{15}N-Sphingoid Bases

The ^{15}N-sphingoid bases, ^{15}N-sphingosine and ^{15}N-sphinganine, were synthesized from ^{15}N-serine following reported methods.[12–16] The ^{15}N-sphingoid bases were dissolved in DMSO to make a 6 mM stock solution, which was sterilized by filtering through a DMSO-rinsed, syringe driven, sterile 0.2 μm PTFE filter unit. Sterile aliquots of ^{15}N-sphingoid bases were stored at −20°C, and warmed to room temperature before use.

Preparation of ^{13}C-Fatty Acids

A 1 mL stock solution of the fatty acid mixture was made by weighing out 13.3 mg of uniformly carbon-13 labeled algal lipid mixture (UL-^{13}C-algal lipids, 98%+) (Cambridge Isotope Laboratories, Inc.) into a microfuge tube. The outside of a hayman style microspatula scoop was used to obtain small portions of the lipid mixture that were deposited into the microfuge tube by wiping. We then added 3.3 mg of $^{13}C_{18}$-stearic acid (99 atom% ^{13}C) (Isotec) to a separate microfuge tube. Next, 125 mg of fatty acid free bovine serum albumin (BSA) (Sigma) and 1 mL of Dulbecco's phosphate-buffered saline (PBS) were added to a third microfuge tube, and dissolved by vortexing. Remaining large crystals were dissolved by briefly centrifuging for a few seconds. Once fully dissolved, the BSA was sterile filtered through a syringe driven, 0.22 μm PVDF filter unit that had been rinsed with PBS, and collected in a sterile microfuge tube. The filter unit was air-purged to ensure a quantitative transfer. To the microfuge tube containing the algal lipid mixture, 250 μL of DMSO was added and vortexed to dissolve. The dissolved UL-^{13}C-algal lipid mixture was quantitatively transferred into the microtube containing the $^{13}C_{18}$-stearic acid, and vortexed. The solution was then sonicated in a bath sonicator until all of the

crystals were dissolved. The UL-^{13}C-algal lipid/$^{13}C_{18}$-stearic acid mixture was sterile filtered using a pre-DMSO-rinsed, syringe driven, 0.2 μm PTFE filter unit that had been air-purged to ensure quantitative transfer. To this sterile 250 μL solution, 750 μL of the sterile BSA solution was added. The BSA/ UL-^{13}C-algal lipid/ $^{13}C_{18}$-fatty acid mixture was vortexed and sonicated for 15 min to dissolve all the precipitate. This resulted in a 1 mL stock solution that had a concentration of 16.6 mg/mL, or approximately 0.0556 M. This solution was stored at 4°C. Prior to use, the stock solution was warmed to room temperature and thoroughly mixed by vortexing.

Cell Culture

NIH3T3 (ATCC CRL-1658^{TM}) and a NIH3T3 transfected mouse fibroblast cell line that stably expresses influenza hemagglutinin (Clone 15 cell line) were grown in high glucose Dulbecco's modified Eagle's medium (DMEM) supplemented with 10% Hyclone calf serum, 10^4 U/mL penicillin G, and 10 mg/mL streptomycin (Media A) for 1 passage (3 days) at 37°C in 5% CO_2. Each day, the stock solution of ^{15}N-sphingoid bases was added via pipette to maintain a ^{15}N-sphingoid base concentration of 3 μM. It was assumed that all of the ^{15}N-sphingoid bases added to the medium were consumed within 24h. After 3 d, the cells had reached approximately 80% confluence and were passaged into new culture dishes that contained high glucose DMEM supplemented with 10% Hyclone lipid-reduced fetal bovine serum and 1% Hyclone calf serum (Media B) at 37°C in 5% CO_2. The stock solutions of ^{15}N-sphingoid bases, ^{13}C-fatty acids, and ethanolamine were was added via pipette each day to maintain concentrations of 3 μM, 215 μM, and 2 μM, respectively, where all of these supplements were assumed to have been completely consumed after 24h. On the sixth day, the cells were passaged and reset with fresh Media B and supplements in dishes that also contain sterilized and poly-L-lysine-coated silicon chips. The cells were collected on the 7th day.

Collection of Samples

Silicon chips with attached cells were removed from the dishes and set aside for chemical fixation. All cells remaining on the dish were detached and collected in a centrifuge tube. Cells were pelleted by centrifuging for 5 min at 201 × g. All but approximately 0.5 mL of the supernatant was removed from the cell pellet to ensure that the cell pellet did not dry out. To wash the pellet, 10 mL of PBS was added to the cells, the cells were collected by centrifugation, and all but 0.5 mL of PBS was decanted from the pellet. After repeating this process twice, the cells were spun down, the excess PBS removed, and the cells were stored at −20°C until label incorporation was evaluated.

Lipid Extraction

The methods for lipid extraction were modified from the method of Bligh and Dyer.[17] To each cell pellet, 2 mL methanol and 1 mL chloroform were added. If there was no PBS remaining on the cell pellet, 0.8 mL of water was also added. The pellet was then vortexed and sonicated to break it apart and mix thoroughly before sitting at room temperature for 1 h. The pellet was then centrifuged at 1,811 × g for 5 min. The liquid supernatant was decanted into a new centrifuge tube, leaving behind the cell pellet. To the supernatant, 1 mL of chloroform and 1 mL of water were added, followed by vortexing and centrifugation at 1,811 × g for 5 min. The lower, chloroform layer was then transferred into a new vial and dried down under a stream of nitrogen gas. The crude lipid extracts were dissolved in 100 μL methanol and then centrifuged at 17, 562 × g for 5 min. An injection of 4 μL of this supernatant was used for high performance liquid chromatography (HPLC-MS) analysis of ^{15}N-incorporation.

Evaluation of Nitrogen-15 Incorporation into Cellular Sphingolipids

The nitrogen-15 incorporation into the cellular sphingomyelin was analyzed with an Agilent 1100 LC/MSD Trap XCT Plus equipped with a Phenomenex Gemini 3u C6-Phenyl 110A column (2 × 100 mm). The separation was performed using methanol at a flow rate of 300 μL/min. The following mass peaks were monitored (retention time was 1.5 min for the stated instrument): *m*/*z* 703.6 (unlabeled N-palmitoyl sphingomyelin), 704.6 (^{15}N-palmitoyl sphingomyelin), 719.6 (^{14}N-palmitoyl $^{13}C_{16}$-sphingomyelin), 720.6 (^{15}N-palmitoyl $^{13}C_{16}$-sphingomyelin), and 735.7 (^{14}N-palmitoyl $^{13}C_{32}$-sphingomyelin). For the cell lines used, no significant signal was detected for other sphingolipid species. The contribution of N-palmitoyl sphingomyelin isotopologues other than ^{15}N-palmitoyl sphingomyelin from peak *m*/*z* 704.6 was removed by subtracting 43.3% of the intensity of the N-palmitoyl sphingomyelin peak (*m*/*z* 703.6) from that of peak *m*/*z* 704.6. The contribution of sphingomyelin isotopologues other than ^{15}N-palmitoyl $^{13}C_{16}$ sphingomyelin to peak *m*/*z* 720.6 was removed by subtracting 25.8% of the intensity of the ^{14}N-palmitoyl $^{13}C_{16}$ sphingomyelin peak at *m*/*z* 719.6 from that of peak *m*/*z* 720.6. The fraction of N-palmitoyl sphingomyelin that contained a nitrogen-15 isotope was calculated as the ratio of the sum of ^{15}N-palmitoyl sphingomyelin and ^{15}N-palmitoyl $^{13}C_{16}$-sphingomyelin peak intensities to the sum of the peak intensities from all N-palmitoyl sphingomyelin isotopologues. The fraction of N-palmitoyl sphingomyelin that biosynthesized from uniformly labeled ^{13}C-palmitic acid was calculated as the ratio of the sum of ^{14}N-palmitoyl $^{13}C_{16}$-sphingomyelin, ^{15}N-palmitoyl $^{13}C_{16}$-sphingomyelin, and ^{14}N-palmitoyl $^{13}C_{32}$-sphingomyelin, over the sum of the peaks produced by all N-palmitoyl sphingomyelin isotopologues.

Evaluation of Carbon-13 Incorporation into All Cellular Lipids

To the crude lipid extracts after LC-MS analysis, 2.5 mL of 95% ethanol and 50 μL of 33% KOH (w/v) was added, and the sample incubated at 70°C for 90 min. The solution was cooled to room temperature, transfered to a centrifuge tube, and 3 drops of concentrated HCl was added. Next, 5 mL of hexane was added, and the sample was vortexed and centrifuged at 1,811 × g for 5 min. The upper, hexane layer was transferred to a new vial and dried down under a stream of nitrogen gas. The sample was resuspended in 100 μL of MeOH:CH_2Cl_2 (1:1), 20 μL of a 2 M solution of trimethylsilyldizomethane in hexane was added, and it was incubated for 1 h at room temperature. Gas chromatography-mass spectrometry (GC-MS) was performed on the resulting solution of fatty acid methyl esters (FAMEs) using an Agilent 6890 gas chromatograph with a ZB-WAX (30 m × 0.25 mm I.D., 0.25 μm film thickness) capillary column (Phenomenex, USA), an Agilent 5973 mass selective detector and HP 7683B (Agilent Inc, USA) autosampler. The inlet and MSD interface temperatures were set to 250°C, and the ion source temperature to 230°C, and a constant flow rate of 1.3 mL/min was used for the helium carrier gas. In positive electron impact mode (EI), the signal intensities corresponding to the FAMEs of $^{13}C_{16}$-palmitic acid (*m*/*z* 286), $^{12}C_{16}$-palmitic acid (*m*/*z* 270), $^{13}C_{16}$-palmitoleic acid (*m*/*z* 284), $^{12}C_{16}$- palmitoleic acid (*m*/*z* 268), $^{13}C_{18}$-stearic acid (*m*/*z* 316), $^{12}C_{18}$-stearic acid (*m*/*z* 298), $^{13}C_{18}$-oleic acid (*m*/*z* 314), $^{12}C_{18}$-oleic acid (*m*/*z* 296), $^{13}C_{18}$-linoleic acid (*m*/*z* 312), and $^{12}C_{18}$-linoleic acid (*m*/*z* 294) were collected. These intensities were then correlated to determine a representative incorporation value.

Cell Preservation with Chemical Fixation

Silicon chips with adherent cells were removed from cell culture and rinse three times with Hendry's Phosphate Buffer (HPB) for 3 min each. Care was taken as not to disturb the

attached cells. The chips were then flooded with 4% glutaraldehyde in HPB and allowed to fix for 30 min. The glutaraldehyde fixative was then removed, and the chips were rinsed twice with HPB for 5 min each, followed by rinsing once with water for 5 min. Chips were then further fixed and stained with freshly diluted, freshly filtered 1% osmium tetroxide for 15 min. After the removal of the osmium tetroxide, the chips were rinsed three times for 5 min each with water. Excess water was then removed, and the samples were to air dried followed by storage at room temperature.

NanoSIMS Imaging of Cells

Samples were coated with ~3 nm of iridium (99.95% Ir) to prevent charging during SIMS analysis. SIMS was performed on a NanoSIMS 50 (Cameca) at Lawrence Livermore National Laboratory with a 0.14 pA, 15 keV $^{133}Cs^{+}$ primary ion beam with a beam size of ~70-nm. Four replicate scans of 512 x 512 pixels were performed over a 15 µm x 15 µm analysis region using a dwell time of 1 ms/pixel resulting in an ion dose of 4.1×10^{14} ions/cm^2.

Data Analysis

The collected NanoSIMS data were processed using a custom software package (LIMAGE; L.R. Nittler, Carnegie Institution of Washington) that runs on the PV-Wave platform (Rogue Wave Software). Isotope enrichment images were constructed by taking the ratio of the heavy isotope ion and the light isotope ion ($^{13}C^{1}H^{-}/^{12}C^{1}H^{-}$ and $^{15}N^{12}C^{-}/^{14}N^{12}C^{-}$) followed by dividing the resulting ratio by the standard natural abundance ratios (0.011237 and 0.00367, respectively). To minimize noise in the images, a 3 by 3- pixel moving average smoothing algorithm was used during image construction. The MATLAB Statistics Toolbox was the used to determine any local elevations of statistical significance.

Results

Metabolic Labeling of Cells

To visualize specific molecules in the plasma membrane, a distinct stable isotope must be incorporated into the target molecules in the cell. This can be achieved with metabolic labeling. The general approach was to culture the cells in the presence of the isotope-labeled precursors, which are metabolized and integrated into the cells' infrastructure. Methods have been established to selectively incorporate distinct stable isotopes or radiolabels into specific lipid species, including phosphatidylethanolamine,[18] cholesterol,[19–21] sphingolipids,[22–24] and gangliosides.[25] These methods must be optimized so that a high fraction of the lipid species of interest within the cell contains the distinct isotope, as the isotope enrichment image will reveal the location and density of only the labeled lipids.

The selection of the distinct isotope label will influence NanoSIMS detection. Species with high ionization probability (i.e., CN^-, F^-, O^-, and S^-) can be detected the most efficiently. For the detection of species with lower ionization probabilities (i.e., CH^- and C^-), a high fraction of the abundant isotope should be replaced with the rare isotope (i.e., the use of $^{13}C_{16}$-palmitic acid is more desirable than $^{13}C_2$-palmitic acid). Here, we describe how to prepare isotope-labeled cells for analysis with a Camecan NanoSIMS. This includes the metabolic incorporation of ^{15}N into the majority of the cellular sphingolipids, and ^{13}C into the majority of cellular lipids.

To facilitate imaging the same cells with multiple imaging techniques an asymmetric pattern was lightly scratched onto the 5 mm × 5 mm silicon chips that are used to support the cells. . Prior to using the patterned chips, they must be washed with soap and water, rinsed well with water to remove any traces of soap, and sterilized by autoclaving. Then to promote cell adhesion, the surfaces of the sterilized chips were covered with a sterile poly-L-lysine solution.

We have found that a satisfactory poly-L-lysine layer was produced by incubating the sterile poly-L-lysine solution with the chips at 4 °C overnight. Satisfactory results may also be obtained with other temperatures and incubation times.

The ^{15}N-sphingoid bases, ^{15}N-sphingosine and ^{15}N-sphinganine, that were metabolically incorporated into the cells can be synthesized from ^{15}N-serine following reported methods.[12–16] Deuterated sphingosine (Avanti Polar Lipids) can be used in its place, and $^{12}C^{2}H^{-}$ and $^{12}C^{1}H^{-}$ secondary ions can be collected with the NanoSIMS for the detection of the deuterated sphingolipids. However, we have not evaluated the intensity of the secondary ions that are specific to the deuterated sphingolipids. We use a 6 mM stock solution of the ^{15}N-sphingoid bases dissolved in DMSO for metabolic labeling. This stock solution must be sterilized by filtering it through a pre-DMSO-rinsed, syringe driven, sterile 0.2 μm PTFE filter unit, and stored at −20°C. To reduce the time required to warm the solution to room temperature prior to use and limit the number of times that the stock solution was thawed and refrozen, the sterile stock solution should be stored as ~1 mL aliquots in sterile 1.7 mL microfuge tubes..

The stock ^{13}C-fatty acid solution that we use to incorporate carbon-13 into all cellular lipids consists of uniformly carbon-13 labeled algal lipids (13.3 mg/mL), $^{13}C_{18}$-stearic acid (3.3 mg/mL), and BSA (125 mg/mL) in PBS. Due to the low solubility of the fatty acids in aqueous mediums, ^{13}C-fatty acid and BSA solutions were prepared and sterilized separately, and then combined to create the stock solution that was used for metabolic labeling. To prepare the ^{13}C-fatty acid solution, the ^{13}C-fatty acids were dissolved in DMSO (250 μL per 16.6 mg fatty acid) and sterile filtered through a pre-DMSO-rinsed, syringe driven, 0.2 μm PTFE filter unit that was air-purged to ensure quantitative transfer. The BSA solution was prepared by dissolving the BSA in PBS (125 mg/mL) and sterile filtering it into a sterile microfuge tube using a syringe driven,

0.22 μm PVDF filter unit that had been rinsed with PBS. Finally, 250 μL of the sterile ^{13}C-fatty acid solution was combined with 750 μL of the sterile BSA solution, mixed with a vortexer, and sonicated for 15 min, or until any visible precipitate dissolves. The resulting 1 mL stock solution has a concentration of 16.6 mg/mL, or approximately 0.0556 M. This solution was used to achieve the desired concentration in the cell culture media and was stored at 4°C. This stock solution must be warmed to room temperature and thoroughly mixed by vortexing prior to subsequent use.

Cell lines used in these studies included NIH3T3 (ATCC CRL-1658^{TM}) and a NIH3T3 transfected mouse fibroblast cell line that stably expresses influenza hemagglutinin (Clone 15 cell line). Note that other cell lines can follow similar procedures for metabolic labeling, but adjustments in the labeling conditions (concentrations, labeling period, media, etc.) may be required to obtain high levels of isotope incorporation. First, to metabolically incorporate nitrogen-15 into the cellular sphingolipids, the cells were grown in media that contains 3 μM of ^{15}N-sphingoid bases for 1 passage (3 days). We assume that all of the ^{15}N-sphingoid bases were consumed within 24 h, so the stock ^{15}N-sphingoid base solution was added daily to maintain a 3 μM concentration in the culture. The cells should reach approximately 80% confluence on day 3, at which point they were ready to be passaged into new medium (Medium B) designed for the metabolic incorporation of nitrogen-15 into cellular sphingolipids and carbon-13 into all cellular lipids. This medium contained high glucose DMEM supplemented with serum (10% Hyclone lipid-reduced fetal bovine serum and 1% Hyclone calf serum) ^{15}N-sphingoid bases, ^{13}C-fatty acids, and ethanolamine (3 μM, 215 μM, and 2 μM respectively). Noteworthy, lipid-reduced fetal bovine serum was employed because calf serum contains fairly higher levels of unlabeled (natural abundance) lipids that compete with the ^{13}C-labeled fatty acids for incorporation into

cellular lipids. A small amount of calf serum was included because the cells grew poorly without it. Stock solutions of ^{15}N-sphingoid bases, ^{13}C-fatty acids, and ethanolamine were added every 24 h to maintain concentrations of 3 μM, 215 μM, and 2 μM, respectively, in the culture. On the sixth day, cells are passaged into new dishes containing fresh Media B and sterilized and poly-L-lysine-coated silicon chips. The silicon chips with attached cells are collected on the 7th day and chemically fix as described below. The cells remaining attached to the dish are collected and used to evaluate isotope incorporation.

Evaluation of Label Incorporation

In order for analysis with the NanoSIMS to be successful, a sufficient amount of isotope label must be incorporated into the plasma membrane to ensure the lipid-specific secondary ions can be detected by NanoSIMS with satisfactory signal to noise. In addition, because only the isotope-labeled lipids will be visible in the NanoSIMS image, a high fraction of the lipid species of interest within the cell should contain the isotope label so that the isotope enrichment image was representative of that lipid's distribution and density within the plasma membrane. The cells that remained attached to the dish after removing the silicon chips are used to assess the isotope incorporation into the lipid species of interest. Their lipids are extracted using a protocol that was adapted from the method of Bligh and Dyer,[17] as described in the Materials and Methods section. Extractions are typically performed on approximately 2×10^6 cells/pellet.

LC-MS was used to determine the fraction of the cellular sphingolipids that contain nitrogen-15. The following mass peaks are monitored: *m*/*z* 703.6 (unlabeled N-palmitoyl sphingomyelin), 704.6 (^{15}N-palmitoyl sphingomyelin), 719.6 (^{14}N-palmitoyl $^{13}C_{16}$-sphingomyelin), 720.6 (^{15}N-palmitoyl $^{13}C_{16}$-sphingomyelin), and 735.7 (^{14}N-palmitoyl $^{13}C_{32}$-sphingomyelin). For the cell lines used, no significant signal was detected for other sphingolipid

species. However, different cell lines may metabolize the lipid precursors into other sphingolipid classes, so the presence of ion peaks corresponding to other sphingolipid species should also be evaluated and included (if present) when determining the incorporation values. The contribution of N-palmitoyl sphingomyelin isotopologues other than ^{15}N-palmitoyl sphingomyelin from peak *m*/*z* 704.6 was removed by subtracting 43.3% of the intensity of the N-palmitoyl sphingomyelin peak (*m*/*z* 703.6) from that of peak *m*/*z* 704.6. The contribution of sphingomyelin isotopologues other than ^{15}N-palmitoyl $^{13}C_{16}$ sphingomyelin to peak *m*/*z* 720.6 was removed by subtracting 25.8% of the intensity of the ^{14}N-palmitoyl $^{13}C_{16}$ sphingomyelin peak at *m*/*z* 719.6 from that of peak *m*/*z* 720.6. The fraction of N-palmitoyl sphingomyelin that contained a nitrogen-15 isotope was calculated as the ratio of the sum of ^{15}N-palmitoyl sphingomyelin and ^{15}N-palmitoyl $^{13}C_{16}$-sphingomyelin peak intensities to the sum of the peak intensities from all N-palmitoyl sphingomyelin isotopologues. The fraction of N-palmitoyl sphingomyelin that biosynthesized from uniformly labeled ^{13}C-palmitic acid was calculated as the ratio of the sum of ^{14}N-palmitoyl $^{13}C_{16}$-sphingomyelin, ^{15}N-palmitoyl $^{13}C_{16}$-sphingomyelin, and ^{14}N-palmitoyl $^{13}C_{32}$-sphingomyelin, over the sum of the peaks produced by all N-palmitoyl sphingomyelin isotopologues.

The fraction of the fatty acids within the cellular lipids that are uniformly labeled with carbon-13 was measured with GC-MS. For this purpose, the lipid extracts from the cells are hydrolyzed with base to release the fatty acids from the lipid backbone. Then the fatty acids are neutralized with acid and converted to methylesters by treatment with trimethylsilyldizomethane. GC-MS was performed on the resulting solution of fatty acid methyl esters (FAMEs). In positive electron impact mode (EI), the signal intensities corresponding to the FAMEs of $^{13}C_{16}$-palmitic acid (*m*/*z* 286), $^{12}C_{16}$-palmitic acid (*m*/*z* 270), $^{13}C_{16}$-palmitoleic acid (*m*/*z* 284), $^{12}C_{16}$- palmitoleic

acid (*m*/*z* 268), $^{13}C_{18}$-stearic acid (*m*/*z* 316), $^{12}C_{18}$-stearic acid (*m*/*z* 298), $^{13}C_{18}$-oleic acid (*m*/*z* 314), $^{12}C_{18}$-oleic acid (*m*/*z* 296), $^{13}C_{18}$-linoleic acid (*m*/*z* 312), and $^{12}C_{18}$-linoleic acid (*m*/*z* 294) are collected. These intensities can then be correlated to determine a representative incorporation value.

Cell Preservation with Chemical Fixation

Imaging with the NanoSIMS was performed under ultrahigh vacuum conditions, so the cells must be dehydrated without perturbing the lateral distributions of lipids and proteins within the cell membrane. This was accomplished by chemically preserving the cells. The method described here was derived from protocols used to chemically fix cells in order to prepare them for analysis with scanning electron microscopy. This chemical fixation procedure produces a membrane whose morphology is retained during the inevitable drying process needed for introduction into the vacuum of the SIMS analysis chamber.[26] Different chemical preservation protocols can be used as long as they involve a heavy fixation that can withstand ultrahigh vacuum conditions. In our method, chips with adherent cells are removed from cell culture and rinsed three times with HPB for 3 min each. Care was taken so as not to disturb the attached cells. The chips are flooded with 4% glutaraldehyde and allowed to fix for 30 min. An easy way of fixing and rinsing without wasting large amounts of material is to place the chips in a parafilm-lined dish and to use pipettes for transferring the liquids. The parafilm will encourage the liquids to pool onto the chip, and the pipettes can be easily used for placing a drop of liquid onto the chips or suctioning off and disposing used material. The glutaraldehyde was removed, and the chips are rinsed twice with HPB for 5 min each, followed by rinsing once with water for 5 min. They are then fixed and stained with freshly diluted, freshly filtered 1% osmium tetroxide for 15 min. The osmium tetroxide was removed, and the chips are rinsed three times for 5 min

each with water. Excess water was removed; the samples are allowed to air dry, and are then stored at room temperature.

Pre-Characterization of Cells

To ensure efficient use of time on the NanoSIMS instrument, assessment of cell preservation was performed using bright field microscopy and low voltage SEM prior to NanoSIMS analysis. An optical map that shows the locations of cells in relation to one another, the scratches on the chip, and the edges of the chip was first created with bright field microscopy. Then, low voltage SEM was used to identify the cells that are best-suited for NanoSIMS analysis. This map will facilitate locating desirable cells during NanoSIMS analysis. Cells that are ideal for NanoSIMS analysis should be well-preserved (i.e., free of cracks or debris), relatively flat, and located away from the edges of the chip. The specific cells that are imaged with SEM should be indicated on the optical bright field map of the chip, which will be used to relocate them in the NanoSIMS. So, first, the entire surface of the chip was mapped with bright field imaging performed at 10-times or 20-times magnification. Starting at one corner of the chip, a series of overlapping images was acquired of the entire chip, and then these images were stitched together to create the optical map of the sample.

Samples can be metal coated to ~5 nm thickness. Sputter coating should be optimized for the individual sample and imaging conditions. A thicker coating should be employed if sample charging occurs. Gold, gold-palladium, iridium and other metals may be used, but carbon coating should not be used. SEM imaging was performed using low voltage to avoid sample charging and to prevent damage. SEM imaging at higher than 5 kV damages the sample. This damage is visible as cracks on the cells. Making small rasters on the sample, such as for higher magnification, can also cause damage in the form of the decomposition of molecules at the

surface of the cell. Images of individual cells are acquired at a low magnification (500–1,100×), and which cells are imaged with SEM was indicated on the optical map of the chip.

SIMS Imaging

The specifics of this section are based on a NanoSIMS 50. Other SIMS instruments can be used for this work, though with some loss in spatial resolution, sensitivity, specificity and/or analysis speed.

NanoSIMS Settings

The analysis conditions are set according to the species to be detected and the spatial resolution needed. Here, the parameters are set based on detecting $^{12}C^{1}H^{-}$, $^{13}C^{1}H^{-}$, $^{14}N^{12}C^{-}$, and $^{15}N^{12}C^{-}$ with 50–100 nm lateral spatial resolution. Carbon isotopes can also be detected using C^{-}, C_2^{-}, and $^{14}NC^{-}$. Other species can be detected on additional detectors. The target mass resolving power (MRP $\equiv$ M/ΔM) is 7,000 to resolve $^{13}C_2^{-}$ from $^{14}N^{12}C^{-}$ ($\Delta M = 0.0037$ amu) and $^{11}B^{16}O^{-}$ from $^{15}N^{12}C^{-}$ ($\Delta M = 0.0041$ amu). Because of the way the NanoSIMS software calculates MRP, ~11,000 MRP must be obtained based on the NanoSIMS high mass resolution scan to achieve the functional mass resolving power of 7,000. Lower mass resolving power can be used if the ^{13}C enrichment is low or natural abundance and BO^{-} counts are negligible. The cesium microbeam ion source was placed at 8,000 V and was mechanically aligned in the primary column based on maximizing the current at the primary Faraday cup (FCp). The filament current on the microbeam ion source reservoir was adjusted to achieve ~30 nA Cs^{+}. The sample was placed at −8,000 V. The L1 lens in the primary column was placed at approximately 6,500 V for high resolution (<100 nm), or left at zero for moderate resolution (~150 nm). One should select a 150 μm or smaller diameter aperture from the D1 aperture strip (primary beam limiting aperture) for the highest resolution (50 nm), 200 μm for high resolution (~75 μm), or 300 μm for moderate

resolution. The resulting beam current at the sample, as measured at the object Faraday cup (FCo), should be ~0.25 pA Cs^+ for the highest resolution or ~2 pA for moderate resolution. We then either adjust the reservoir current or perform more advanced alignment procedures to achieve the target beam current.

The secondary ion beam must be aligned in the column in the total ion count detector with the secondary ion beam centering deflectors. This alignment is typically only performed with changes in instrument hardware. Next the desired masses are aligned in the individual detectors in the multicollection chamber. Both vertical and horizontal coincidence must be confirmed. To enable 11,000 MRP in NanoSIMS units (a functional 7,000 MRP), the 10 μm × 100 μm entrance slit was aligned on the secondary ion beam by maximizing the current at the multicollector detectors; the 150 × 150 μm^2 aperture slit was then aligned on the secondary ion beam in the same way. The secondary ion beam was next tuned using standard Cameca procedures to achieve ~11,000 MRP. The primary beam focusing was performed in parallel with secondary ion beam focusing. The primary beam diameter on the sample, which determines image resolution, was checked at this point (as described below) to ensure the imaging target was achieved. The SIMS analysis location was aligned with the CCD optical imaging reticule using a reference sample. This alignment was necessary to allow centering on target cells without SIMS imaging.

Sample Loading and Analysis Locations

Sample chips should be loaded into a front-justified sample holder. The sample well in the holder can be 7.2 mm diameter, 5 × 5 mm squares, or a ~6 mm diameter aperture in a larger hole. The samples should be held in place from behind by non-magnetic springs. We then introduce the sample holder into the analysis vacuum chamber after pumping in the airlock.

Prospective analysis locations are located in the CCD image based on the light microscopy and SEM imaging, and the coordinates are saved in the point table. Also we save the location of nearby cells that can be used for tuning. All sample chips on the holder can be mapped before moving to SIMS analysis position to save time.

Cell Analysis

The primary challenge of the sample analysis was to position the sample and align the secondary beam so that the tuning accomplished above was achieved with the target cells. Control samples should be analyzed in the same session to ensure analysis quality. First, we would move to SIMS analysis position and choose a starting area, go to the preselected tuning cell, and adjust sample height and secondary ion beam steering. It was necessary to check MRP and peak alignment, ensuring that interfering isobars are not collected (Fig. 2.1 and Table 2.1). Significant changes in MRP or peak alignment potentially indicate excessive sample topography. Adjustments in tuning can be made to improve MRP, but caution is necessary to assure analysis quality. Note that abundances are calculated relative to isotopologues and cannot be directly compared to other molecules. For example, the yield of CN^- is typically ~10× that of C_2^-, although it is unlikely that CN^- was present at 10× higher levels than C_2^-. After tuning was complete, we would turn off the primary beam and move to the desired starting location on the target cell. Five to ten micrometers leeway was allowed for stage drift and misalignment of the CCD and SIMS imaging. The analysis conditions were set so that the primary beam cross section from pixel to pixel overlaps by at least 50%. The scan rate was set to enable multiple scans before eroding through the plasma membrane (e.g., 512 × 512 pixels, 15 × 15 μm^2, 0.5–1 ms/pixels, 3–5 scans; see below for calculation of sputter depth). Target species (e.g., $^{12}C^1H^-$, $^{13}C^1H^-$, $^{14}N^{12}C^-$ and $^{15}N^{12}C^-$) and secondary electrons are collected.

Data Analysis

Determination of Analysis Depth

Determination of the sputtering depth was straightforward, involving use of established formulas and procedures. To ensure that the vast majority of secondary ions are produced by the cell membrane and few secondary ions are collected from the underlying cytoplasm, the sputtering depth should be less than the sum of the thicknesses of the membrane (7.5 nm)[27] and the metal coating (~5 nm). If the sputtering depth exceeds the membrane thickness, it can be reduced by discarding some of the image planes. Because the sputtering depth increases with each subsequent image plane, the last image plane(s) to be acquired should be discarded until the sputtering depth is less than approximately 5 nm.

The sputtering depth (D_{sp}) was calculated using the sputter rate (R_{sp}), primary ion beam current at the sample (FCo) in pA, raster area (A_{ras}) in μm^2, and the sputtering time (t_{sp}) in seconds. The sputter rate determined on other biological samples, which ranges from 0.9 $nm \cdot \mu m^2/pA \cdot s$ (unpublished results) to 2.5 $nm \cdot \mu m^2/pA \cdot s$ [11] may be employed. The primary ion beam's current at the FCp and raster area were recorded during NanoSIMS analysis. The primary ion beam current at the sample (FCo) must be measured separately. The sputtering time (t_{sp}) is calculated using the dwell time (t_{dw}) for each pixel (pxl), the total pixels (pxl_{tot}) per image plane, and the total number of image planes (N_P) according to Eq. 2.1.

$$\text{Sputtering time} = \left(\frac{\text{dwell}}{\text{pixel}}\right)\left(\frac{\text{total pixels}}{\text{image plane}}\right)(\text{number of image planes}) \quad (2.1)$$

For example, for a 512 × 512 pixel image consisting of four image planes that were each acquired with a dwell of 1 ms/pixel, the total sputtering time is 1048.576 s. We calculate the sputtering depth in nanometers using Eq. 2.2.

$$\text{Sputtering depth} = \left(\frac{\text{sputter rate} \times \text{primary ion beam current} \times \text{sputter time}}{\text{raster area}}\right) \quad (2.2)$$

Determination of Lateral Spatial Resolution

Lateral resolution was also determined using standard procedures. The primary challenge is to find a sufficiently small or sharp edged feature so that its width is negligible relative to the primary beam diameter. To determine the spot size, a single scan of a standard sample is used. To determine the practical resolution, multiple scans of a cell sample can be used, but with the caveat that the features may not be sufficiently small or sharp to accurately characterize the beam diameter. To do this, we first collect a secondary electron image of a standard sample (256 × 256 pixels, 5 × 5 μm^2, 0.5–1 ms/pixels) or use an image that has already been collected of a cell (see above). For multi-scan images, one will need to align the NanoSIMS image planes to correct for spatial drift in the beam or the sample. The presence of image drift would compromise the lateral resolution of the resulting image. Images of high count rate species, such as $^{12}C^{14}N^-$ or secondary electrons, typically provide the best alignment for cells. Next, we calculate the effective diameter of the primary ion beam, to determine the lateral resolution of the NanoSIMS analysis. To do this, we make a line scan across a region in a secondary ion or secondary electron image where the sample composition changes abruptly. We determine the distance over which the secondary ion or electron signal intensity changes from 84% to 16% of the maximum intensity. This distance was the effective diameter of the analysis beam.[8]

Creation of ^{15}N- and ^{13}C-Enrichment Images

To accurately visualize the distribution of ^{15}N-sphingolipids and ^{13}C-lipids in the plasma membrane, the secondary ion signal must be normalized to remove ion intensity variations due to concentration-independent factors that affect ion yields and sputter rates.[28] These factors include changes in ionization probabilities related to sample composition—which is referred to as "matrix effects"—and sample topography.[29–31] Because these concentration-independent factors

influence the intensities of isotopologues, which are chemical species that differ in isotopic composition (i.e., $^{15}N^{12}C^-$, $^{14}N^{13}C^-$ and $^{14}N^{12}C^-$), to relatively the same extent, expressing the lipid-specific ion counts as a ratio to the corresponding major ion accurately represents the concentration distribution of the target molecules.[28] To minimize random noise in the images, the ratio images are typically "smoothed" over a 3 by 3 pixel window, which means the value at a given pixel is the average ratio of the 3 by 3 pixel region that is centered around that pixel.

Once again, image processing begins with aligning the image plane. For each image plane, we ratio the counts of each lipid-specific ion (e.g., $^{15}N^{12}C^-$or $^{13}C^1H^-$) detected at each pixel to the counts of the corresponding major element ion ($^{14}N^{12}C^-$ or $^{12}C^1H^-$) detected at the same pixel. We then smooth the isotope ratio measured at each pixel using a 3 by 3 pixel window. For every pixel, we calculate the mean (μ) isotope ratio ($^{15}N^{12}C^-/^{14}N^{12}C^-$ or $^{13}C^1H^-/^{12}C^1H^-$) of the individual image planes ($\mu = \Sigma x_i/N$, where N was the number of total image planes). The isotope ratio ($^{15}N^{12}C^-/^{14}N^{12}C^{14}N^-$ or $^{13}C^1H^-/^{12}C^1H^-$) was then divided by their natural abundance (0.00367 or 0.011237, respectively) to produce an enrichment factor that was a quantitative relative measure of the amount of ^{15}N-sphingolipids or ^{13}C-lipids in the plasma membrane compared to an unlabeled (natural abundance) cell. Finally, a color scale was used to encode the value of the isotope enrichment measured at each pixel in the output image with a color (Fig. 2.2).

Visual Interpretation of ^{15}N- and ^{13}C-Enrichment Images

The ^{13}C-enrichment and ^{15}N-enrichment images (Fig. 2.2) reveal the distributions of ^{13}C-labeled lipids and ^{15}N-sphingolipids in the plasma membrane. The ^{13}C-lipid distribution was used to assess the quality of cell preservation. As shown in the ^{13}C-enrichment image in Fig. 2.2, the continuity of the ^{13}C-enrichment on the cell surface confirms that the cell membrane was

intact, and the ^{13}C-lipids are not clustered within the membrane. This continuous distribution of ^{13}C-lipids on the cell surface confirms that the preservation process did not create holes in the membrane, or induce artifactual lipid clustering. Therefore, the lateral variations in the ^{15}N-enrichment on the cell surface (Fig. 2.2), which indicate that the ^{15}N-sphingolipids are heterogeneously distributed in the cell membrane, cannot be attributed to preparation-induced artifacts. Instead, the local elevations in the ^{15}N-sphingolipid enrichment that are dispersed within a continuous matrix of lower ^{15}N-sphingolipid abundance signify the presence of ^{15}N-sphingolipid domains within the plasma membrane.

Conclusions

Advances in secondary ion mass spectrometry (SIMS) now enable the distributions of isotopically labeled lipids within cellular or model membranes to be imaged with chemical specificity and high (≥50 nm) lateral resolution. Methods to image the distributions of sphingolipids within the membranes of intact cells with a Cameca NanoSIMS were described in this chapter. This includes the metabolic incorporation of distinct stable isotopes into the lipid species of interest, cell preservation, imaging conditions, and data analysis, which are all essential for lipid detection with a NanoSIMS. By using this approach to image large regions on the cell surface, the long-range organization of the sphingolipid microdomains in the plasma membrane may be visualized. The methods and principles described here can also be extended to studying other membrane lipids or cholesterol. Such work is described in the subsequent chapters.

References

(1) This research was originally published and is reprinted with kind permission from Springer Science and Business Media. Klitzing, H. A.; Weber, P. K.; Kraft, M. L. Secondary Ion Mass Spectrometry Imaging of Biological Membranes at High Spatial Resolution. In *Nanoimaging*; Sousa, A. A., Kruhlak, M. J., Eds.; Humana Press: Totowa, NJ, 2013; pp 483–501.

(2) Ostrowski, S. G.; Van Bell, C. T.; Winograd, N.; Ewing, A. G. Mass Spectrometric Imaging of Highly Curved Membranes during Tetrahymena Mating. *Science* **2004**, *305* (5680), 71–73.

(3) Piehowski, P. D.; Davey, A. M.; Kurczy, M. E.; Sheets, E. D.; Winograd, N.; Ewing, A. G.; Heien, M. L. Time-of-Flight Secondary Ion Mass Spectrometry Imaging of Subcellular Lipid Heterogeneity: Poisson Counting and Spatial Resolution. *Anal. Chem.* **2009**, *81* (14), 5593–5602.

(4) Kurczy, M. E.; Piehowski, P. D.; Van Bell, C. T.; Heien, M. L.; Winograd, N.; Ewing, A. G. Mass Spectrometry Imaging of Mating Tetrahymena Show That Changes in Cell Morphology Regulate Lipid Domain Formation. *Proc. Natl. Acad. Sci. U. S. A.* **2010**, *107* (7), 2751–2756.

(5) Anderton, C. R.; Lou, K.; Weber, P. K.; Hutcheon, I. D.; Kraft, M. L. Correlated AFM and NanoSIMS Imaging to Probe Cholesterol-Induced Changes in Phase Behavior and Non-Ideal Mixing in Ternary Lipid Membranes. *Biochim. Biophys. Acta* **2011**, *1808* (1), 307–315.

(6) Vaezian, B.; Anderton, C. R.; Kraft, M. L. Discriminating and Imaging Different Phosphatidylcholine Species within Phase-Separated Model Membranes by Principal Component Analysis of TOF-Secondary Ion Mass Spectrometry Images. *Anal. Chem.* **2010**, *82* (24), 10006–10014.

(7) Boxer, S. G.; Kraft, M. L.; Weber, P. K. Advances in Imaging Secondary Ion Mass Spectrometry for Biological Samples. *Annu. Rev. Biophys.* **2009**, *38*, 53–74.

(8) Kraft, M. L.; Weber, P. K.; Longo, M. L.; Hutcheon, I. D.; Boxer, S. G. Phase Separation of Lipid Membranes Analyzed with High-Resolution Secondary Ion Mass Spectrometry. *Science* **2006**, *313* (5795), 1948–1951.

(9) Wilson, R. L.; Frisz, J. F.; Hanafin, W. P.; Carpenter, K. J.; Hutcheon, I. D.; Weber, P. K.; Kraft, M. L. Fluorinated Colloidal Gold Immunolabels for Imaging Select Proteins in Parallel with Lipids Using High-Resolution Secondary Ion Mass Spectrometry. *Bioconjug. Chem.* **2012**, *23* (3), 450–460.

(10) Wilson, R. L.; Frisz, J. F.; Klitzing, H. A.; Zimmerberg, J.; Weber, P. K.; Kraft, M. L. Hemagglutinin Clusters in the Plasma Membrane Are Not Enriched with Cholesterol and Sphingolipids. *Biophys. J.* **2015**, *108* (7), 1652–1659.

(11) Ghosal, S.; Fallon, S. J.; Leighton, T. J.; Wheeler, K. E.; Kristo, M. J.; Hutcheon, I. D.; Weber, P. K. Imaging and 3D Elemental Characterization of Intact Bacterial Spores by High-Resolution Secondary Ion Mass Spectrometry. *Anal. Chem.* **2008**, *80* (15), 5986–5992.

(12) Garner, P.; Park, J. M. The Synthesis and Configurational Stability of Differentially Protected .beta.-Hydroxy-.alpha.-Amino Aldehydes. *J. Org. Chem.* **1987**, *52* (12), 2361–2364.

(13) Garner, P.; Park, J. M.; Malecki, E. A Stereodivergent Synthesis of D-Erythro-Sphingosine and D-Threo-Sphingosine from L-Serine. *J. Org. Chem.* **1988**, *53* (18), 4395–4398.

(14) Mckillop, A.; Taylor, R. J. K.; Watson, R. J.; Lewis, N. An Improved Procedure for the Preparation of the Garner Aldehyde and Its Use for the Synthesis of *N* -Protected 1-Halo-2-(*R*)-Amino-3-Butenes. *Synthesis* **1994**, *1994* (01), 31–33.

(15) Peters, C.; Billich, A.; Ghobrial, M.; Högenauer, K.; Ullrich, T.; Nussbaumer, P. Synthesis of Borondipyrromethene (BODIPY)-Labeled Sphingosine Derivatives by Cross-Metathesis Reaction. *J. Org. Chem.* **2007**, *72* (5), 1842–1845.

(16) Roush, W. R.; Hunt, J. A. Asymmetric Allylboration of 2-N,3-O-Isopropylidene-N-Boc-L-Serinal: Diastereoselective Synthesis of the Calicheamicin .gamma.1I Amino Sugar. *J. Org. Chem.* **1995**, *60* (4), 798–806.

(17) Bligh, E. G.; Dyer, W. J. A Rapid Method of Total Lipid Extraction and Purification. *Can. J. Biochem. Physiol.* **1959**, *37* (8), 911–917.

(18) Zhu, L.; Johnson, C.; Bakovic, M. Stimulation of the Human CTP:phosphoethanolamine Cytidylyltransferase Gene by Early Growth Response Protein 1. *J. Lipid Res.* **2008**, *49* (10), 2197–2211.

(19) Keller, P.; Simons, K. Cholesterol Is Required for Surface Transport of Influenza Virus Hemagglutinin. *J. Cell Biol.* **1998**, *140* (6), 1357–1367.

(20) Campbell, S.; Gaus, K.; Bittman, R.; Jessup, W.; Crowe, S.; Mak, J. The Raft-Promoting Property of Virion-Associated Cholesterol, but Not the Presence of Virion-Associated Brij 98 Rafts, Is a Determinant of Human Immunodeficiency Virus Type 1 Infectivity. *J. Virol.* **2004**, *78* (19), 10556–10565.

(21) Scheiffele, P.; Rietveld, A.; Wilk, T.; Simons, K. Influenza Viruses Select Ordered Lipid Domains during Budding from the Plasma Membrane. *J. Biol. Chem.* **1999**, *274* (4), 2038–2044.

(22) Chigorno, V.; Riva, C.; Valsecchi, M.; Nicolini, M.; Brocca, P.; Sonnino, S. Metabolic Processing of Gangliosides by Human Fibroblasts in Culture--Formation and Recycling of Separate Pools of Sphingosine. *Eur. J. Biochem. FEBS* **1997**, *250* (3), 661–669.

(23) Dolo, V.; D'Ascenzo, S.; Sorice, M.; Pavan, A.; Sciannamblo, M.; Prinetti, A.; Chigorno, V.; Tettamanti, G.; Sonnino, S. New Approaches to the Study of Sphingolipid Enriched Membrane Domains: The Use of Microscopic Autoradiography to Reveal Metabolically Tritium Labeled Sphingolipids in Cell Cultures. *Glycoconj. J.* **2000**, *17* (3-4), 261–268.

(24) Van Echten, G.; Birk, R.; Brenner-Weiss, G.; Schmidt, R. R.; Sandhoff, K. Modulation of Sphingolipid Biosynthesis in Primary Cultured Neurons by Long Chain Bases. *J. Biol. Chem.* **1990**, *265* (16), 9333–9339.

(25) Schwarzmann, G.; Hoffmann-Bleihauer, P.; Schubert, J.; Sandhoff, K.; Marsh, D. Incorporation of Ganglioside Analogues into Fibroblast Cell Membranes. A Spin-Label Study. *Biochemistry (Mosc.)* **1983**, *22* (21), 5041–5048.

(26) Cheng, J.; Fujita, A.; Ohsaki, Y.; Suzuki, M.; Shinohara, Y.; Fujimoto, T. Quantitative Electron Microscopy Shows Uniform Incorporation of Triglycerides into Existing Lipid Droplets. *Histochem. Cell Biol.* **2009**, *132* (3), 281–291.

(27) Edidin, M. Lipids on the Frontier: A Century of Cell-Membrane Bilayers. *Nat. Rev. Mol. Cell Biol.* **2003**, *4* (5), 414–418.

(28) Peteranderl, R.; Lechene, C. Measure of Carbon and Nitrogen Stable Isotope Ratios in Cultured Cells. *J. Am. Soc. Mass Spectrom.* **2004**, *15* (4), 478–485.

(29) Williams, P. Biological Imaging Using Secondary Ions. *J. Biol.* **2006**, *5* (6), 18.

(30) Kumar, S.; Aaron, J.; Sokolov, K. Directional Conjugation of Antibodies to Nanoparticles for Synthesis of Multiplexed Optical Contrast Agents with Both Delivery and Targeting Moieties. *Nat. Protoc.* **2008**, *3* (2), 314–320.

(31) Rangarajan, S.; Tyler, B. J. Topography in Secondary Ion Mass Spectroscopy Images. *J. Vac. Sci. Technol. A* **2006**, *24* (5), 1730–1736.

Figures and Tables

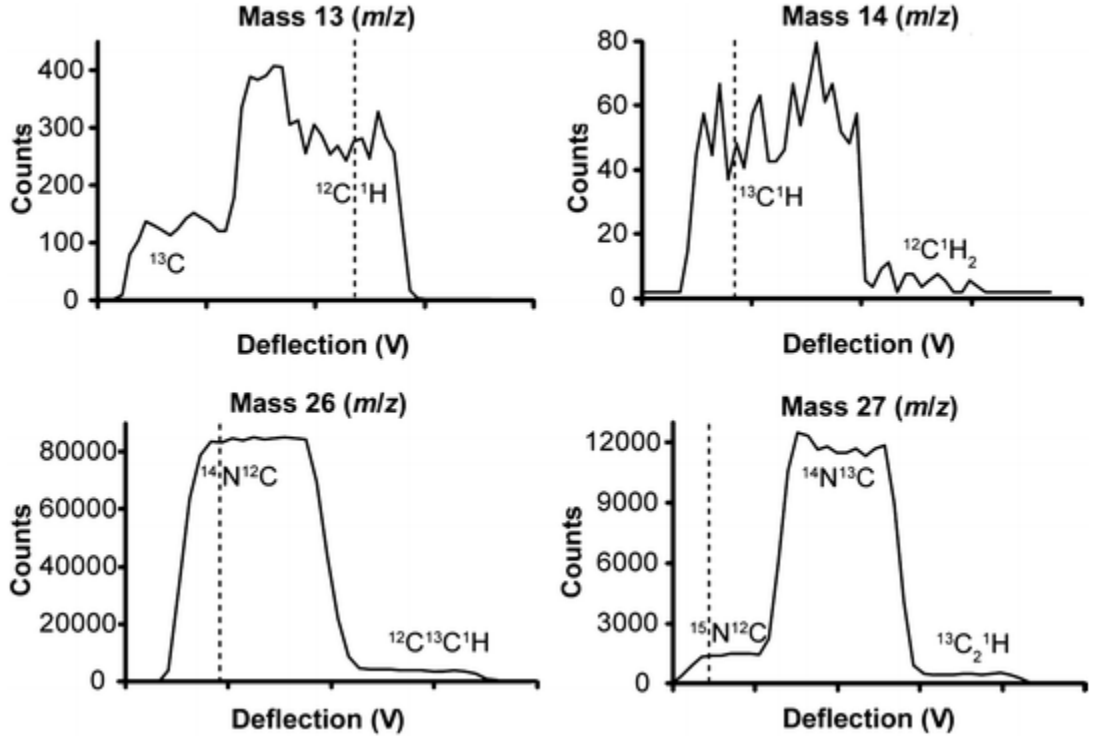

Figure 2.1 Mass spectra acquired with ~11,000 MRP and 75 μm-width slits in front of the detectors. The analyzed cell was isotopically enriched in ^{13}C and ^{15}N. The ions of interest and some of the interfering isobars at *m*/*z* 13, *m*/*z* 14, *m*/*z* 26, and *m*/*z* 27 are indicated. The individual masses are not resolved in these scans, but by setting the deflection on each detector as indicated with the dashed lines, the contribution of the interfering isobars was less than 0.1% of the species of interest. Several species are too low in abundance to be visible in the mass spectra (*see* Table 2.1 for the full list of interferences at *m*/*z* 26 and 27).

Calculated clusters	m/e (u)	Δ (mu)	Abundance	MRP
At mass 26				
^{12}C–^{14}N	26.0025	0.0	0.98538	–
^{13}C–^{13}C	26.0062	3.6	0.00012	7,155
^{10}B–^{16}O	26.0073	4.8	0.19853	5,443
^{1}H–^{12}C–^{13}C	26.0106	8.1	0.01088	3,208
^{1}H–^{1}H–^{12}C–^{12}C	26.0151	12.6	0.97783	2,068
At mass 27				
^{12}C–^{15}N	26.9996	0.0	0.00362	–
^{11}B–^{16}O	27.0037	4.1	0.79909	6,567
^{13}C–^{14}N	27.0059	6.3	0.01096	4,272
^{1}H–^{12}C–^{14}N	27.0104	10.8	0.98523	2,502
^{1}H–^{13}C–^{13}C	27.0140	14.4	0.00012	1,872
^{1}H–^{1}H–^{12}C–^{13}C	27.0185	18.9	0.01088	1,429
^{1}H–^{1}H–^{13}C–^{12}C	27.0185	18.9	0.01088	1,429

Table 2.1 Mass Interferences

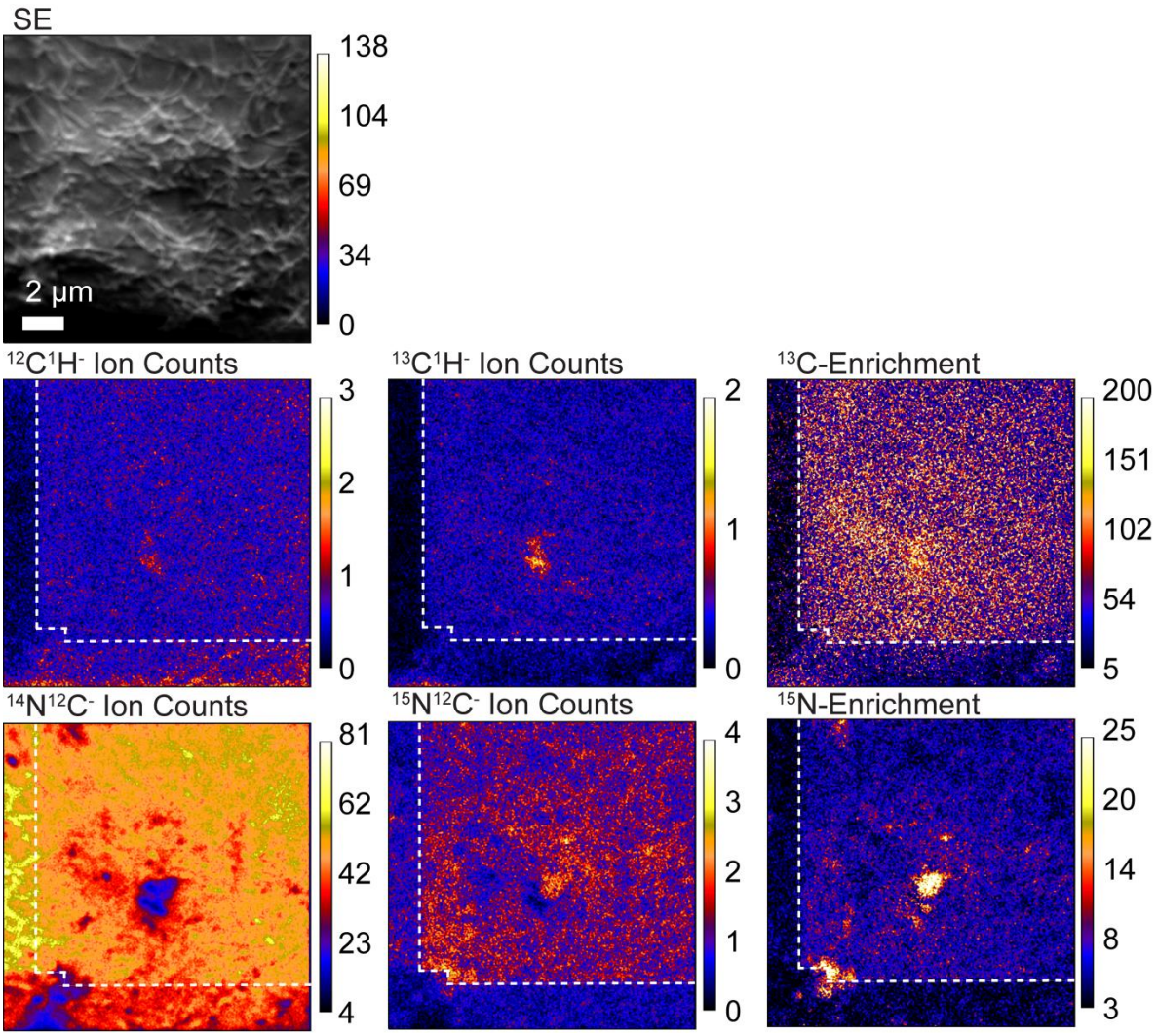

Figure 2.2 NanoSIMS images acquired from a fibroblast cell. The secondary electrons were acquired in parallel with the $^{12}C^{1}H^{-}$, $^{13}C^{1}H^{-}$, $^{14}N^{12}C^{-}$ and $^{15}N^{12}C^{-}$ secondary ions. To image the entire cell at this lateral resolution, multiple overlapping images are required. Low ion counts at edges of images (below and to the left of the *dashed lines*) are characteristic of previously analyzed locations. The ^{13}C-enrichment (($^{13}C^{1}H^{-}/^{12}C^{1}H^{-}$)/0.011237) and ^{15}N-enrichment (($^{15}N^{12}C^{-}/^{14}N^{12}C^{-}$)/0.00367) images reveal the distributions of ^{13}C-labeled lipids and ^{15}N-sphingolipids in the plasma membrane. The secondary ion and enrichment images were smoothed over 3 by 3 pixels.

CHAPTER 3.
DIRECT CHEMICAL EVIDENCE OF SPHINGOLIPID DOMAINS ALLOWS FOR FURTHER CHARACTERIZATION

Notes and Acknowledgements[3]

This chapter features portions of work which originally appeared in two different sources and has been reprinted with permissions from: *Proceedings of the National Academy of Sciences*

[3] This chapter features portions of work which originally appeared in two publications and has been reprinted with permission from:

1. *Proceedings of the National Academy of Sciences, USA*. Frisz, J. F.; Lou, K.; Klitzing, H. A.; Hanafin, W. P.; Lizunov, V.; Wilson, R. L.; Carpenter, K. J.; Kim, R.; Hutcheon, I. D.; Zimmerberg, J.; et al. Direct Chemical Evidence for Sphingolipid Domains in the Plasma Membranes of Fibroblasts. *Proc. Natl. Acad. Sci.* **2013**, *110* (8), E613–E622.
2. *Journal of Biological Chemistry*. Frisz, J. F.; Klitzing, H. A.; Lou, K.; Hutcheon, I. D.; Weber, P. K.; Zimmerberg, J.; Kraft, M. L. Sphingolipid Domains in the Plasma Membranes of Fibroblasts Are Not Enriched with Cholesterol. *J. Biol. Chem.* **2013**, *288* (23), 16855–16861.

The publication in the *Proceedings of the National Academy of Sciences of the USA* was co-authored by Haley A. Klitzing, Jessica F. Frisz, William P. Hanafin, Vladimir Lizunov, Robert L. Wilson, Kevin J. Carpenter, Raehyun Kim, Ian D. Hutcheon, Joshua Zimmerberg, Peter K. Weber, and Mary L. Kraft. Individual contributions to this work are: HAK prepared and characterized temperature control samples with NanoSIMS, and analyzed the data. JFF prepared and characterized cells, assisted with NanoSIMS analysis, and performed data analysis. KL synthesized the ^{15}N-labeled sphingolipid precursors and developed the metabolic labeling protocols and isotope incorporation assay. WPH cultured cells used for control experiments. VL performed fluorescence experiments. RK assisted with designing the fluorescent experiments and prepared the fluorescent lipid. IDH assisted with designing the NanoSIMS analysis. JZ provided the Clone 15 line, planned experiments, and assisted with data interpretation. PKW planned experiments, and assisted with NanoSIMS analysis and data interpretation. MLK planned experiments, developed statistical tools for data analysis and assisted with NanoSIMS analysis and data interpretation.

The publication in the *Journal of Biological Chemistry* was co-authored by Haley A. Klitzing, Jessica F. Frisz, Kaiyan Lou, Ian D. Hutcheon, Peter K. Weber, Joshua Zimmerberg, and Mary L. Kraft. Individual contributions to this work are: HAK prepared and characterized cytoskeletal disruption cell samples, assisted with NanoSIMS, and performed data analysis. JFF prepared and characterized cholesterol-labeled cells, assisted with NanoSIMS analysis, and performed data analysis. KL synthesized the isotope-labeled metabolic precursors, and developed assays for isotope incorporation. IDH assisted with experimental design. PKW assisted with experimental design, NanoSIMS analysis, and data interpretation. JZ provided the Clone 15 cell line, planned experiments, and assisted with data interpretation. MLK planned experiments, assisted with NanoSIMS analysis, developed statistical tools, and assisted with data interpretation.

of the United States of America (Copyright 2013 National Academy of Sciences, USA.),[1] and *Journal of Biological Chemistry* (© the American Society for Biochemistry and Molecular Biology).[2]

We thank A. Ulanov for his valuable comments on the evaluation of isotope incorporation, C. Ramon for technical assistance, and L. Nittler for software development. MLK holds a Career Award at the Scientific Interface from the Burroughs Wellcome Fund. Portions of this work were carried out in the Metabolomics Center in the Roy J. Carver Biotechnology Center, Univ. of Illinois, and in the Frederick Seitz Materials Research Laboratory Central Facilities, Univ. of Illinois, which are partially supported by the U.S. Department of Energy (DOE) under grants DE-FG02-07ER46453 and DE-FG02-07ER46471. Work at Lawrence Livermore National Laboratory was supported by Laboratory Directed Research and Development funding and performed under the auspices of the U.S. DOE under contract DE-AC52-07NA27344. This material was supported in part by the National Science Foundation under CHE—1058809.

Introduction

Spatial organization of the lipids and proteins in the plasma membranes of eukaryotic cells is critical to coordinating lipid signaling and numerous other processes that occur at the cell surface.[3] Thus, the hypothesis that lipids self-organize in compositionally and functionally distinct plasma membrane domains has been investigated for decades.[4] Microdomains with a variety of lipid compositions and dependencies on lipid and protein interactions may exist in the plasma membrane,[5–7] but the most compelling lipid microdomain is the lipid raft because such domains self-assemble in synthetic membranes.[8,9] Lipid rafts are defined as dynamic and small (10- to 200-nm) plasma membrane domains that are enriched with cholesterol and sphingolipids.[8,9] Despite intense research, the distributions of most lipid species, including cholesterol and sphingolipids, in cellular membranes are still difficult to determine.[9] The ability to directly visualize specific lipid species without the use of potentially perturbing tags would help to address outstanding questions regarding distinct lipid domains in the plasma membrane.[9–11]

Here we use a high-resolution chemical imaging approach to address the question: How are sphingolipids distributed in the plasma membranes of intact cells? We focused on sphingolipids because (*i*) they are postulated to be segregated within compositionally distinct lipid domains, such as lipid rafts,[12–14] and (*ii*) sphingolipid metabolites are signaling molecules that regulate cell survival and proliferation.[15] We studied a transfected mouse fibroblast cell line that stably expresses influenza hemagglutinin (Clone 15 cell line) because the hemagglutinin clusters in their plasma membranes are thought to be associated with sphingolipid and cholesterol domains.[12–14] Thus, we hoped to increase the probability of detecting sphingolipid-enriched plasma membrane domains by using the Clone 15 cell line.

To visualize the sphingolipids within the plasma membrane, we isotopically labeled them and then mapped their distributions in the plasma membrane, using a secondary ion mass spectrometry (SIMS) instrument (Cameca NanoSIMS 50) with 50-nm lateral resolution and an analysis depth of <5 nm at the cell surface;[16–18] this analysis depth is less than the thickness of the plasma membrane. Previous reports establish that NanoSIMS imaging does not alter biomolecule distribution within subcellular compartments or lipid membranes.[16,19–21] Thus, this approach enabled us to quantitatively determine the sphingolipid organization. Sphingolipids were segregated in ∼200-nm diameter microdomains that nonrandomly clustered into sphingolipid-rich plasma membrane patches with micrometer-scale dimensions. Sphingolipid organization was not altered by chemical fixation or cell preservation temperatures, but treatments of the plasma membranes, such as with latrunculin-A, show a measurable effect on sphingolipid distribution in the plasma membrane.

Methods and Materials

Materials

Uniformly ^{13}C-labeled (98 atom%) fatty acids were from CambridgeIsotope Laboratories. Fatty acid-free bovine serum albumin (FAFBSA) and $^{13}C_{18}$-stearic acid (99 atom% ^{13}C) were from Sigma. Lipid-reduced fetal bovine serum (LR-FBS) and calf serum were from HyClone Laboratories. Poly-L-lysine and fixation reagents were from Electron Microscopy Sciences. Standard cell growth medium consisted of high-glucose Dulbecco's modification of Eagle's medium (DMEM) supplemented with 10% (vol/vol) calf serum, 10^4 units/mL penicillin G, and 10 mg/mL streptomycin. BODIPY-sphingosine and ^{15}N-sphingolipid precursors (^{15}N-sphingosine and ^{15}N-sphinganine, 1:1 molar ratio) were synthesized as reported in refs.[22–24] Latrunculin A for cytoskeleton disruption was from Cayman Chemical. The Clone 15 cell line

was obtained by standard techniques for selecting stably transfected cells after transient expression in a NIH 3T3 mouse fibroblast line with a DNA plasmid for the hemagglutinin from the 1957 pandemic Japan strain of influenza.

Metabolic Labeling of Cells

Cells were metabolically labeled as was previously described in Chapter 2.

Depolymerization of Actin Cytoskeleton

After metabolic labeling of the cells is complete, substrates with their adherent cells are removed from the cell culture and placed into culture dishes containing Media B and 0.83 μM of latrunculin A. After 30 min of exposure, substrates are removed, and the latrunculin A-treated cells are chemically preserved as described below. Control cells were generated by culturing cells in the presence of dimethyl sulfoxide (the solvent for latrunculin A) instead of latrunculin A. The effects of latrunculin A were visually confirmed through the use of a light microscopy as well as secondary electron microscopy (SEM).

Evaluation of Label Incorporation

The evaluation of the isotopic label content in cell samples was performed as previously described in Chapter 2. This information includes specifics on lipid extraction from cells, liquid chromatography mass spectrometry settings, and gas chromatography mass spectrometry settings as well as other pertinent information.

Cell Preservation with Chemical Fixation

Imaging with the NanoSIMS is performed under ultrahigh vacuum conditions, so the cells must be dehydrated without perturbing the lateral distributions of lipids and proteins within the cell membrane. This was accomplished by chemically preserving the cells. The method described here is derived from protocols used to chemically fix cells in order to prepare them for

analysis with SEM. This chemical fixation procedure produces a membrane whose morphology is retained during the inevitable drying process needed for introduction into the vacuum of the SIMS analysis chamber.[25] In this method, chips with adherent cells are removed from cell culture and rinsed three times with Hendry's Phosphate Buffer (HPB) for 3 min each. Care was taken so as not to disturb the attached cells. The chips were flooded with 4% glutaraldehyde and allowed to fix for 30 min. The glutaraldehyde was then removed, and the chips were rinsed twice with HPB for 5 min each, followed by rinsing once with water for 5 min. They were then fixed and stained with freshly diluted, freshly filtered 1% osmium tetroxide for 15 min. The osmium tetroxide was removed, and the chips were rinsed three times for 5 min each with water. Excess water was removed; the samples were allowed to air dry, and were then stored at room temperature. This preservation protocol was performed either at room temperature or at biological temperature (37°C). In order to achieve biological conditions, fixation reagents (buffers, glutaraldehyde, osmium tetroxide, water) were pre-warmed to 37°C. During the fixation process, the cells were kept in an incubator to ensure the appropriate temperature. After the final rinses with water, the samples were allowed to air dry and then stored at room temperature.

Low-voltage SEM

SEM imaging was performed using a Hitachi S-4800 SEM. Low voltage was used to avoid sample charging and to prevent damage. SEM imaging at higher than 5 kV damages the sample. This damage is visible as cracks on the cells. Making small rasters on the sample, such as for higher magnification, can also cause damage in the form of the decomposition of molecules at the surface of the cell. Images of individual cells were acquired at a low magnification (500–1,100×), and which cells were imaged with SEM was indicated on the optical map of the chip.

Formation of Thin Iridium Layer on Cell Samples.

To prevent charging during NanoSIMS analysis, a Cressington 208HR High-Resolution Sputter Coater equipped with a low-voltage planar magnetron sputter head, a rotary-planetary-tilting stage, and a Cressington MTM-20 High-Resolution Thickness Controller was used to produce the 3-nm-thick iridium coatings on the cells. The sample stage was rotated and tilted approximately ±30° during the entire metal sputtering process to minimize variations in the iridium coating thickness that might be caused by sample topography. To reduce the amount of impurities present in the resulting iridium metal coating on the samples, high-purity (99.95%) iridium was used as the source, and the source was presputtered to remove surface contamination before opening the shutter.

SIMS Analysis

SIMS was performed on a Cameca NanoSIMS 50 at Lawrence Livermore National Laboratory with a 0.129-pA, 15-keV $^{133}Cs^{+}$ primary ion beam focused onto a 69-nm spot. Four replicate scans of 512 × 512 pixels with a dwell time of 1 ms/pixel were acquired for each 15 × 15-µm analysis region, resulting in a pixel size (29 × 29 nm) smaller than the beam diameter. The $^{12}C^{1}H^{-}$, $^{13}C^{1}H^{-}$, $^{12}C^{14}N^{-}$, and $^{12}C^{15}N^{-}$ secondary ions, and secondary electrons, were simultaneously collected. A mass resolving power of ~6,700 was used to separate isobaric interferences from the isotopes of interest, e.g., $^{12}C^{15}N^{-}$ from $^{13}C^{14}N^{-}$ at mass 27. The primary ion dose was 4.5×10^{14} ions/cm^{2}.

Data Analysis

NanoSIMS data were processed with a custom software package (L'image; L. R. Nittler, Carnegie Institution of Washington, Washington, DC) run with PV-Wave (Visual Numerics; presently known as Rogue Wave). Quantitative ^{15}N- and ^{13}C-enrichment images showing the ^{15}N-

sphingolipid and ^{13}C-lipid distributions, respectively, were constructed using a 3 × 3-pixel moving average smoothing algorithm. Isotope enrichment is the $^{12}C^{15}N^{-}/^{12}C^{14}N^{-}$ or $^{13}C^{1}H^{-}/^{12}C^{1}H^{-}$ ratio divided by standard natural abundance ratios (0.00367 and 0.011237, respectively). The MATLAB statistics toolbox was used to determine the statistically significant thresholds for ^{15}N-enrichment and to perform Kolmogorov-Smirnov tests for statistically significant differences in the ^{15}N-sphingolipid domains.

Analysis of Sphingolipid Domain Organization

The clustering of the domains on the cell body was assessed using the SpatStat spatial statistics package (version 1.22-1) run in the R program (version 2.12.2).[26,27] The x–y coordinates for the cell body were recorded by loading the montage of secondary electron images of the cell into GraphClick 3.0 and tracing the edges of the cell body but omitting the lamellipodia. The coordinates for the cell body were expressed in pixel units and were used to define the observation window in SpatStat. The x–y coordinates of the domain centers with respect to the whole cell were calculated from the coordinates of the pixels where the domain centers were located within each ^{15}N-enrichment image (exported from L'image) and the coordinates of each ^{15}N-enrichment image in the montage of the whole cell. These coordinates were used to create a point pattern that represented the observed domains within the observation window that corresponded to the cell body.

Ripley's K-test was performed on the point pattern corresponding to the domain centers, using translation edge correction to calculate the number of domains within a radius, r, of any domain on the cell surface.[28,29] Analysis was restricted to distances less than one-quarter of the smallest length of the observation window. Data were normalized to the 99% confidence interval, calculated according to

$$CI_{99} = 1.68\sqrt{A/N} \quad (3.1)$$

A is the area of the observation window and N is the total number of domains within the window.

For comparison with the experimental domains observed on the cell surface, we simulated a population of spatially random domains within the observation window that represented the cell body. The number and effective diameters of the domains in the simulated population were identical to those that were experimentally observed on the cell body. We first determined the frequency distribution of effective domain diameters experimentally observed on the cell body, using a bin size of 1 pixel. We tabulated the number of domains with a specified effective diameter that were experimentally observed on the cell body. An algorithm was used to randomly add domains ("points") with the specified effective diameter (encoded as a "mark") one-by-one to the observation window that represented the cell body. New domains were generated independent of the preceding domains, and those that lay outside of the observation window were rejected. To prevent the domains from overlapping, the simulated domains were also rejected if the distance between the center of the simulated domain and the center of the closest domain was less than the sum of the radii of the two domains. Once the number of domains with a given diameter in the observation window equaled that experimentally observed on the cell body, the process was repeated for the next effective domain diameter. These steps were repeated until the correct number of domains had been simulated for every observed effective diameter.

The nearest neighbor distance, which is the distance from the center of each domain to the center of its nearest neighbor, was computed for each of the (i) experimentally observed domains on the cell body and (ii) simulated, spatially random domains. For each population (e.g.,

experimental and simulated), the frequency distribution of nearest neighbor domain distances was tabulated using a bin size of 50 nm and normalized to the total number of domains in the population to produce the fraction of the total. The difference between the frequencies of observed and simulated nearest neighbor distances was calculated by subtracting the fraction of the simulated domain population with nearest neighbor distances within each 50-nm increment from the fraction of experimentally observed domains with nearest neighbor distances in the same range. The differences between the frequencies of observed and simulated nearest neighbor distances are plotted in Fig. 3.6F.

The pairwise domain distances, which are the distances between the center of each domain and the center of every other domain on the cell body, were computed for (i) every domain that was experimentally observed and (ii) every domain within the simulated population. The frequency distributions of pairwise domain distances for the experimental and simulated domains on each cell were tabulated using a bin size of 0.5 μm and normalized to the total number of domains in the population. The difference between the frequencies of observed and simulated pairwise domain distances was calculated for each 0.5-μm increment and is plotted in Fig. 3.6G.

SIMS Analysis of ^{13}C-Lipid Dstribution Throughout the Cell.

A series of 36 NanoSIMS ^{13}C-enrichment images were sequentially acquired at the same sample position on a representative Clone 15 cell that was metabolically labeled and prepared as previously described. To permit analysis of the cytoplasm, the NanoSIMS operating conditions were adjusted so that the sampling depth was approximately four times greater than that used to acquire the rest of the NanoSIMS images presented herein. All other analysis conditions remained constant. Approximately 1.3 nm of material was sputtered from the sample surface

each time an image was acquired. The resulting data provided a depth profile of the cell at that location.

Results

NanoSIMS Images Show Sphingolipid-Enriched Domains in the Plasma Membrane

Secondary electron images of the Clone 15 fibroblast cells were collected simultaneously to the secondary ions to allow the isotopic data to be related to cell location and morphology (Fig. 3.1). The high levels of ^{15}N-isotope incorporation into the cellular sphingomyelin allowed the location and density of sphingolipids in the membrane to be mapped with a high signal-to-noise ratio. Local elevations in ^{15}N-enrichment were dispersed within a matrix of lower ^{15}N-enrichment on the surfaces of the Clone 15 cells (Fig. 3.2). Control experiments excluded the possibilities that these local elevations in ^{15}N-enrichment were artifacts induced by cell topography, the iridium coating, or isotope-labeled material adsorbed to the cell. Consequently, these local elevations in ^{15}N-enrichment are plasma membrane domains enriched with ^{15}N-sphingolipids. These sphingolipid microdomains were detected on every one of over 25 other cells studied. Based upon the analysis of 59,301 3 × 3-pixel subregions on the Clone 15 cell shown in Fig. 3.2, a ^{15}N-enrichment factor ≥12 is at least 2 SD above the mean ^{15}N-enrichment factor for the domain-free regions (mean ^{15}N-enrichment factor for domain-free regions = 7.8, 1 SD = 2.1) and therefore represents a statistically significant elevation in the plasma membrane's local ^{15}N-sphingolipid enrichment. The ^{15}N-sphingolipid–enriched domains on this cell (Fig. 3.2) and others (Table 3.1) were more abundant on the main body of the cell than on its extensions. Debris on the substrate near the cell was also enriched with ^{15}N-sphingolipids, consistent with reports that fibroblasts deposit lipids along with other cellular material when migrating.[30]

Because the ^{15}N-sphingolipid assemblages were larger than expected, we carefully inspected the ^{13}C-lipid distribution shown in the ^{13}C-enrichment images for signs of membrane defects or spatially dependent variations in detection sensitivity. The specificity of the elevated ^{13}C-enrichment to ^{13}C-lipids was confirmed by its localization at the surfaces of identically labeled cells and at distinct regions in their cytoplasm that likely correspond to organelle membranes (Fig. 3.4). Therefore, the continuously elevated ^{13}C-enrichments detected on the Clone 15 cells in Fig. 3.3 and Fig. 3.4 confirm their plasma membranes were intact, and the regions of lower ^{15}N-sphingolipid abundance are not artifacts of membrane damage. The absence of statistically significant variations in the ^{13}C-enrichment on the surfaces of the cells as a function of distance from the nucleus indicates the analysis sensitivity was laterally uniform. Finally, we tested whether the local elevations in ^{15}N-sphingolipid abundance reflected an excess of all cellular lipids, which could be caused by intracellular membranes adjacent to the plasma membrane or fixation-induced lipid aggregates. An excess of cellular lipids at the sites of ^{15}N-sphingolipid enrichment produces a concomitant statistically significant elevation in the ^{13}C-enrichment (not shown). For the Clone 15 cell shown in Fig. 3.2, the ^{13}C-enrichment factors in the domains are not statistically higher than in the nondomain regions (Kolmogrov–Smirnov test, $h = 0$, $P = 0.60$). This confirms the local ^{15}N-sphingolipid enrichment in the plasma membrane was not caused by intracellular membranes or artifactual lipid clustering.

Sphingolipid Organization Is Not Altered by Chemical Fixation.

We investigated the possibility that our fixation procedure altered the sphingolipid distribution in the plasma membrane. Control experiments were performed to test whether room temperature fixation or any other unavoidable exposure to subphysiological temperatures before fixation caused nanoscale sphingolipid domains to coalesce into the assemblages we observed

with SIMS. Low temperatures can induce phase separation in model membranes and sphingolipid clustering in the plasma membranes of unfixed cells.[31,32] This redistribution of lipids does not occur when the cells are preserved with aldehyde fixatives similar to those we used before their exposure to subphysiological temperatures.[31] Thus, lipid rearrangement could have occurred in our experiments only when the cells were removed from their incubator and subsequently exposed to room temperature (RT) glutaraldehyde solution. We compared Clone 15 cells that were chemically fixed with RT and 37 °C glutaraldehyde solutions. The ^{15}N-sphingolipid microdomains on the cells fixed at 37 °C (Fig. 3.5) were similar in appearance to those in the membranes of cells fixed at RT. Thus, RT fixation did not induce the formation of ^{15}N-sphingolipid domains in the plasma membrane.

To assess whether RT fixation increased the size or abundance of the ^{15}N-sphingolipid domains on the cell surface, we compared the mean sphingolipid domain size and surface coverage on cells fixed with RT and 37 °C glutaraldehyde solutions. By visual inspection, both sets of cells exhibited ^{15}N-sphingolipid–enriched plasma membrane domains with circular and oblong morphologies, where the domain's longest axis ranged from ~200 nm to 2 μm. By using a particle definition algorithm to quantitatively define the sphingolipid domains, we determined each Clone 15 cell that was fixed at 37 °C had >1,400 sphingolipid-enriched domains that covered 8–13% of the cell surface (Table 3.1). Similar sphingolipid domain surface coverage was measured on each Clone 15 cell fixed at RT (9–15%). Because the majority of the sphingolipid domains were oblong (Fig. 3.6 *A*–*C*), we quantified their area and equivalent diameter, which is the diameter of a circular region with the same area. The sphingolipid domains on the cells fixed with RT glutaraldehyde solution had mean areas between 0.029 and 0.038 μm^2 and mean equivalent diameters between 180 and 205 nm (Table 3.1). Similar

sphingolipid domain areas and diameters were measured on the cells fixed at 37 °C (Fig. 3.6 and Table 3.1). Thus, the glutaraldehyde fixation temperature and kinetics did not affect the surface coverage or size of the sphingolipid domains.

Sphingolipid Organization is Dependent on the Cytoskeleton

We probed the hypothesis that the cytoskeleton and its associated proteins control membrane lipid organization. We disrupted the cytoskeleton in Clone 15 cells by exposing them to the actin-depolymerizing drug, latrunculin A,[33] and assessed the effects on the sphingolipid domains in the plasma membrane. The extensive rounding of the cell shown in the NanoSIMS secondary electron images (Fig. 3.7*A*) confirms the latrunculin A treatment disrupted the cytoskeleton in this Clone 15 cell. In contrast to the cells with intact cytoskeletons, the ^{15}N-sphingolipids on the body of the latrunculin A–treated cell were not enriched within micrometer-scale domains and instead appeared to be randomly distributed (Fig. 3.7*B*). Only a few ^{15}N-sphingolipid aggregates that approach the dimensions of the large ^{15}N-sphingolipid domains observed on the untreated Clone 15 cells are visible on the mesh of thin extensions that stem from the rounded cell body. The ^{13}C-lipids were fairly evenly distributed on the cell surface, although lower abundances of ^{13}C-lipids were detected at the lower left and right sides of the rounded cell body. The presence of ^{13}C-lipids on the substrate adjacent to the cell body suggests that membrane fragments detached from the cell when rounding occurred (Fig. 3.7*C*). The reproducibility of these results was tested across cell lines (Fig. 3.8) On the basis of these results, we conclude that an intact cytoskeleton is obligatory for sphingolipid-enriched plasma membrane domains. This type of finding illustrates the usefulness of SIMS imaging as a means for elucidating biological questions.

Discussion and Conclusion

We can now refute the hypotheses that sphingolipid-enriched domains in the plasma membrane are nanoscopic or nonexistent,[9–11] as we have directly imaged domains of sphingolipids on the dorsal surfaces of intact cells by combining metabolic labeling with high-resolution SIMS. Sphingolipids are enriched within ~200-nm diameter membrane microdomains that cluster into larger domains primarily within 5- to 10-μm diameter patches on the cell body. These sphingolipid domains are highly dependent on the cytoskeleton. These domains cannot be attributed to label-induced perturbations in molecular interactions or sphingolipid trafficking because the ^{15}N-sphingolipids we imaged were biosynthesized by the cell and they have the same chemical structure as native sphingolipids. Although we acquired chemical images of fixed cells, our data indicate that they represent snapshots of the sphingolipid organizations that were present in living Clone 15 cells. This conclusion is supported by (*i*) exclusion of artifactual elevations in the local ^{15}N-sphingolipid abundance caused by vesicles adjacent to the membrane; (*ii*) exclusion of temperature-induced sphingolipid reorganization during preservation; and *(iii)* analytical controls. These experiments lay to rest the debate over the existence of compositionally distinct lipid domains in the plasma membrane that has been in the literature for decades and lead us to reject models of membrane organization that feature spatially homogeneous lipid compositions.

We undertook this study with Clone 15 cells because we expected these cells contained sphingolipid domains that could be detected with NanoSIMS. This expectation was based on the hypothesis that the micrometer-scale patches of darkly staining membrane lipids associated with the influenza hemagglutinin clusters were cholesterol- and sphingolipid-enriched rafts that coalesced due to favorable interactions with hemagglutinin.[12,14] We successfully detected sphingolipid domains in the plasma membranes of the Clone 15 cells. Moreover, the properties

of the sphingolipid domains we observed, which include their micrometer-scale dimensions and their distribution on the cell, are inconsistent with those of lipid rafts. Nonrandom sphingolipid clustering was drastically affected by cytoskeleton disruption. On the basis of reports of a size difference between GM1 and GM3 domains and their segregation from one another,[6,34,35] we expect that the plasma membrane contains multiple types of microdomains that differ in sphingolipid subspecies composition and size. Accordingly, the micrometer-scale sphingolipid patches we observed in the Clone 15 cells likely consist of microdomains that are each enriched with a different sphingolipid subspecies. Further studies involving the simultaneous imaging of numerous sphingolipid subspecies are required to test these hypotheses.

If the plasma membrane contains sphingolipid domains with up to micrometer-scale dimensions, why are sphingolipid-enriched plasma membrane domains widely expected to have diameters below 200 nm? The expectation of nanometer-scale sphingolipid domains is primarily based on the assumption that all sphingolipid domains are lipid rafts, which are defined as nanoscale domains that are enriched with sphingolipids, cholesterol, and glycosylphosphatidylinositol(GPI)-anchored proteins.[8,9] Consequently, consideration must be given to how raft size has been deduced. Because cohesive interactions between cholesterol, sphingolipids, and GPI-anchored proteins are postulated to induce lipid raft formation, domain sizes <200 nm have been inferred from the cholesterol-dependent clustering and diffusion of GPI-anchored proteins and sphingolipids.[34,36–38] However, numerous studies have demonstrated that the clustering and hindered diffusion of GPI-anchored proteins and lipids are regulated by cortical actin organization.[6,39–42] The indirect relationship between cholesterol-dependent biophysical properties and the local lipid composition in the plasma membrane renders inferring sphingolipid domain size from biophysical behavior less reliable than directly imaging the

sphingolipid components. Visualization of sphingolipid distribution via use of fluorescently labeled sphingolipid analogs or sphingolipid-specific affinity labels has revealed plasma membrane domains that differ in sphingolipid subspecies composition and size.[6,34,35,43–45] As mentioned above, GM1 and GM3 are located in separate domains that have diameters <300 nm,[6,34,35] whereas sphingomyelin is enriched in plasma membrane domains with micrometer-scale dimensions.[43–45] Because micrometer-scale sphingomyelin domains are inconsistent with the expected size range for lipid rafts, these findings have been largely dismissed as artifacts caused by fluorophore-induced clustering or antibody cross-linking. Our chemical imaging method that employs nonperturbing stable isotope labels confirms that sphingolipid domains have micrometer-scale dimensions. Altogether, these findings indicate that the majority of sphingolipid domains in the plasma membrane are not lipid rafts, so the dimensions of sphingolipid domains cannot be inferred from properties ascribed to lipid rafts.

High-resolution SIMS detection of metabolically labeled sphingolipids provides direct evidence for micrometer-scale sphingolipid-enriched patches composed of numerous microdomains in the plasma membranes of fibroblast cells. These domains are organized in multiple hierarchical levels. The properties of the sphingolipid domains we observed, size and location, indicate that they are not lipid rafts. Instead, our data support a model in which protein scaffolds consisting of the cytoskeleton and its associated proteins compartmentalize the plasma membrane.[5,7,46] By adding this unique dimension of analysis—chemically specific compositional imaging at the scale of tens of nanometers—unique insight into the causes and functional consequences of plasma membrane organization is obtained.

Overall, the dependence of the sphingolipid domains on an intact cytoskeleton supports a plasma membrane model in which lipid and protein organization is actively established by

remodeling of the cortical actin.[40,42] In the fibroblasts we studied, the sphingolipid-enriched plasma membrane domains were regulated by the cytoskeleton, and cohesive cholesterol-sphingolipid interactions (not shown) were insufficient to drive the cholesterol to associate with the sphingolipid domains. Based on these findings, and the presence of a cytoskeleton in all mammalian cells, we anticipate that the plasma membranes of most types of mammalian cells contain sphingolipid domains that are not enriched with cholesterol, although the sizes of these domains may vary.

By supplementing fluorescence microscopy studies with our complementary high-resolution SIMS imaging of isotope-labeled lipids in the plasma membrane, the mechanism that links lipid organization to the cytoskeleton and the role of cholesterol in this process may be elucidated.

References

(1) This research was originally published in Proceedings of the National Academy of Sciences, USA. Frisz, J. F.; Lou, K.; Klitzing, H. A.; Hanafin, W. P.; Lizunov, V.; Wilson, R. L.; Carpenter, K. J.; Kim, R.; Hutcheon, I. D.; Zimmerberg, J.; et al. Direct Chemical Evidence for Sphingolipid Domains in the Plasma Membranes of Fibroblasts. *Proc. Natl. Acad. Sci.* **2013**, *110* (8), E613–E622.

(2) This research was originally published in *Journal of Biological Chemistry*. Frisz, J. F.; Klitzing, H. A.; Lou, K.; Hutcheon, I. D.; Weber, P. K.; Zimmerberg, J.; Kraft, M. L. Sphingolipid Domains in the Plasma Membranes of Fibroblasts Are Not Enriched with Cholesterol. *J. Biol. Chem.* **2013**, *288* (23), 16855–16861.

(3) Radhakrishnan, K.; Halasz, A.; Vlachos, D.; Edwards, J. S. Quantitative Understanding of Cell Signaling: The Importance of Membrane Organization. *Curr. Opin. Biotechnol.* **2010**, *21* (5), 677–682.

(4) Karnovsky, M. J.; Kleinfeld, A. M.; Hoover, R. L.; Klausner, R. D. The Concept of Lipid Domains in Membranes. *J. Cell Biol.* **1982**, *94* (1), 1–6.

(5) Douglass, A. D.; Vale, R. D. Single-Molecule Microscopy Reveals Plasma Membrane Microdomains Created by Protein-Protein Networks That Exclude or Trap Signaling Molecules in T Cells. *Cell* **2005**, *121* (6), 937–950.

(6) Fujita, A.; Cheng, J.; Fujimoto, T. Segregation of GM1 and GM3 Clusters in the Cell Membrane Depends on the Intact Actin Cytoskeleton. *Biochim. Biophys. Acta-Mol. Cell Biol. Lipids* **2009**, *1791* (5), 388–396.

(7) Neumann, A. K.; Itano, M. S.; Jacobson, K. Understanding Lipid Rafts and Other Related Membrane Domains. *F1000 Biol. Rep.* **2010**, *2*.

(8) Simons, K.; Gerl, M. J. Revitalizing Membrane Rafts: New Tools and Insights. *Nat. Rev. Mol. Cell Biol.* **2010**, *11* (10), 688–699.

(9) Jacobson, K.; Mouritsen, O. G.; Anderson, R. G. W. Lipid Rafts: At a Crossroad between Cell Biology and Physics. *Nat. Cell Biol.* **2007**, *9* (1), 7–14.

(10) Shaw, A. S. Lipid Rafts: Now You See Them, Now You Don't. *Nat. Immunol.* **2006**, *7* (11), 1139–1142.

(11) Leslie, M. Do Lipid Rafts Exist? *Science* **2011**, *334* (6059), 1046–1047.

(12) Hess, S. T.; Kumar, M.; Verma, A.; Farrington, J.; Kenworthy, A.; Zimmerberg, J. Quantitative Electron Microscopy and Fluorescence Spectroscopy of the Membrane Distribution of Influenza Hemagglutinin. *J. Cell Biol.* **2005**, *169* (6), 965–976.

(13) Polozov, I. V.; Bezrukov, L.; Gawrisch, K.; Zimmerberg, J. Progressive Ordering with Decreasing Temperature of the Phospholipids of Influenza Virus. *Nat. Chem. Biol.* **2008**, *4* (4), 248–255.

(14) Scheiffele, P.; Roth, M. G.; Simons, K. Interaction of Influenza Virus Haemagglutinin with Sphingolipid-Cholesterol Membrane Domains via Its Transmembrane Domain. *Embo J.* **1997**, *16* (18), 5501–5508.

(15) Hannun, Y. A.; Obeid, L. M. Principles of Bioactive Lipid Signalling: Lessons from Sphingolipids. *Nat. Rev. Mol. Cell Biol.* **2008**, *9* (2), 139–150.

(16) McMahon, G.; Glassner, B. J.; Lechene, C. P. Quantitative Imaging of Cells with Multi-Isotope Imaging Mass Spectrometry (MIMS)-Nanoautography with Stable Isotope Tracers. *Appl. Surf. Sci.* **2006**, *252* (19), 6895–6906.

(17) Boxer, S. G.; Kraft, M. L.; Weber, P. K. Advances in Imaging Secondary Ion Mass Spectrometry for Biological Samples. *Annu. Rev. Biophys.* **2009**, *38*, 53–74.

(18) Lechene, C.; Hillion, F.; McMahon, G.; Benson, D.; Kleinfeld, A. M.; Kampf, J. P.; Distel, D.; Luyten, Y.; Bonventre, J.; Hentschel, D.; et al. High-Resolution Quantitative Imaging of Mammalian and Bacterial Cells Using Stable Isotope Mass Spectrometry. *J. Biol.* **2006**, *5* (6), 1–30.

(19) Anderton, C. R.; Lou, K.; Weber, P. K.; Hutcheon, I. D.; Kraft, M. L. Correlated AFM and NanoSIMS Imaging to Probe Cholesterol-Induced Changes in Phase Behavior and Non-Ideal Mixing in Ternary Lipid Membranes. *Biochim. Biophys. Acta* **2011**, *1808* (1), 307–315.

(20) Kraft, M. L.; Weber, P. K.; Longo, M. L.; Hutcheon, I. D.; Boxer, S. G. Phase Separation of Lipid Membranes Analyzed with High-Resolution Secondary Ion Mass Spectrometry. *Science* **2006**, *313* (5795), 1948–1951.

(21) Steinhauser, M. L.; Bailey, A. P.; Senyo, S. E.; Guillermier, C.; Perlstein, T. S.; Gould, A. P.; Lee, R. T.; Lechene, C. P. Multi-Isotope Imaging Mass Spectrometry Quantifies Stem Cell Division and Metabolism. *Nature* **2012**, *481* (7382), 516–U131.

(22) Garner, P.; Park, J. M.; Malecki, E. A Stereodivergent Synthesis of D-Erythro-Sphingosine and D-Threo-Sphingosine from L-Serine. *J. Org. Chem.* **1988**, *53* (18), 4395–4398.

(23) Dondoni, A.; Perrone, D. Synthesis of 1,1-Dimethylethyl (S)-4-Formyl-2,2-Dimethyl-3-Oxazolidinecarboxylate by Oxidation of the Alcohol. In *Organic Syntheses*; John Wiley & Sons, Inc., 2003.

(24) Peters, C.; Billich, A.; Ghobrial, M.; Högenauer, K.; Ullrich, T.; Nussbaumer, P. Synthesis of Borondipyrromethene (BODIPY)-Labeled Sphingosine Derivatives by Cross-Metathesis Reaction. *J. Org. Chem.* **2007**, *72* (5), 1842–1845.

(25) Cheng, J.; Fujita, A.; Ohsaki, Y.; Suzuki, M.; Shinohara, Y.; Fujimoto, T. Quantitative Electron Microscopy Shows Uniform Incorporation of Triglycerides into Existing Lipid Droplets. *Histochem. Cell Biol.* **2009**, *132* (3), 281–291.

(26) R Development Core Team. R: A Language and Environment for Statistical Computing. R Foundation for Statistical Computing, Vienna 2010.

(27) Baddeley, A.; Turner, R. Spatstat: An R Package for Analyzing Spatial Point Patterns. *J. Stat. Softw.* **2005**, *12* (6), 1–42.

(28) Prior, I. A.; Muncke, C.; Parton, R. G.; Hancock, J. F. Direct Visualization of Ras Proteins in Spatially Distinct Cell Surface Microdomains. *J. Cell Biol.* **2003**, *160* (2), 165–170.

(29) Dixon, P. M. Ripley's K Function. In *Encyclopedia of Environmetrics*; El-Shaarawi, A. H., Piegorsch, W. W., Eds.; Wiley, Chichester, UK, 2002; pp 1796–1803.

(30) Regen, C. M.; Horwitz, A. F. Dynamics of Beta 1 Integrin-Mediated Adhesive Contacts in Motile Fibroblasts. *J. Cell Biol.* **1992**, *119* (5), 1347–1359.

(31) Chen, Y.; Qin, J.; Cai, J.; Chen, Z. W. Cold Induces Micro- and Nano-Scale Reorganization of Lipid Raft Markers at Mounds of T-Cell Membrane Fluctuations. *PLoS ONE* **2009**, *4* (4), e5386.

(32) Feigenson, G. W. Phase Boundaries and Biological Membranes. In *Annual Review of Biophysics and Biomolecular Structure*; Annual Reviews: Palo Alto, 2007; Vol. 36, pp 63–77.

(33) Spector, I.; Shochet, N. R.; Kashman, Y.; Groweiss, A. Latrunculins: Novel Marine Toxins That Disrupt Microfilament Organization in Cultured Cells. *Science* **1983**, *219* (4584), 493–495.

(34) Fujita, A.; Cheng, J.; Hirakawa, M.; Furukawa, K.; Kusunoki, S.; Fujimoto, T. Gangliosides GM1 and GM3 in the Living Cell Membrane Form Clusters Susceptible to Cholesterol Depletion and Chilling. *Mol. Biol. Cell* **2007**, *18* (6), 2112–2122.

(35) Chen, Y.; Qin, J.; Chen, Z. W. Fluorescence-Topographic NSOM Directly Visualizes Peak-Valley Polarities of GM1/GM3 Rafts in Cell Membrane Fluctuations. *J. Lipid Res.* **2008**, *49* (10), 2268–2275.

(36) Pralle, A.; Keller, P.; Florin, E.-L.; Simons, K.; Hörber, J. K. H. Sphingolipid–Cholesterol Rafts Diffuse as Small Entities in the Plasma Membrane of Mammalian Cells. *J. Cell Biol.* **2000**, *148* (5), 997–1008.

(37) Lasserre, R.; Guo, X.-J.; Conchonaud, F.; Hamon, Y.; Hawchar, O.; Bernard, A.-M.; Soudja, S. M.; Lenne, P.-F.; Rigneault, H.; Olive, D.; et al. Raft Nanodomains Contribute

to Akt/PKB Plasma Membrane Recruitment and Activation. *Nat. Chem. Biol.* **2008**, *4* (9), 538–547.

(38) Eggeling, C.; Ringemann, C.; Medda, R.; Schwarzmann, G.; Sandhoff, K.; Polyakova, S.; Belov, V. N.; Hein, B.; von Middendorff, C.; Schoenle, A.; et al. Direct Observation of the Nanoscale Dynamics of Membrane Lipids in a Living Cell. *Nature* **2009**, *457* (7233), 1159–U121.

(39) Kwik, J.; Boyle, S.; Fooksman, D.; Margolis, L.; Sheetz, M. P.; Edidin, M. Membrane Cholesterol, Lateral Mobility, and the Phosphatidylinositol 4,5-Bisphosphate-Dependent Organization of Cell Actin. *Proc. Natl. Acad. Sci.* **2003**, *100* (24), 13964–13969.

(40) Goswami, D.; Gowrishankar, K.; Bilgrami, S.; Ghosh, S.; Raghupathy, R.; Chadda, R.; Vishwakarma, R.; Rao, M.; Mayor, S. Nanoclusters of GPI-Anchored Proteins Are Formed by Cortical Actin-Driven Activity. *Cell* **2008**, *135* (6), 1085–1097.

(41) Mueller, V.; Ringemann, C.; Honigmann, A.; Schwarzmann, G.; Medda, R.; Leutenegger, M.; Polyakova, S.; Belov, V. N.; Hell, S. W.; Eggeling, C. STED Nanoscopy Reveals Molecular Details of Cholesterol- and Cytoskeleton-Modulated Lipid Interactions in Living Cells. *Biophys. J.* **2011**, *101* (7), 1651–1660.

(42) Gowrishankar, K.; Ghosh, S.; Saha, S.; Rumamol, C.; Mayor, S.; Rao, M. Active Remodeling of Cortical Actin Regulates Spatiotemporal Organization of Cell Surface Molecules. *Cell* **2012**, *149* (6), 1353–1367.

(43) Tyteca, D.; D'Auria, L.; Van Der Smissen, P.; Medts, T.; Carpentier, S.; Monbaliu, J. C.; de Diesbach, P.; Courtoy, P. J. Three Unrelated Sphingomyelin Analogs Spontaneously Cluster into Plasma Membrane Micrometric Domains. *Biochim. Biophys. Acta-Biomembr.* **2010**, *1798* (5), 909–927.

(44) Fujimoto, T. GPI-Anchored Proteins, Glycosphingolipids, and Sphingomyelin Are Sequestered to Caveolae Only after Crosslinking. *J. Histochem. Cytochem.* **1996**, *44* (8), 929–941.

(45) Marks, D. L.; Bittman, R.; Pagano, R. E. Use of Bodipy-Labeled Sphingolipid and Cholesterol Analogs to Examine Membrane Microdomains in Cells. *Histochem. Cell Biol.* **2008**, *130* (5), 819–832.

(46) Kusumi, A.; Nakada, C.; Ritchie, K.; Murase, K.; Suzuki, K.; Murakoshi, H.; Kasai, R. S.; Kondo, J.; Fujiwara, T. Paradigm Shift of the Plasma Membrane Concept from the Two-Dimensional Continuum Fluid to the Partitioned Fluid: High-Speed Single-Molecule Tracking of Membrane Molecules. In *Annual Review of Biophysics and Biomolecular Structure*; Annual Reviews: Palo Alto, 2005; Vol. 34, pp 351–U54.

Figures and Tables

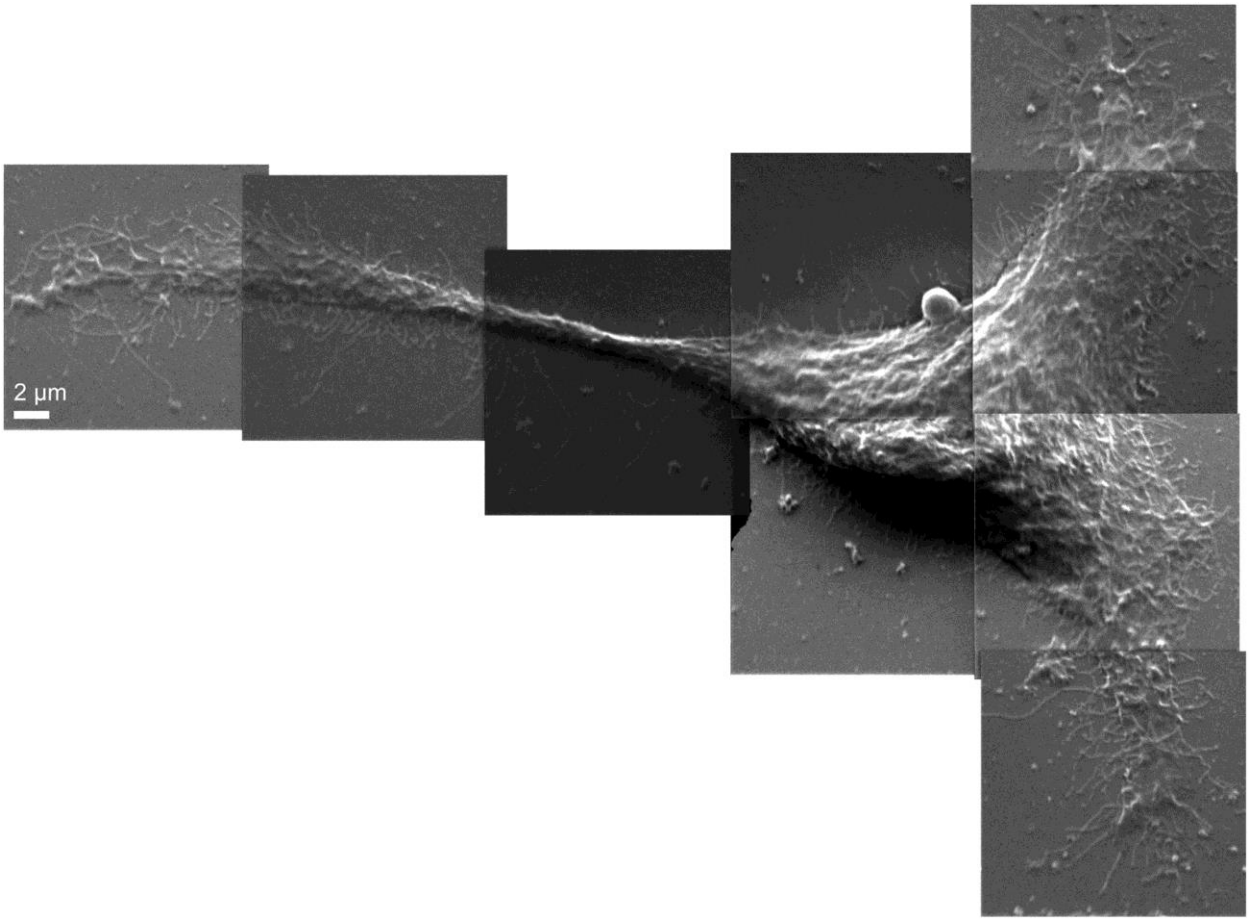

Figure 3.1 Secondary electron images of a Clone 15 fibroblast cell were acquired in parallel with the secondary ion signals, using NanoSIMS. Montage of 15 × 15-µm secondary electron images shows the morphology of a representative Clone 15 cell.

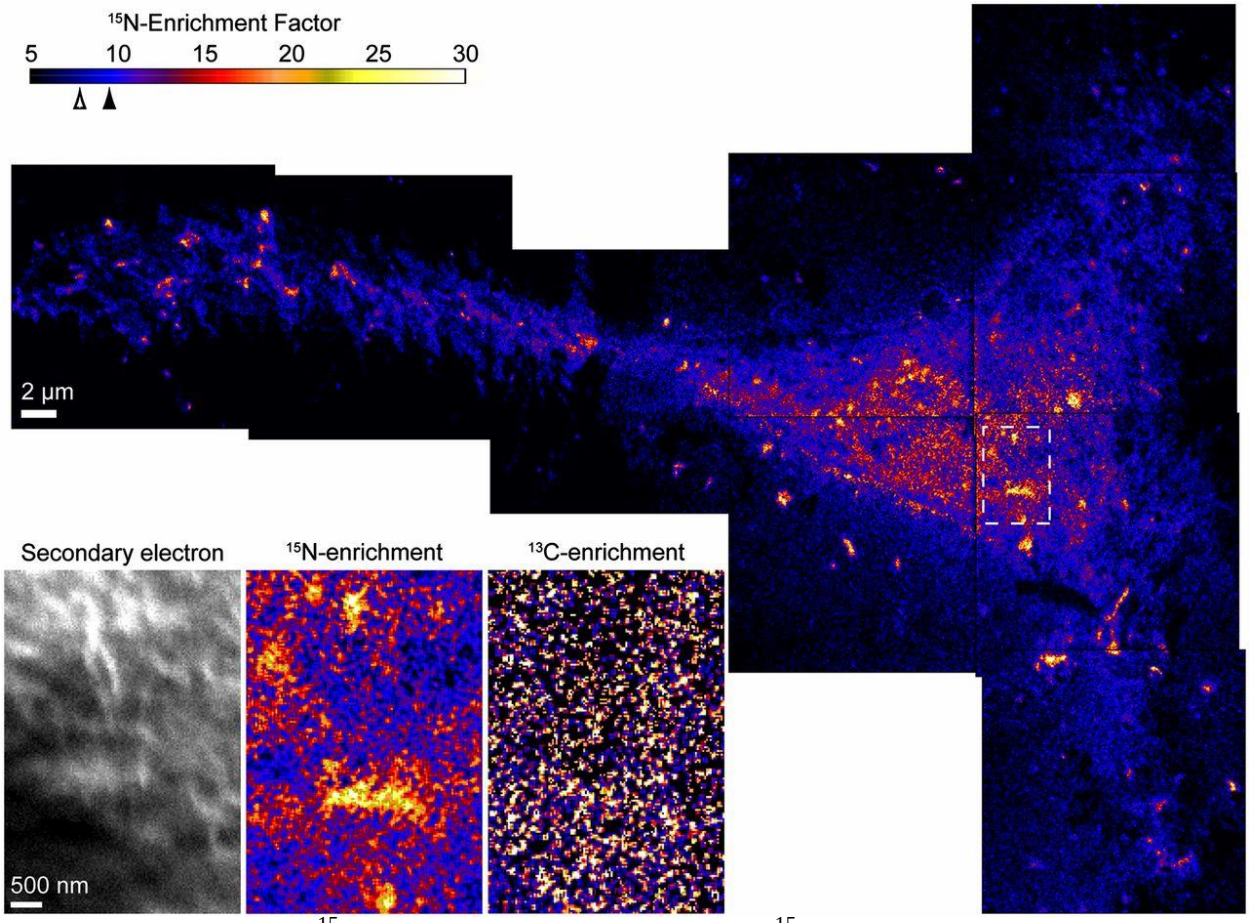

Figure 3.2 Montage of ^{15}N-enrichment images shows the ^{15}N-sphingolipid distribution on the Clone 15 fibroblast cell. The color scale represents the measured $^{12}C^{15}N^{-}/^{12}C^{14}N^{-}$ ratio divided by the natural abundance ratio, corresponding to the ^{15}N-sphingolipid enrichment. The mean ^{15}N-enrichment factors for domain-free regions and the entire cell are 7.8 (open arrowhead, SD = 2.1) and 9.5 (solid arrowhead, SD = 3.6), respectively. Lateral variations in the ^{15}N-sphingolipid abundance are visible. Consistent with reports that fibroblasts deposit membrane fragments when migrating, ^{15}N-sphingolipid–enriched debris is present on the substrate.{Regen, 1992 #922} The enlarged views of the secondary electron, ^{13}C-enrichment, and ^{15}N-enrichment images that were acquired at the outlined region on the cell (*Inset*) demonstrate that the ^{15}N-sphingolipid domains do not coincide with cell topography or excess cellular lipids. The color scale for the ^{13}C-enrichment image shown in the *Inset* is provided in Figure 3.3.

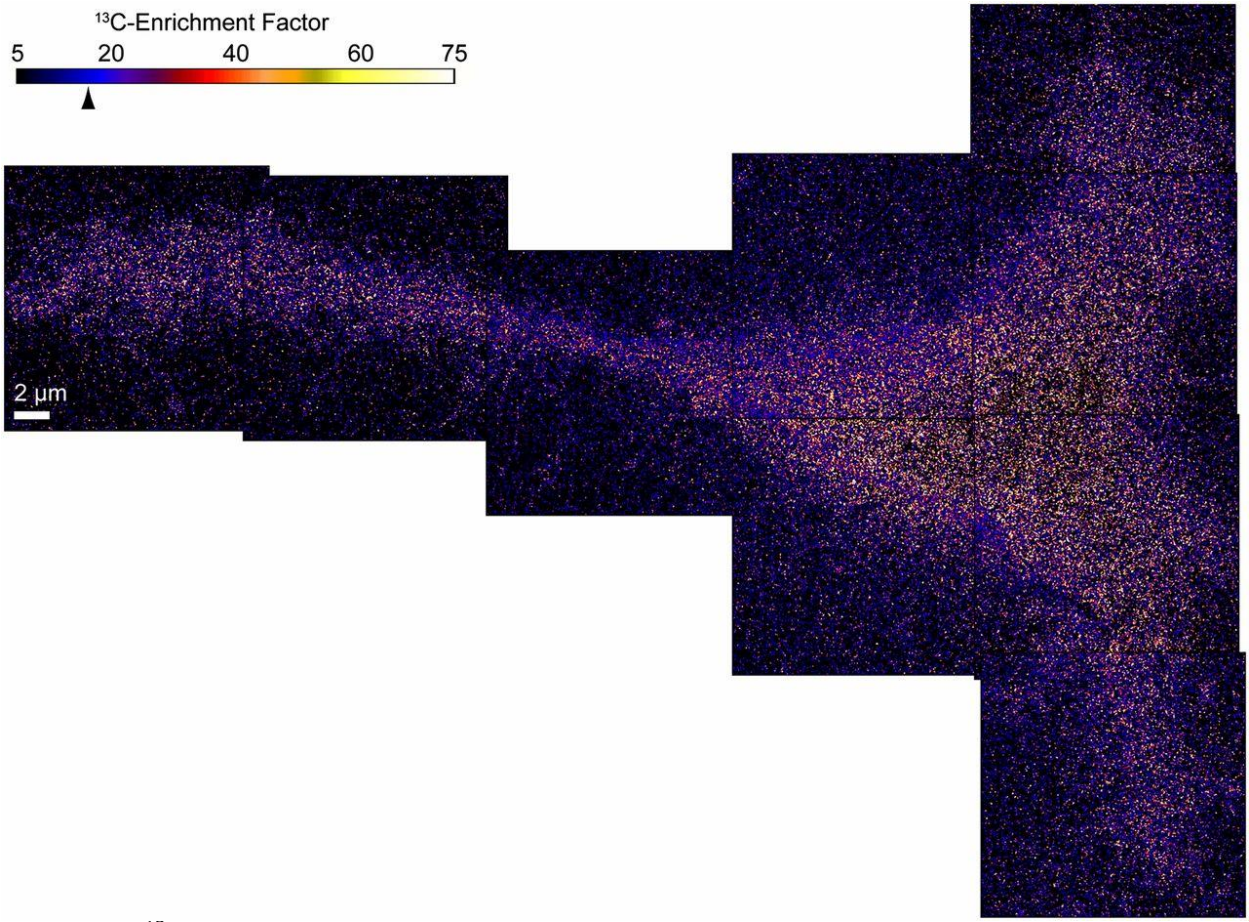

Figure 3.3 ^{13}C-enrichment images of a Clone 15 fibroblast cell were acquired in parallel with the secondary electron (Fig. 3.1) and ^{15}N-enrichment (Fig. 3.2) images. Montage of quantitative ^{13}C-enrichment images reveals the distribution of all lipids in the plasma membrane of the Clone 15 cell. The color scale shows the measured $^{13}C^{1}H^{-}/^{12}C^{1}H^{-}$ ratio divided by the natural abundance ratio, corresponding to the ^{13}C-lipid enrichment. The mean ^{13}C-enrichment for the entire surface of the cell was 16.3 (arrowhead, SD = 22.5). The elevated ^{13}C-enrichment and the absence of statistically significant lateral variations in the ^{13}C-enrichment on the cell verify the plasma membrane was intact. Speckling is due to low counts of the CH isotopologues.

	Cell 1 RT	Cell 2 RT	Cell 3 RT	Cell 1 37 °C	Cell 2 37 °C	Cell 3 37 °C	Cell 1 mβCD	Cell 2 mβCD	Cell 3 mβCD
Cell surface area, μm^2	718	518	513	1,430	668	357	348	214	237
No. domains	2,190	2,729	1,236	2,352	2,508	1,479	158	342	309
Mean domain area, μm^2	0.033 ± 0.023	0.029 ± 0.026	0.038 ± 0.032	0.033 ± 0.027	0.025 ± 0.020	0.031 ± 0.023	0.025 ± 0.019	0.027 ± 0.019	0.031 ± 0.024
Mean effective domain diameter, nm	194 ± 63	182 ± 67	205 ± 80	194 ± 72	170 ± 58	189 ± 64	170 ± 57	177 ± 59	188 ± 66
Cell surface coverage, %	10	15	9	8	10	13	1	4	4
Domains/μm^2 body	5.8	6.4	3.2	2.7	4.9	5.1	0.9	1.8	1.8
Domains/μm^2 extensions	0.9	1.3	1.1	1.3	0.7	1.4	0.2	0.8	0.5

RT, room temperature.

Table 3.1 Characteristics of cell membrane area and sphingolipid domains in Clone 15 cells

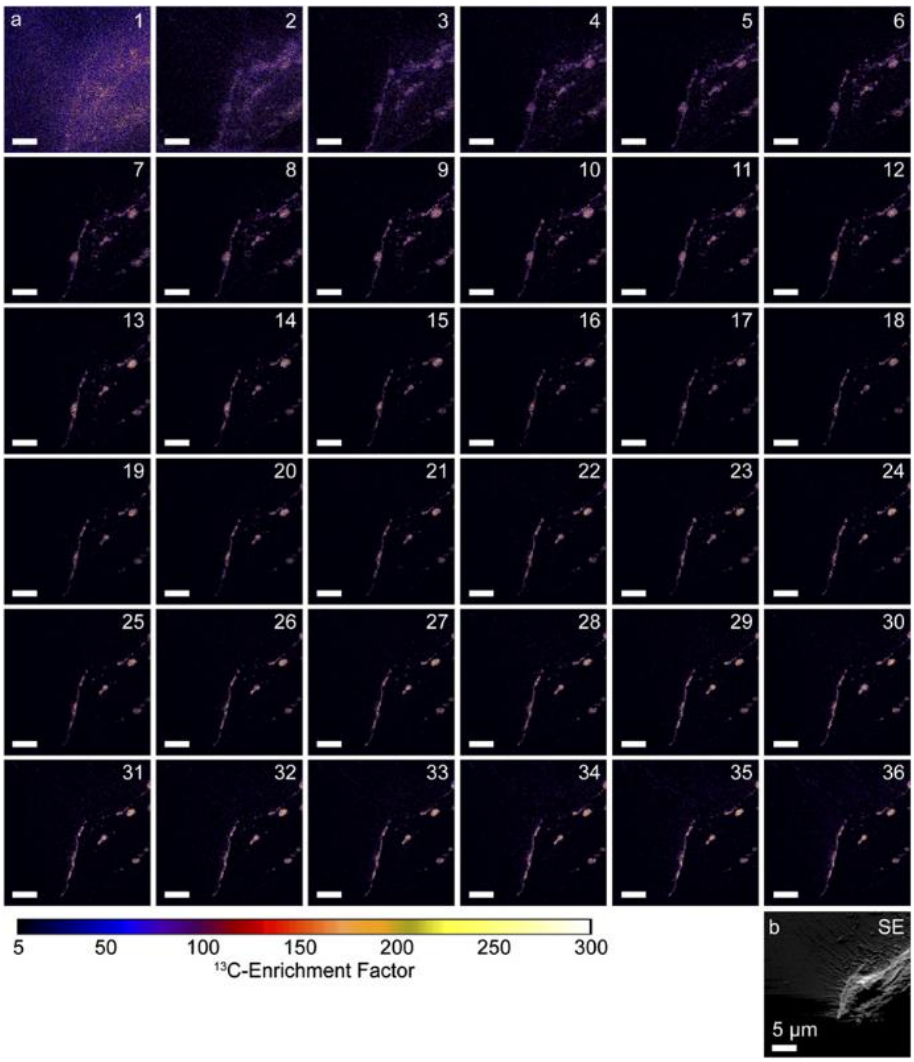

Figure 3.4. Three-dimensional distribution of ^{13}C-enrichment in the cell shows elevated ^{13}C-enrichment is specific to cellular membranes. (A) A series of 36 NanoSIMS ^{13}C-enrichment images were sequentially acquired at the same sample position on a representative Clone 15 cell that was metabolically labeled and prepared for analysis identically to the cells shown above. To permit analysis of the cytoplasm, the NanoSIMS operating conditions used to acquire these images were adjusted so that the sampling depth was approximately four times greater than that used to acquire the rest of the NanoSIMS images presented herein. Approximately 1.3 nm of material was sputtered from the sample surface each time an image was acquired. The elevated ^{13}C-enrichment was continuous at the cell surface, but became discontinuous upon the detection of significant amounts of material within the cytoplasm. Once most of the plasma membrane had been removed (approximately image 6), the ^{13}C-enrichment was elevated only at localized regions within the cytoplasm that likely correspond to organelle membranes and lipid-containing organelles. This confirms that elevated ^{13}C-enrichment is characteristic of cellular membranes. In addition, inspection of the ^{13}C-lipid structures in the cytoplasm shows that their edges remain sharp as the analysis depth increases, which demonstrates that NanoSIMS analysis did not induce biomolecule mixing or alter the lateral distribution of lipids in the sample. Similar results were obtained by depth-profiling measurements made on the four other cells we analyzed. (B) The morphology of the cell is shown in the NanoSIMS secondary electron (SE) image of this location. SEs were not detected at the lower portion of the image, likely because secondary electron production is low when the low primary ion beam currents are used for imaging.

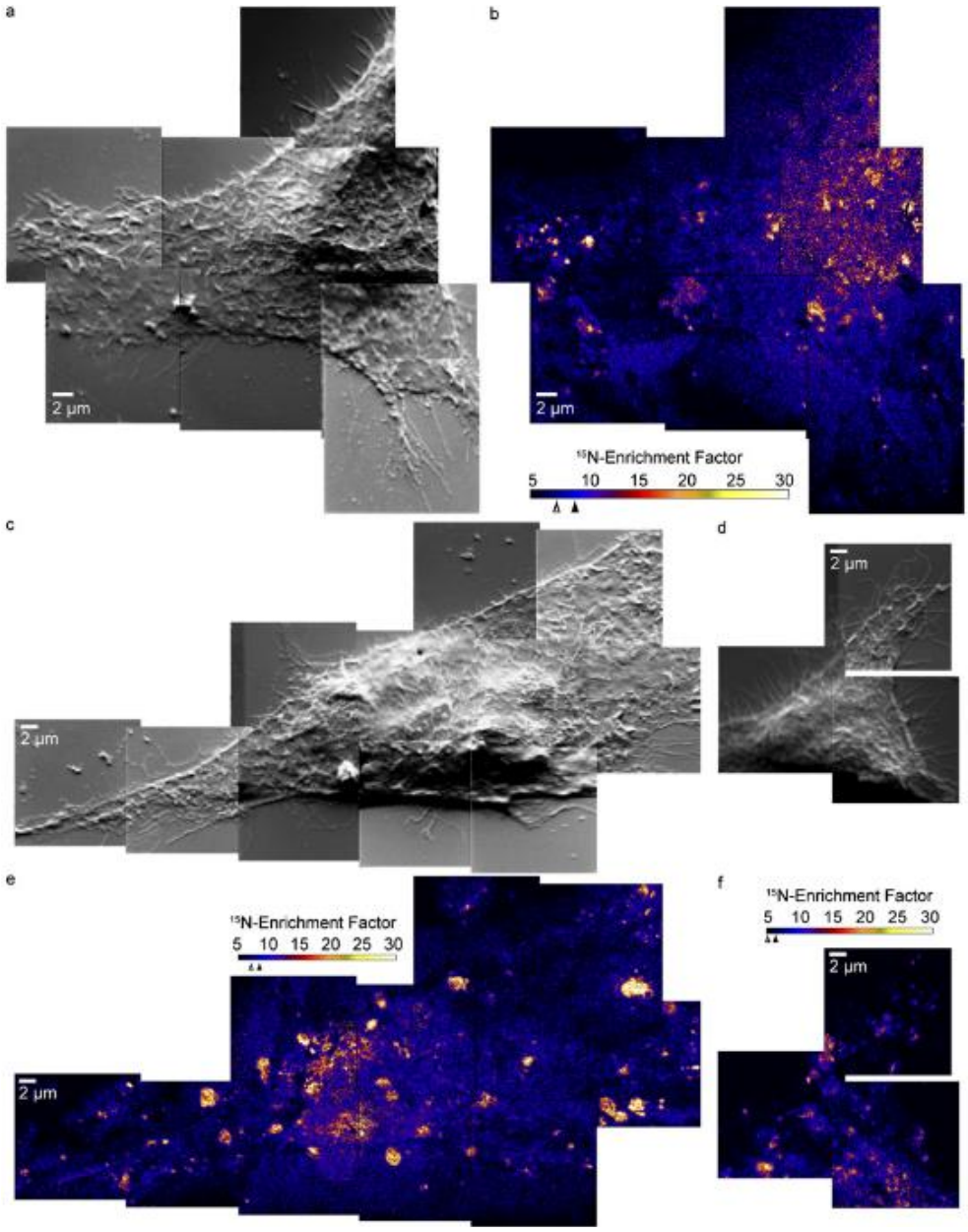

Figure 3.5 NanoSIMS images of three additional Clone 15 cells that were fixed with glutaraldehyde at 37 °C. The montages of secondary electron images show Clone 15 cell 1 at 37°C (A), cell 2 at 37 °C (C), and cell 3 at 37 °C (D) have normal morphology. The ^{15}N-enrichment images show the ^{15}N-sphingolipid abundance in the membranes of Clone 15 cell 1 at 37 °C (B), cell 2 at 37 °C (E), and cell 3 at 37 °C (F). Color scale is the $^{12}C^{15}N^{-}/^{12}C^{14}N^{-}$ratio divided by the natural abundance ratio. For cell 1 at 37 °C, the mean ^{15}N-enrichment factors for the entire surface and the domain-free regions on the cell are 9.2 (solid arrowhead, SD = 4.8) and 7.4 (open arrowhead, SD= 2.8), respectively. For cell 2 at 37 °C, the mean15 N-enrichment factors for the entire surface (solid arrowhead) and domain-free areas (open arrowhead) are 8.5 (SD = 4.6) and 5.1 (SD = 1.9), respectively. For cell 3 at 37 °C, the mean 15 N-enrichment factors for the entire surface (solid arrowhead) and domain-free areas (open arrowhead) are 6.3 (SD = 3.4) and 5.6 (SD = 2.4), respectively.

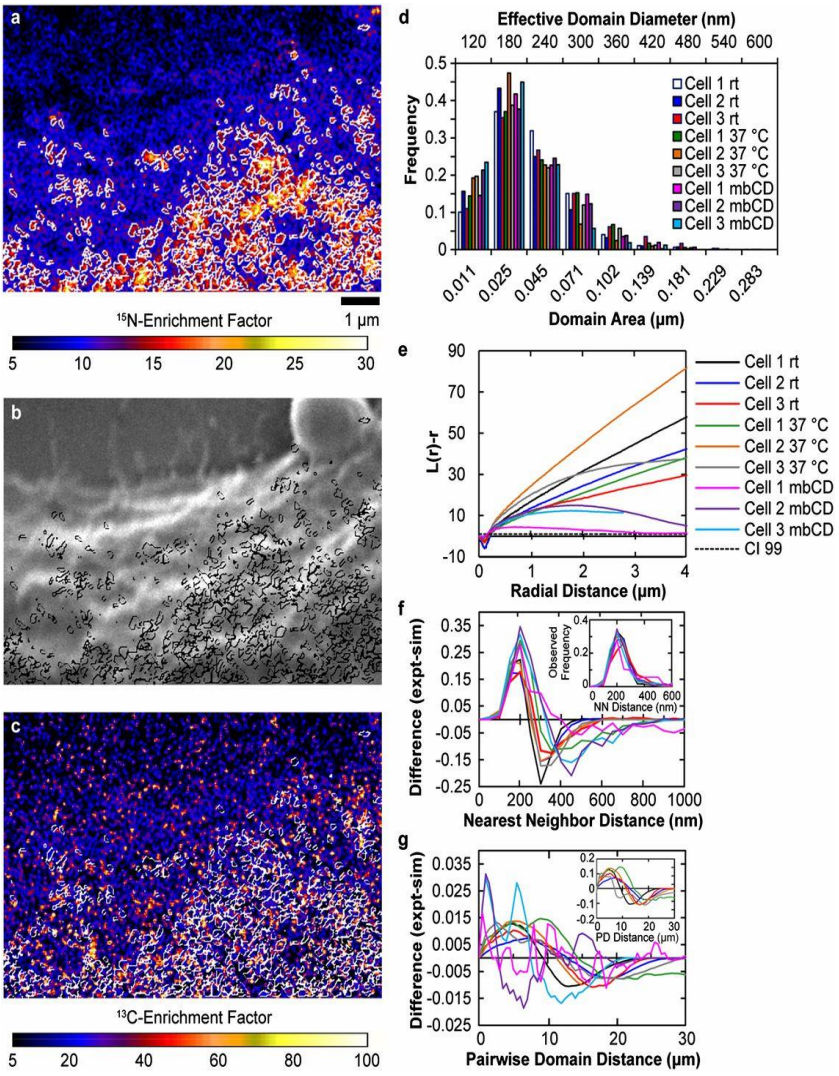

Figure 3.6 Sphingolipid-enriched domain size and spatial distribution. (*A*) White outlines show the perimeters of the ^{15}N-sphingolipid domains (defined with a particle definition algorithm) in a portion of the ^{15}N-enrichment image shown in Fig. 3.2. (*B* and *C*) The locations of the ^{15}N-sphingolipid domains are outlined on the corresponding (*B*) secondary electron image (black) and (*C*) ^{13}C-enrichment image (white). (*D*) The frequency distributions of sphingolipid domain sizes measured on cells fixed with glutaraldehyde solution at either RT or 37 °C or treated with mβCD show these treatments did not affect microdomain size. (*E*) Plot of Ripley's K-test statistic, L(r) – r, as a function of distance. Data are normalized so the 99% CI (CI 99, dashed line) = 1. L(r) – r exceeds the CI 99 for all accessible distances >0.2 μm regardless of fixation temperature, signifying nonrandom microdomain clustering. mβCD treatment decreased domain clustering at distances >2 μm. (*F*) Plot of the difference between the frequency distribution of nearest neighbor (NN) domain distances measured for the observed (expt) domains (*Inset*) and a simulated (sim) random domain distribution on the cell body vs. distance. For all treatments, NN distances of ∼200 nm occurred more often than expected for a random distribution. (*G*) Difference in the pairwise domain distances (PD) measured for the observed and simulated randomly distributed domains is plotted as a function of distance. For both fixation temperatures, the higher occurrence of domain–domain distances between 5 and 10 μm than expected for randomly distributed domains (*Inset*) indicates the microdomain clusters were more abundant within 5- to 10-μm diameter patches on the cell body. Treatment with mβCD disrupted this long-range microdomain organization.

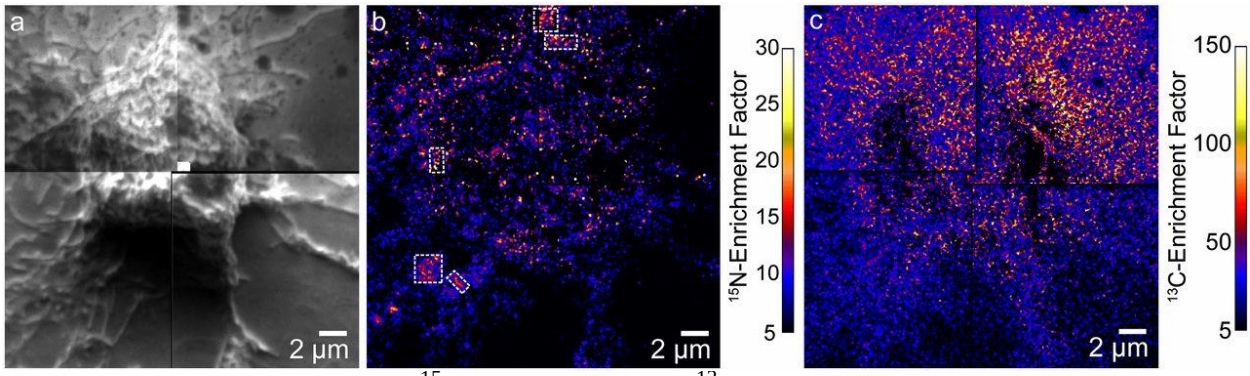

Figure 3.7 Secondary electron, ^{15}N-enrichment, and ^{13}C-enrichment images of a Clone 15 cell that was treated with latrunculin A for 30 min to disrupt the cytoskeleton. (*A*) Montage of secondary electron images acquired with NanoSIMS shows the extensive cell rounding that is characteristic of cytoskeleton disruption by latrunculin A treatment. (*B*) Montage of ^{15}N-enrichment images of the same cell shows that micrometer-scale sphingolipid domains were not present on the cell surface after disruption of the cytoskeleton by treatment with latrunculin A. A few micrometer-scale ^{15}N-sphingolipid aggregates are present on the cellular extensions adjacent to the rounded cell body (outlined with a dashed white line). (*C*) Montage of ^{13}C-enrichment images shows the ^{13}C-lipid distribution at the same location. The high ^{13}C-enrichment on the substrate adjacent to the cell likely signifies the presence of membrane fragments.

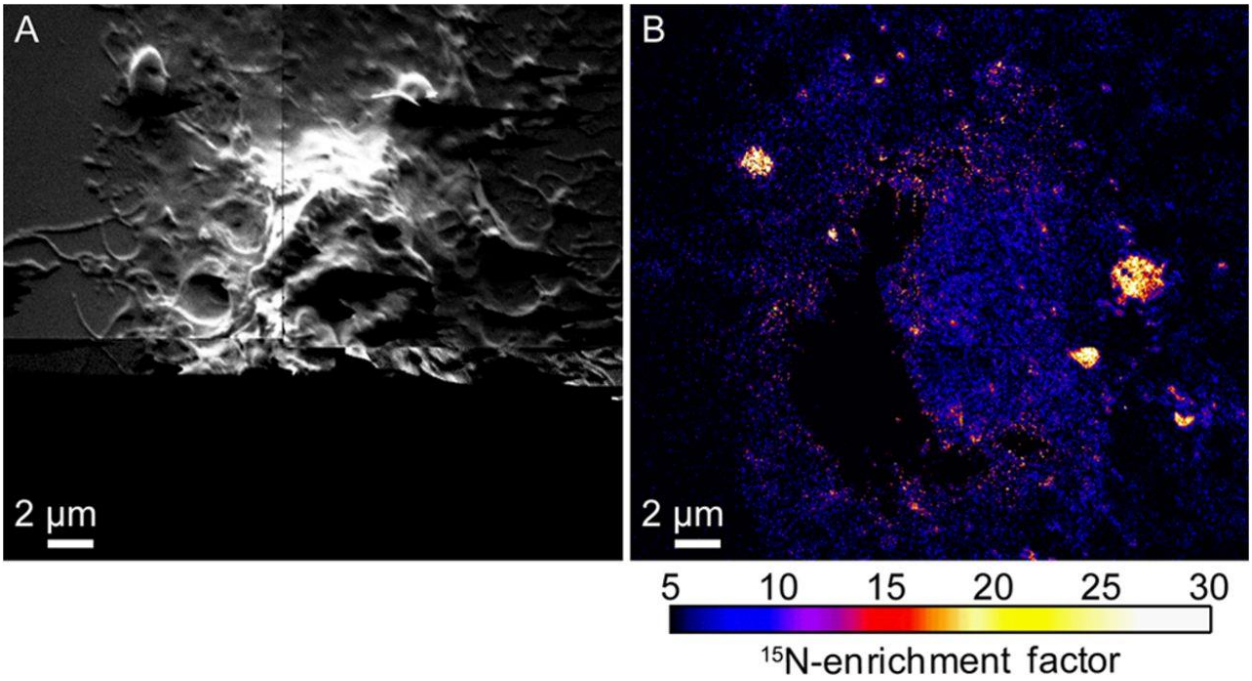

Figure 3.8 High-resolution SIMS images of a NIH 3T3 cell treated with latrunculin A to disrupt its cytoskeleton. (A) montage of secondary electron images acquired with high-resolution SIMS shows latrunculin A treatment disrupted the cytoskeleton of the metabolically labeled NIH 3T3 cell. Secondary electrons were not detected near the *bottom* of the image due to the low primary ion beam current used for analysis. (B) montage of ^{15}N-enrichment SIMS images shows few ^{15}N-sphingolipid domains were present in the plasma membrane of the NIH 3T3 cell after latrunculin A treatment. Latrunculin A treatment also disrupts the sphingolipid domains in the plasma membranes of clone 15 cells.

CHAPTER 4.
CHANGES IN SPHINGOLIPID MICRODOMAINS AS A FUNCTION OF TIME

Notes and Acknowledgements

This chapter describes unpublished work. Mary L. Kraft planned experiments, assisted with NanoSIMS analysis, developed statistical tools for data analysis, and assisted with data interpretation. Haley A. Klitzing planned and performed experiments, performed NanoSIMS analysis, data analysis, and data interpretation. Peter K. Weber assisted with NanoSIMS analysis. We thank A. Ulanov for his valuable comments on the evaluation of isotope incorporation, J. Zimmerberg for the Clone 15 cell line, C. Ramon for technical assistance, and L. Nittler for software development. MLK holds a Career Award at the Scientific Interface from the Burroughs Wellcome Fund. Portions of this work were carried out in the Metabolomics Center in the Roy J. Carver Biotechnology Center, Univ. of Illinois, and in the Frederick Seitz Materials Research Laboratory Central Facilities, Univ. of Illinois, which are partially supported by the U.S. Department of Energy (DOE) under grants DE-FG02-07ER46453 and DE-FG02-07ER46471. Work at Lawrence Livermore National Laboratory was supported by Laboratory Directed Research and Development funding and performed under the auspices of the U.S. DOE under contract DE-AC52-07NA27344. This material was supported in part by the National Science Foundation under CHE—1058809.

Introduction

Being the outermost structure of mammalian cells, the plasma membrane is involved in many key cellular functions.[1–4] Because of the membrane's importance in multiple cellular processes, many studies have focused on elucidating plasma membrane organization and how this organization changes in response to internal and external stimuli, such as protein signaling, cholesterol depletion, and mutations in integral membrane proteins.[5–9] Despite being intensely researched, the organization of most lipid species within the plasma membrane, sphingolipids being of particular interest, has been difficult to determine.[10]

As was described in the previous chapters, we have used high-resolution imaging secondary ion mass spectrometry (SIMS) to image metabolically incorporated ^{15}N-sphingolipids in the plasma membranes of mouse fibroblast cells that stably expressed influenza hemagglutinin (Clone 15 cell line).[11] In these experiments, the cells were first metabolically labeled for 6 days so that the resulting ^{15}N-sphingolipids reached a steady-state intracellular distribution. High-resolution SIMS mapping of the sphingolipid-specific ^{15}N-enrichment on the cell surface (top ~5 nm) revealed micrometer-scale ^{15}N-sphingolipid patches consisting of many sphingolipid microdomains (~200 nm in diameter) that were detectable in the plasma membrane.[11] The sizes of these domains, and their higher dependency on the cytoskeleton than on cholesterol abundance, indicated the sphingolipids were confined within domains by the cytoskeleton and its associated proteins.[11] The relatively even cholesterol distribution (not shown in this dissertation) subsequently observed in the plasma membranes of Clone 15 cells and analogous mouse fibroblast cells (NIH-3T3, the parent line from which Clone 15 was derived) confirmed that the sphingolipid domains did not result from favorable cholesterol-sphingolipid interactions.[12] Instead, these results are consistent with the hypothesis that cortical actin and its associated

proteins establish diffusion barriers that sustain concentration gradients produced by vesicle transport.[13] In this hypothesis, cortical actin and its associated proteins establish diffusion barriers that sustain local concentration gradients produced by vesicle fusion.[13] Consequently, the local elevations in sphingolipid abundance that we have observed within the plasma membrane may result from the fusion of the transport vesicles that move newly synthesized sphingolipids from the Golgi apparatus to the plasma membrane.

In this chapter, we investigate how newly biosynthesized sphingolipids are organized in the plasma membrane. We pulse labeled the cells with ^{15}N-sphingoid bases for time intervals that ranged from 30 min to 6 d and imaged the distributions of the ^{15}N-sphingolipids that were synthesized from these labeled ^{15}N-sphingoid bases in the plasma membrane with high-resolution SIMS. We found that the newly synthesized ^{15}N-sphingolipids were rapidly incorporated into discrete domains within the plasma membrane. The fraction of the plasma membrane that was occupied by domains that are enriched with ^{15}N-sphingolipids was fairly constant for all pulse labeling times employed, though the ^{15}N-enrichment, and thus the amount of ^{15}N-sphingolipids, within these domains increased with the pulse labeling time. The short range (<1 μm) sphingolipid microdomain organization did not change as the pulse labeling time increased. The long range (>2 μm) sphingolipid microdomain organization slightly increased as the pulse labeling time increased to 8 h, and no further changes were observed at longer labeling times. These results indicate that the ^{15}N-sphingolipids synthesized from the ^{15}N-sphingoid bases were rapidly incorporated into plasma membrane domains with sphingolipids that contained the unlabeled (abundant nitrogen-14 isotope) sphingoid backbone. These findings suggest that the sphingolipids in the plasma membrane are rapidly internalized, are sorted to the

Golgi or endosomes where they mix with newly synthesized sphingolipids before returning to the plasma membrane.

Methods

Materials

The Clone 15 cell line, transfected from the NIH-3T3 mouse fibroblast line to stably express the influenza protein hemagglutinin, was obtained from the NIH (Zimmerberg). Initial cell growth medium (Media A) consisted of high glucose Dulbecco's modified Eagle's medium (DMEM) supplemented with 10% Hyclone calf serum (Fisher Scientific), 10^4 U/mL penicillin G, and 10 mg/mL streptomycin. During the second stage of cell growth, the medium (Media B) consisted of high glucose DMEM supplemented with 10% Hyclone lipid-reduced fetal bovine serum and 1% Hyclone calf serum (Fisher Scientific). A fatty acid solution (^{13}C-fatty acids) made from algal lipid mixture (uniformly carbon-13 labeled, UL-^{13}C, 98%+) (Cambridge Isotope Laboratories, Inc.), stearic acid ($^{13}C_{18}$, 99 atom% ^{13}C) (Isotec), and fatty acid free bovine serum albumin (FAF-BSA) was used to metabolically label all cellular lipids. The ^{15}N-sphingoid bases, 1:1 molar ratio of ^{15}N-sphingosine and ^{15}N-sphinganine, used to isotopically label sphingolipids consist were synthesized from ^{15}N-serine following reported techniques.[14–16] Natural abundance (NA-) sphingoid bases were synthesized in the same manner using regular serine. Silicon substrates (5 x 5 mm) were purchased from Ted Pella, Inc. Separation and mass spectrometry (MS) was performed using an Agilent 1100 LC/MSD Trap XCT Plus equipped with a Phenomenex Gemini 3u C6-Phenyl 110A column (2 x 100 mm) (LC-MS) and an Agilent 6890 gas chromatograph with a ZB-WAX (30 m × 0.25 mm I.D., 0.25 μm film thickness) capillary column (Phenomenex, Torrance, CA, USA), an Agilent 5973 mass selective detector and HP 7683B (Agilent Inc, Palo Alto, CA, USA) autosampler (GC-MS).

Metabolic Labeling

Cells were grown in Media A at 37°C in 5% CO_2 during which culture media was supplemented with 3 µM NA-sphingoid bases on a daily basis. After 3 nights, the cells were passaged, plated onto new culture dishes, and grown in Media B at 37°C in 5% CO_2. On a daily basis, Media B was supplemented with 3 µM NA-sphingoid bases and 227 µM ^{13}C-fatty acids (4:1:28 mass ratio of UL-^{13}C lipid mix/^{13}C-stearic acid/FAF-BSA). On the sixth day, cells were passaged and reset into dishes containing fresh Media B, NA-sphingoid bases and ^{13}C-fatty acid supplements, and sterilized, poly-L-lysine coated silicon substrates. The following day, culture media was removed and replaced with fresh Media B. The fresh media was then supplemented with 227 µM ^{13}C-fatty acids and 6 µM ^{15}N-sphingoid bases. After pre-determined time intervals, substrates with attached cells were collected and chemically fixed. The remaining cells attached to the culture dishes were harvested and further used for label incorporation evaluation.

^{15}N-Incorporation Analysis

The harvested cells underwent lipid extraction.[17,18] LC-MS was performed and ion peaks corresponding to N-palmitoyl sphingomyelin, including m/*z* 703.6 (unlabeled N-palmitoyl sphingomyelin), 704.6 (^{15}N-palmitoyl sphingomyelin), 719.6 (^{14}N-palmitoyl $^{13}C_{16}$-sphingomyelin), 720.6 (^{15}N-palmitoyl $^{13}C_{16}$-sphingomyelin), and 735.7 (^{14}N-palmitoyl $^{13}C_{32}$-sphingomyelin), were analyzed to determine the percent incorporation of nitrogen-15 into sphingolipid molecules. The contribution from other isotopologues was removed, and the fraction of N-palmitoyl sphingomyelin that contained the nitrogen-15 isotope was calculated as the ratio of ^{15}N-palmitoyl sphingomyelin and ^{15}N-palmitoyl $^{13}C_{16}$-sphingomyelin peak intensities to the sum of the peak intensities from all N-palmitoyl sphingomyelin isotopologues. The fraction of N-palmitoyl sphingomyelin that biosynthesized from uniformly labeled ^{13}C-palmitic

acid was also calculated as the ratio of the sum of ^{14}N-palmitoyl $^{13}C_{16}$-sphingomyelin, ^{15}N-palmitoyl $^{13}C_{16}$-sphingomyelin, and ^{14}N-palmitoyl $^{13}C_{32}$-sphingomyelin over the sum of all of the peaks.

^{13}C-Incorporation Analysis

The lipid extracts were hydrolyzed, neutralized, and methylated. GC-MS was then performed on the resulting fatty acid methyl esters (FAMEs). The signal intensities corresponding to $^{13}C_{16}$-palmitic acid (*m*/*z* 286), $^{12}C_{16}$-palmitic acid (*m*/*z* 270), $^{13}C_{16}$-palmitoleic acid (*m*/*z* 284), $^{12}C_{16}$- palmitoleic acid (*m*/*z* 268), $^{13}C_{18}$-stearic acid (*m*/*z* 316), $^{12}C_{18}$-stearic acid (*m*/*z* 298), $^{13}C_{18}$-oleic acid (*m*/*z* 314), $^{12}C_{18}$-oleic acid (*m*/*z* 296), $^{13}C_{18}$-linoleic acid (*m*/*z* 312), and $^{12}C_{18}$-linoleic acid (*m*/*z* 294) were then used to determine a representative incorporation value.

Cell Preservation

Silicon chips were removed from culture dishes and rinsed with Hendry's Phosphate Buffer (HPB). Cells were fixed in 4% glutaraldehyde (diluted in HPB) for 30 min at room temperature. Substrates were then rinsed twice in HPB for 5 min followed by one rinse in 18mΩ filtered water. Heavy metal staining was then performed using 1% osmium tetroxide solution for 15 min. Samples were then rinsed three times for 5 min each in 18mΩ filtered water and allowed to air dry.

Pre-Characterization of Cells

An optical map showing the locations of cells in relation to one another, the scratches on the chip, and the edges of the chip was created using bright field microscopy. Secondary electron microscopy (SEM) was performed on a Hitachi S4800 SEM instrument. Since the samples did not receive a sputter coating, SEM was performed using low voltage in order to avoid sample charging and to prevent damage to the sample.

High-Resolution Secondary Ion Mass Spectrometry (SIMS)

High-resolution SIMS was performed on a Cameca NanoSIMS 50 (Cameca, France) at Lawrence Livermore National Laboratory similarly to how was previously reported. To increase signal and prevent charging, samples were sputter coated with 3 nm of iridium. A ~0.15 pA $^{133}Cs^+$ primary ion beam was used for an analysis that included four replicate scans of 512 x 512 pixels, with a dwell time of 1000 µs/pixel, over a 15 x 15 μm^2 analysis region, resulting in a pixel size of 29 x 29 nm^2. The $^{12}C^{12}C^-$, $^{13}C^{12}C^-$, $^{12}C^{14}N^-$, and $^{12}C^{15}N^-$ secondary ions, and secondary electrons were simultaneously collected.

Image Processing

Image analysis was performed using a custom software package (L'image, L.R. Nittler, Carnegie Institution of Washington) run on a PV-Wave platform (Rogue Wave Software). The distribution of each labeled cell component was determined according to the isotopic enrichment for that species, which is the ratio of secondary ion signal intensities of the rare isotope to its corresponding naturally abundant isotope, $^{13}C^{12}C^-/^{12}C^{12}C^-$ correlating to all ^{13}C-cellular lipids while $^{15}N^{12}C^-/^{14}N^{12}C^-$ corresponds to ^{15}N-sphingolipids, divided by the natural abundance ratio (0.00367 and 0.011237 respectively). This resulted in the number of times that the enrichment is great than that in an unlabeled cell.

Quantitative Analysis of ^{15}N-enriched Sphingolipid Domains

For each cell, the threshold ^{15}N-enrichment that is statistically significant and cannot be attributed to noise was identified using the MATLAB Statistics Toolbox™, as previously reported (1). The regions of statistically significant ^{15}N-enrichment that represent ^{15}N-sphingolipid domains on each cell were defined with a particle definition algorithm within a custom software package (Limage; L. R. Nittler, Carnegie Institution of Washington,

Washington, DC) run on the PV-Wave platform (Rogue Wave), as described previously.[11] The spatial arrangements of the ^{15}N-sphingolipid domains on each cell were evaluated using the SpatStat spatial statistics package run in the R program as previously reported.[11,19]

Results

Incorporation of ^{15}N-Sphingolipids into Cells after Various Pulse Labeling Times

We investigated Clone 15 cells that had been pulse-labeled with the ^{15}N-sphingolipid precursors, ^{15}N-sphingosine and ^{15}N-sphinganine, for times varying from 30 min to 24 h. These intervals are much shorter than the 6 d labeling time that we previously used to produce a steady-state ^{15}N-sphingolipid distribution in the plasma membrane.[11] Cells that had been cultured in the presence of ^{15}N-sphingolipid precursors for 6 d were also characterized to permit comparison to the steady state sphingolipid organization. To help ensure that the cells are able to rapidly utilize the ^{15}N-sphingoid bases for sphingolipid biosynthesis while maintaining sphingolipid homeostasis, the cells were cultured in the presence of unlabeled sphingoid bases for 6 d prior to pulse labeling.

Liquid chromatography-mass spectrometry (LC-MS) measurements revealed a gradual increase in ^{15}N-sphingoid base incorporation into *N*-palmitoyl sphingomyelin, the most abundant cellular sphingolipid (Table 4.1). These measurements indicated that the ^{15}N-sphingoid base was incorporated into approximately 8% of the *N*-palmitoyl sphingomyelin detected in cells that were pulse-labeled for 30 min, 1 h, and 2 h. However, these ^{15}N-incorporation levels are likely overestimated because it is difficult to remove the contributions of unlabeled lipid species from the peaks that are used to quantify the ^{15}N-sphingomyelin species when the ^{15}N-incorporation is low. The ^{15}N-incorporation gradually increased from approximately 8% to 37% as the pulse labeling interval increased from 2 to 24 h (Table 4.1). In comparison, ^{15}N-incorporation into the

N-palmitoyl sphingomyelin was 89% in the cells that had been pulse labeled for 6 d. Thus, these results suggest that under these conditions, the majority of the cellular sphingolipids were either degraded to non-sphingolipid products between 24 h and 6 d.

The relative ^{15}N-sphingolipid abundance within the plasma membrane was assessed by using high-resolution SIMS to measure the ^{15}N-enrichment, which is the number of times the ^{15}N-enrichment is greater than the standard abundance ratio (0.00367), on the cell surface (top ≤5 nm). The mean ^{15}N-enrichment measured in the plasma membranes of the labeled cells gradually increased from 2.4 to 19.7 as the pulse labeling time increased from 0.5 h to 6 d. The slight decrease in the mean ^{15}N-enrichment measured in the plasma membrane observed when the pulse labeling time increased from 12 to 24 h likely indicates the label abundance in the extracellular media, which was added to the culture every 24 h, had become depleted by the end of the 24 h labeling period.

Characteristics of the Individual ^{15}N-Sphingolipid Microdomains Produced by Various Pulse Labeling Times

The ^{15}N-enrichment images acquired with high-resolution SIMS revealed domains of elevated ^{15}N-sphingolipid distribution in the plasma membrane after each pulse labeling time (Figure 4.1). Visual inspection of the images suggested that the ^{15}N-enrichment, and thus ^{15}N-sphingolipid abundance, within the domains generally increased with pulse labeling time. Quantitative analysis of the SIMS images (see Materials and Methods for details) confirmed this deduction. Though the mean ^{15}N-enrichment measured in the ^{15}N-sphingolipid domains and nondomain regions on the cells were highly variable at all labeling times, they generally increased as the pulse labeling time increased up to 12h (Table 4.1). In contrast, the microdomains' sizes and abundances on the cell surface were less dependent on the pulse

labeling time. The mean effective diameter, which is defined as the diameter of a circular domain with the same area, of the ^{15}N-sphingolipid domains increased as the pulse labeling time increased from 30 min to 2 h. However, only small increases in domain size were observed as the pulse labeling time increased beyond 2 h (Table 4.1). Pulse labeling time did not seem to affect the percentage of the cell's surface that was covered by sphingolipid-enriched microdomains, which was between approximately 10 to 15% for all labeling times. Altogether, these data suggest that within 2 h, nearly all of the sphingolipid domains in the plasma membrane contained a mixture of newly synthesized ^{15}N-sphingolipids and pre-existing, endogenous (naturally abundant nitrogen-14 containing) sphingolipids.

Effects of Pulse Labeling Time on ^{15}N-Sphingolipid Microdomain Organization

Established statistical methods for point pattern analysis[12,19,20] were used to assess whether the duration of ^{15}N-sphingolipid precursor incorporation into the cells affected the organization of the ^{15}N-sphingolipid microdomains in the plasma membrane. The coordinates for the centers of the ^{15}N-sphingolipid microdomains with respect to the surface of each cell were tabulated, and then a modified Ripley's K-test was performed to assess whether the microdomain organization deviated from a random distribution.[12,19] Figure 4.2A shows the average Ripley's K-test statistic, L(r) – r, for 3 to 6 cells that were pulse labeled for the indicated duration as a function of radial distance; the plots were normalized so that the 99% confidence interval (99% CI) equals one. For all labeling times, the average L(r) – r was larger than the 99% CI at radial distances between ~0.2 and the longest accessible length scale (~3 μm), indicating the ^{15}N-sphingolipid microdomains were non-randomly clustered over this distance.

To examine whether the pulse labeling time influenced the ^{15}N-sphingolipid microdomain clustering, we compared the frequencies of domain-domain distances for the

microdomains observed on the pulse labeled cells to those for simulated populations of randomly positioned domains. The nearest neighbor (NN) distance, which is the distance between the center of each domain and that of its closest neighbor, provides information on the short-range microdomain organization. Figure 4.2B shows the average differences between the frequencies of observed and simulated NN distances that were calculated using data from 3 – 6 cells that were pulse labeled for the indicated time. For all labeling times, NN distances of 200 nm occurred more frequently than expected for randomly positioned microdomains. Because the average microdomain diameters were between 130 to 180 nm, the microdomains were nearly touching their nearest neighbor.

The pairwise domain (PD) distances, which are the distances between the center of each sphingolipid microdomain and every other microdomain on the cell, provides information on whether the sphingolipid microdomains form larger clusters in the plasma membrane. For each labeling time, the frequencies of observed and simulated PD distances were tabulated using data from 15 μm by 15 μm regions on 2 – 4 cells, and the average difference between the frequencies of observed and simulated PD distances was calculated over then range of 0 to 20 μm. The trends in the plots of the average fractional difference in the observed and simulated PD distances reveal modest changes in sphingolipid microdomain organization in the cells measured for 4 h or less versus those labeled for longer durations (Figure 4.2C). For cells pulse labeled for 4 h or less, PD distances in the range of 0.5 to 5 μm and also 10 to 18 nm occurred more frequently than expected for a randomly distributed population, whereas PD distances between 5 and 10 μm occurred less frequently than expected. This indicates the sphingolipid microdomains in the plasma membranes of cells that were pulse-labeled for no more than 4 h were nonrandomly clustered within membrane regions that were roughly 5 μm across, and these

patches of microdomains were separated from one another by approximately 10 – 18 μm. In comparison, for cells that were pulse labeled for at least 8 h the difference in the observed and simulated PD distances were generally positive at distances of 0.5 to 6 μm, somewhat negative at distances of 9 to 15 μm, and near zero at distances of 16 – 20 μm. These data suggest that the sphingolipid microdomains nonrandomly clustered within marginally larger membrane patches that were slightly more separated from each other when the pulse labeling increased to 8 h. Altogether, these results indicate both the short and long range sphingolipid distribution within the plasma membrane occurs very rapidly.

Discussion

Our data indicates sphingolipid organization in the plasma membrane arises from the effects of the cytoskeleton and intracellular traffic, specifically that of the cortical actin and its associated proteins establishing diffusion barriers that sustain local concentration gradients produced by vesicle fusion.[13] Consequently, the fusion of transport vesicles that move newly synthesized sphingolipids from the Golgi to the plasma membrane produces local elevations in sphingolipid abundance within the plasma membrane.

De novo sphingolipid biosynthesis begins in the endoplasmic reticulum with the condensation of serine and palmitoyl-CoA. Ensuing steps in the endoplasmic reticulum yield the sphingoid base, sphinganine, which is converted to ceramide. The ceramide is then transported to the Golgi, where it is converted to complex sphingolipids, including sphingomyelin and glycosphingolipids. These sphingolipid products are packaged into vesicles that are transported to the plasma membrane. The fusion of these sphingolipid-rich vesicles with the plasma membrane would then produce local elevations in sphingolipid abundance. These elevations persist due to the diffusion barriers established by a dense network of transmembrane proteins

that are tethered to the underlying cytoskeleton. Sphingolipids in the plasma membrane are internalized to endososomes where they can be transported back to the plasma membrane, or degraded in lysosomes. Sphingolipids that are recycled back to the plasma membrane may utilize a direct route, or they may be first sent to the Golgi where they would be packaged into transport vesicles that also contain newly synthesized sphingolipids, and then trafficked together to the plasma membrane. Alternatively the sphingolipids that are destined for degradation in lysosomes are broken down to sphingosine. Although sphingosine is not produced in the *de novo* sphingolipid biosynthesis pathway, the resulting sphingosine can be transported to the endoplasmic reticulum, and reutilized for sphingolipid biosynthesis via the salvage pathway.

In this work, only the sphingolipids that contain the ^{15}N-sphingoid backbone could be detected with high-resolution SIMS. Our findings of little change in either the fraction of the cell membrane's surface that was covered with ^{15}N-sphingolipid microdomains, or the size of these ^{15}N-sphingolipid microdomains indicates most sphingolipids in the plasma membrane were endocytosed, transported to intracellular compartments where they mixed with newly synthesized sphingolipids, and then returned to the plasma membrane. Once returning to the plasma membrane, vesicles containing these newly synthesized sphingolipids formed statistically significant (as determined using the MATLAB Statistics Toolbox^{TM}) and non-randomly clustered sphingolipid domains (calculated using Ripley's K-test). This non-random distribution was also confirmed when evaluating the nearest neighbor (NN) distances of the observed sphingolipid domains at which point it was determined that most domains were nearly touching their nearest neighbot. Finally, steady state distribution in the plasma membrane was assessed by comparing the pairwise domain distances; results indicate that both the short and long range sphingolipid distribution within the plasma membrane is established very quickly.

The use of high-resolution SIMS in conjunction with a pulse-labeling of cellular sphingolipids provided us with a better understanding of the analyzed murine fibroblast cells. New insight was gained in terms of the speed in which these cells will turnover their membrane surface (noticeable changes occurring within 30 min). This work also points towards the importance of vesicle transport within domain formation since the primary path for sphingolipid delivery to the plasma membrane is via vesicles.[21,22] The appearance of sphingolipid domains at all of our time points indicates that large portions of newly synthesized sphingolipids are quickly delivered to the plasma membrane, possibly in vesicles that fuse to adjacent regions within the plasma membrane. While unique insight has been gained towards better understanding sphingolipid delivery into domains, further studies will need to be conducted in order to fully understand the role that vesicle transport plays in the formation of sphingolipid domains.

References

(1) Doherty, G. J.; McMahon, H. T. Mediation, Modulation, and Consequences of Membrane-Cytoskeleton Interactions. *Annu. Rev. Biophys.* **2008**, *37* (1), 65–95.

(2) Holthuis, J. C. M.; Levine, T. P. Lipid Traffic: Floppy Drives and a Superhighway. *Nat. Rev. Mol. Cell Biol.* **2005**, *6* (3), 209–220.

(3) Shaw, J. E.; Epand, R. F.; Epand, R. M.; Li, Z.; Bittman, R.; Yip, C. M. Correlated Fluorescence-Atomic Force Microscopy of Membrane Domains: Structure of Fluorescence Probes Determines Lipid Localization. *Biophys. J.* **2006**, *90* (6), 2170–2178.

(4) Zhang, J.; Pekosz, A.; Lamb, R. A. Influenza Virus Assembly and Lipid Raft Microdomains: A Role for the Cytoplasmic Tails of the Spike Glycoproteins. *J. Virol.* **2000**, *74* (10), 4634–4644.

(5) Eggeling, C.; Ringemann, C.; Medda, R.; Schwarzmann, G.; Sandhoff, K.; Polyakova, S.; Belov, V. N.; Hein, B.; von Middendorff, C.; Schoenle, A.; et al. Direct Observation of the Nanoscale Dynamics of Membrane Lipids in a Living Cell. *Nature* **2009**, *457* (7233), 1159–U121.

(6) Shnyrova, A. V.; Frolov, V. A.; Zimmerberg, J. Domain-Driven Morphogenesis of Cellular Membranes. *Curr. Biol.* **2009**, *19* (17), R772–R780.

(7) Simons, K.; Toomre, D. Lipid Rafts and Signal Transduction. *Nat. Rev. Mol. Cell Biol.* **2000**, *1* (1), 31–39.

(8) Takeda, M.; Leser, G. P.; Russell, C. J.; Lamb, R. A. Influenza Virus Hemagglutinin Concentrates in Lipid Raft Microdomains for Efficient Viral Fusion. *Proc. Natl. Acad. Sci.* **2003**, *100* (25), 14610–14617.

(9) Radhakrishnan, K.; Halasz, A.; Vlachos, D.; Edwards, J. S. Quantitative Understanding of Cell Signaling: The Importance of Membrane Organization. *Curr. Opin. Biotechnol.* **2010**, *21* (5), 677–682.

(10) Jacobson, K.; Mouritsen, O. G.; Anderson, R. G. W. Lipid Rafts: At a Crossroad between Cell Biology and Physics. *Nat. Cell Biol.* **2007**, *9* (1), 7–14.

(11) Frisz, J. F.; Lou, K.; Klitzing, H. A.; Hanafin, W. P.; Lizunov, V.; Wilson, R. L.; Carpenter, K. J.; Kim, R.; Hutcheon, I. D.; Zimmerberg, J.; et al. Direct Chemical Evidence for Sphingolipid Domains in the Plasma Membranes of Fibroblasts. *Proc. Natl. Acad. Sci.* **2013**, *110* (8), E613–E622.

(12) Frisz, J. F.; Klitzing, H. A.; Lou, K.; Hutcheon, I. D.; Weber, P. K.; Zimmerberg, J.; Kraft, M. L. Sphingolipid Domains in the Plasma Membranes of Fibroblasts Are Not Enriched with Cholesterol. *J. Biol. Chem.* **2013**, *288* (23), 16855–16861.

(13) Kusumi, A.; Nakada, C.; Ritchie, K.; Murase, K.; Suzuki, K.; Murakoshi, H.; Kasai, R. S.; Kondo, J.; Fujiwara, T. Paradigm Shift of the Plasma Membrane Concept from the Two-Dimensional Continuum Fluid to the Partitioned Fluid: High-Speed Single-Molecule Tracking of Membrane Molecules. In *Annual Review of Biophysics and Biomolecular Structure*; Annual Reviews: Palo Alto, 2005; Vol. 34, pp 351–U54.

(14) Garner, P.; Park, J. M.; Malecki, E. A Stereodivergent Synthesis of D-Erythro-Sphingosine and D-Threo-Sphingosine from L-Serine. *J. Org. Chem.* **1988**, *53* (18), 4395–4398.

(15) Dondoni, A.; Perrone, D. Synthesis of 1,1-Dimethylethyl (S)-4-Formyl-2,2-Dimethyl-3-Oxazolidinecarboxylate by Oxidation of the Alcohol. In *Organic Syntheses*; John Wiley & Sons, Inc., 2003.

(16) Peters, C.; Billich, A.; Ghobrial, M.; Högenauer, K.; Ullrich, T.; Nussbaumer, P. Synthesis of Borondipyrromethene (BODIPY)-Labeled Sphingosine Derivatives by Cross-Metathesis Reaction. *J. Org. Chem.* **2007**, *72* (5), 1842–1845.

(17) Klitzing, H. A.; Weber, P. K.; Kraft, M. L. Secondary Ion Mass Spectrometry Imaging of Biological Membranes at High Spatial Resolution. In *Nanoimaging*; Sousa, A. A., Kruhlak, M. J., Eds.; Humana Press: Totowa, NJ, 2013; pp 483–501.

(18) Bligh, E. G.; Dyer, W. J. A Rapid Method of Total Lipid Extraction and Purification. *Can. J. Biochem. Physiol.* **1959**, *37* (8), 911–917.

(19) Hess, S. T.; Kumar, M.; Verma, A.; Farrington, J.; Kenworthy, A.; Zimmerberg, J. Quantitative Electron Microscopy and Fluorescence Spectroscopy of the Membrane Distribution of Influenza Hemagglutinin. *J. Cell Biol.* **2005**, *169* (6), 965–976.

(20) Zhang, J.; Leiderman, K.; Pfeiffer, J. R.; Wilson, B. S.; Oliver, J. M.; Steinberg, S. L. Characterizing the Topography of Membrane Receptors and Signaling Molecules from Spatial Patterns Obtained Using Nanometer-Scale Electron-Dense Probes and Electron Microscopy. *Micron* **2006**, *37* (1), 14–34.

(21) Gheber, L. A.; Edidin, M. A Model for Membrane Patchiness: Lateral Diffusion in the Presence of Barriers and Vesicle Traffic. *Biophys. J.* **1999**, *77* (6), 3163–3175.

(22) Klemm, R. W.; Ejsing, C. S.; Surma, M. A.; Kaiser, H.-J.; Gerl, M. J.; Sampaio, J. L.; Robillard, Q. de; Ferguson, C.; Proszynski, T. J.; Shevchenko, A.; et al. Segregation of Sphingolipids and Sterols during Formation of Secretory Vesicles at the Trans-Golgi Network. *J. Cell Biol.* **2009**, *185* (4), 601–612.

Figures and Tables

Pulse-labeling time	0.5 h	1 h	2 h	4 h	8 h	12 h	24 h	6 d
Mean ± 1 s.d. (%) ^{15}N-incorporation in *N*-palmitoyl sphingomyelin (LC-MS)	8.6 ± 6.2	8.1 ± 4.1	7.7 ± 0.0*	13.5 ± 1.4	19.9 ± 3.5	27.5 ± 0.6	36.5 ± 8.7	88.5 ± 4.4
Mean ± 1 s.d. ^{15}N-enrichment in plasma membrane (SIMS)	2.4 ± 0.5	2.8 ± 0.3	4.0 ± 1.0	3.6 ± 1.0	6.0 ± 1.3	9.0 ± 1.4	7.6 ± 1.3	8.6 ± 0.8
Mean ± 1 s.d. ^{15}N-enrichment in sphingolipid domains (SIMS)	6.9 ± 2.0	7.6 ± 1.5	9.1 ± 2.2	7.4 ± 2.4	10.9 ± 2.9	17.2 ± 4.4	14.1 ± 2.5	19.7 ± 3.9
Mean ± 1 s.d. ^{15}N-enrichment in non-domain areas (SIMS)	2.2 ± 0.4	2.5 ± 0.3	3.4 ± 0.7	3.1 ± 1.0	5.1 ± 1.6	7.4 ± 1.3	6.6 ± 1.5	7.1 ± 1.0
Mean ± 1 s.d. (nm) effective domain diameter	132 ± 10	137 ± 5	158 ± 21	149 ± 16	152 ± 18	168 ± 21	179 ± 6.6	171 ± 11
Mean ± 1 s.d. (%) surface coverage of ^{15}N-sphingolipid domains	13.4 ± 3.7	12.7 ± 3.1	14.9 ± 1.4	11.6 ± 3.2	9.9 ± 2.4	12.0 ± 4.9	14.3 ± 4.6	15.1 ± 5.5

*1 s.d. < 0.1

Table 4.1 Comparison of sphingolipid incorporation with respect to time

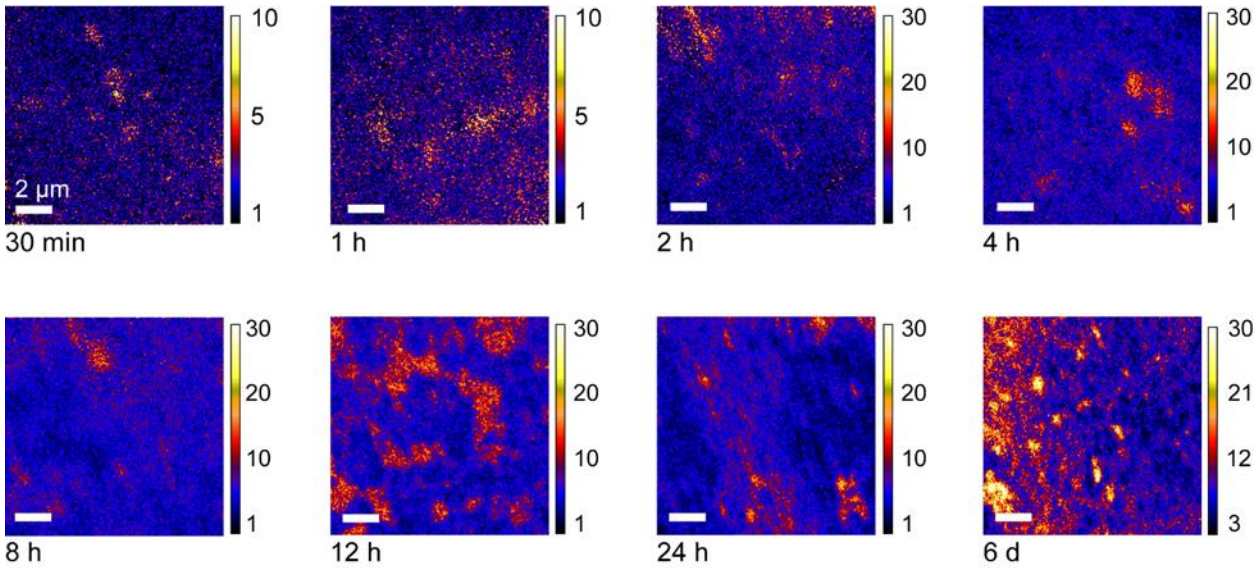

Figure 4.1 The ^{15}N-enrichment images acquired with high-resolution SIMS at each pulse labeling time. Images revealed statistically significant domains of elevated ^{15}N-sphingolipid after each pulse labeling time

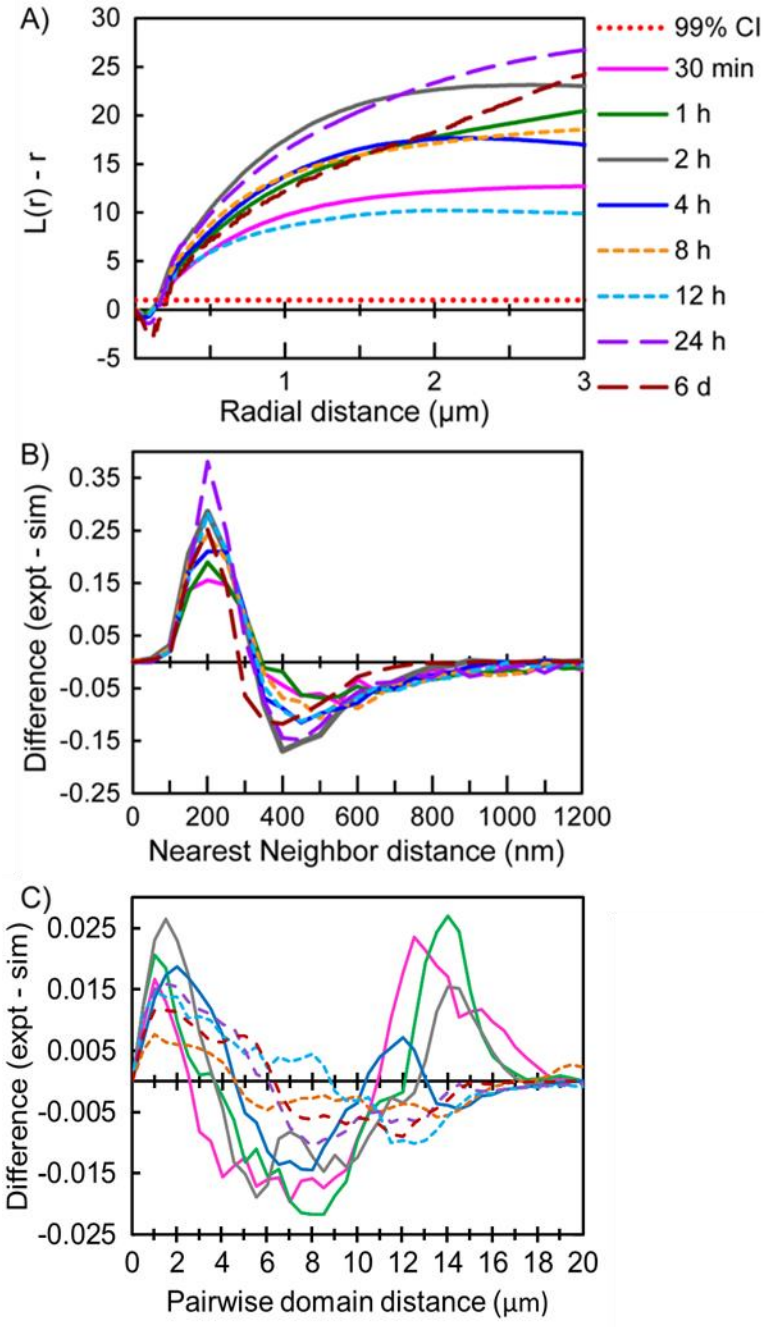

Figure 4.2 Analysis of sphingolipid domain organization on the plasma membranes of cells isotopically labeled for varying lengths of time. (A) The average Ripley's K-test statistic, L(r) – r. Lengths at which L(r) – r was larger than the 99% CI indicates non-random clustering over this distance; (B) Plots of the average differences between the frequencies of observed and simulated nearest neighbor distances. A value larger than 0 indicates domains occurring more frequently than expected at that distance; (C) Plots of the average fractional difference in the observed and simulated pairwise domain distances. Values that deviate from 0 indicate domains occurring more frequently than expected at that distance.

CHAPTER 5.
FINAL OBSERVATIONS, CONCLUSIONS, AND FUTURE OBJECTIVES

Notes and Acknowledgements

The "Final Observations" portion of this chapter describes unpublished work. Mary L. Kraft planned experiments, assisted with NanoSIMS analysis, developed MATLAB-based statistical tools for data analysis, and assisted with data interpretation. Haley A. Klitzing planned and performed experiments, performed NanoSIMS analysis, data analysis, and data interpretation. Peter K. Weber assisted with experimental design, NanoSIMS analysis, and data interpretation. We thank A. Ulanov for his valuable comments on the evaluation of isotope incorporation and L. Nittler for software development. MLK holds a Career Award at the Scientific Interface from the Burroughs Wellcome Fund. Portions of this work were carried out in the Metabolomics Center in the Roy J. Carver Biotechnology Center, Univ. of Illinois, and in the Frederick Seitz Materials Research Laboratory Central Facilities, Univ. of Illinois, which are partially supported by the U.S. Department of Energy (DOE) under grants DE-FG02-07ER46453 and DE-FG02-07ER46471. Work at Lawrence Livermore National Laboratory was supported by Laboratory Directed Research and Development funding and performed under the auspices of the U.S. DOE under contract DE-AC52-07NA27344. This material was supported in part by the National Science Foundation under CHE—1058809.

Final Observations

Clearly more studies must be performed to understand the complete role that vesicle traffic plays in the formation of sphingolipid domains. Initial work has been done using two types of disruption drugs: brefeldin A (BFA), which has been shown to halt trafficking at the Golgi apparatus;[1] and nocodazole, which has been shown to depolymerize microtubules important for vesicle transport.[2]

Methods and Materials

The NIH3T3 mouse fibroblast cells were obtained from ATCC CRL-1658™. Initial cell growth medium (Media A) consisted of high glucose Dulbecco's modified Eagle's medium (DMEM) supplemented with 10% Hyclone calf serum (Fisher Scientific), 10^4 U/mL penicillin G, and 10 mg/mL streptomycin. During the second stage of cell growth, the medium (Media B) consisted of high glucose DMEM supplemented with 10% Hyclone lipid-reduced fetal bovine serum and 1% Hyclone calf serum (Fisher Scientific). A fatty acid solution (^{13}C-fatty acids) made from algal lipid mixture (uniformly carbon-13 labeled, UL-^{13}C, 98%+) (Cambridge Isotope Laboratories, Inc.), stearic acid ($^{13}C_{18}$, 99 atom% ^{13}C) (Isotec), and fatty acid free bovine serum albumin (FAF-BSA) was used to metabolically label all cellular lipids as described in previous chapters. The ^{15}N-sphingoid bases, 1:1 molar ratio of ^{15}N-sphingosine and ^{15}N-sphinganine, used to isotopically label sphingolipids were synthesized as detailed in previous chapters. Metabolic labeling was performed as described in previous chapters.

Following metabolic labeling, cells were attached to silicon substrates (5 x 5 mm) (Ted Pella, Inc.) as described in previous chapters to enable sample analysis. Substrates with adherent cells were then divided into separate dishes functioning as either control or experimental treatments. One set of the sample substrates acted as controls and were placed in media

containing equal amounts of dimethyl sulfoxide as the experimental conditions. A second set of substrates was placed in media containing 10 μg/mL of nocodazole (Sigma) where they were incubated for 2 h before being removed and chemically fixed. The last set of substrates was placed in media containing 1 μg/mL of BFA (Biolegend) where they were incubated for 2 h before being removed and chemically fixed.

Chemical fixation of the cells was performed with glutaraldehyde and osmium tetroxide (Electron Microscopy Sciences) as previously described. Lipid extraction followed by sample separation and mass spectrometry (MS) was performed as described in previous chapters using an Agilent 1100 LC/MSD Trap XCT Plus equipped with a Phenomenex Gemini 3u C6-Phenyl 110A column (2 x 100 mm) (LC-MS) and an Agilent 6890 gas chromatograph with a ZB-WAX (30 m × 0.25 mm I.D., 0.25 μm film thickness) capillary column (Phenomenex, Torrance, CA, USA), an Agilent 5973 mass selective detector and HP 7683B (Agilent Inc, Palo Alto, CA, USA) autosampler (GC-MS).

Low voltage secondary electron microscopy (SEM) was performed on a Hitachi S-4800 SEM followed by samples being imaged with Cameca's NanoSIMS 50. Instrumental analysis and data analysis (including the use of L'Image and MATLAB) was performed as described in previous chapters.

Results

In these experiments, metabolically labeled cells were exposed to one of the drug treatments prior to fixation and NanoSIMS analysis. Although treatment with BFA showed no noticeable changes in cell morphology (Fig. 5.1), NanoSIMS imaging showed marked changes in membrane sphingolipid distribution (Fig. 5.2). It appears there are fewer (if any) sphingolipid

domains on the cell's surface. However, further experiments are required to confirm reproducibility of these results.

Initial experiments were also performed to examine the defects of depolymerizing the microtubules that are required for vesicle transport using nocodazole. Metabolically labeled cells exposed to nocodazole showed very slight rounding (Fig. 5.3). This is presumably due to structural changes in the cellular cytoskeleton when the microtubules were depolymerized. The sphingolipid distribution appeared similar to what had been observed in the BFA-treated cells (Fig. 5.4), specifically, lower sphingolipid content in the plasma membrane and fewer sphingolipid domains. This is consistent with the hypothesis that vesicle transport plays a role in sphingolipid organization in the plasma membrane. However, further experiments are needed to confirm these preliminary results and elucidate their full meaning.

Conclusions and Future Objectives

During the course of this work, we've established a protocol for using high resolution imaging secondary ion mass spectrometry (SIMS) to examine the distribution of specific lipid species in the plasma membranes of cells. Using this technique, we successfully visualized the locations of sphingolipids on the plasma membrane, and found that they are nonrandomly organized within domains. We also explored the cause behind the formation of these sphingolipid domains. We found that the formation of these domains requires an intact cytoskeleton, and vesicle trafficking seems to be involved.

The body of work described in Chapter 2 describes the technique development for using high resolution imaging SIMS to visualize sphingolipids in the plasma membranes of mammalian cells with a lateral resolution better than 100 nm. Precise incorporation of distinct isotope labels into plasma membrane components of interest, namely specific lipid species,

enables the direct analysis of their organization in the cell membrane. This facilitates answering questions related to membrane organization and its functional consequences, which have thus far evaded researchers.

Chapter 3 discussed the use of these high resolution SIMS techniques to evaluate the presence of sphingolipid domains on the cell surface. Use of the NanoSIMS confirmed a heterogeneous plasma membrane featuring regions with statistically significant local elevations of sphingolipids (domains) in comparison to the rest of the plasma membrane. These domains had an average diameter of 200 nm and were primarily organized in micron-sized clusters or patches. Disrupting the cytoskeleton of the cell resulted in the dispersal of these sphingolipid domains, implying that an intact cytoskeleton is necessary for the sphingolipid microdomains to be present. This set of studies has helped redefine our understanding of plasma membrane organization and has turned the tides in the "lipid raft"[3] controversy[4] by helping to disprove the concept.[5] These studies also helped confirm the importance that an intact cytoskeleton plays in the formation of sphingolipid microdomains, and leads to the question of "What role does vesicle traffic play?" Our work in Chapter 4 and initial work in Chapter 5 has looked at this.

In an effort to visualize the vesicle trafficking of sphingolipids to the plasma membrane, a pulse-labeling experiment was performed in Chapter 4. This study showed rapid incorporation of isotope labels into the sphingolipids in the plasma membrane, indicating a very fast turnover rate. Statistically significant domains were detectable in the cells imaged after only 30 min of labeling. When comparing isotope incorporation in the bulk of the cell to that of the plasma membrane, it appears as though much of the newly synthesized sphingolipids are rapidly transported to the plasma membrane. This incorporation into the membrane was successfully visualized with the NanoSIMS. Also, at the beginning of this chapter we showed preliminary

results suggesting that the disruption of vesicle transport plays a role in the appearance of sphingolipids within domains.

Altogether, we developed a technique for using high resolution SIMS to study sphingolipids within the plasma membrane. This resulting technique then allowed steps to be taken towards determining how these sphingolipids form domains. An intact cytoskeleton appears to be essential. Results also suggest that vesicle trafficking of these sphingolipids to the membrane is done rapidly and may be essential to the formation of domains. More studies will be needed to understand the role of membrane transport on sphingolipid domain formation, but this technique can be combined with conventional biochemistry and biochemical methods to gain said knowledge. A drawback of these studies is that the drug treatments performed could have unknown effects on the cell and its membrane organization. Additional studies will need to address whether the observed sphingolipid organizations are a side effect of drug treatment, or if they are representative of the native cell function. Once the complete role of vesicle transport on sphingolipid domains is discovered we will have a more complete understanding of the formation of these sphingolipid domains on the plasma membrane; knowledge which will allow the scientific community to better control and manipulate the plasma membrane throughout its extensive interactions with its environment.

References

(1) Miller, S. G.; Carnell, L.; Moore, H. H. Post-Golgi Membrane Traffic: Brefeldin A Inhibits Export from Distal Golgi Compartments to the Cell Surface but Not Recycling. *J. Cell Biol.* **1992**, *118* (2), 267–283.

(2) Breitfeld, P. P.; McKinnon, W. C.; Mostov, K. E. Effect of Nocodazole on Vesicular Traffic to the Apical and Basolateral Surfaces of Polarized MDCK Cells. *J. Cell Biol.* **1990**, *111* (6), 2365–2373.

(3) Pike, L. J. Rafts Defined: A Report on the Keystone Symposium on Lipid Rafts and Cell Function. *J. Lipid Res.* **2006**, *47* (7), 1597–1598.

(4) Leslie, M. Do Lipid Rafts Exist? *Science* **2011**, *334* (6059), 1046–1047.

(5) Kraft, M. L. Plasma Membrane Organization and Function: Moving Past Lipid Rafts. *Mol. Biol. Cell* **2013**, *24* (18), 2765–2768.

Figures

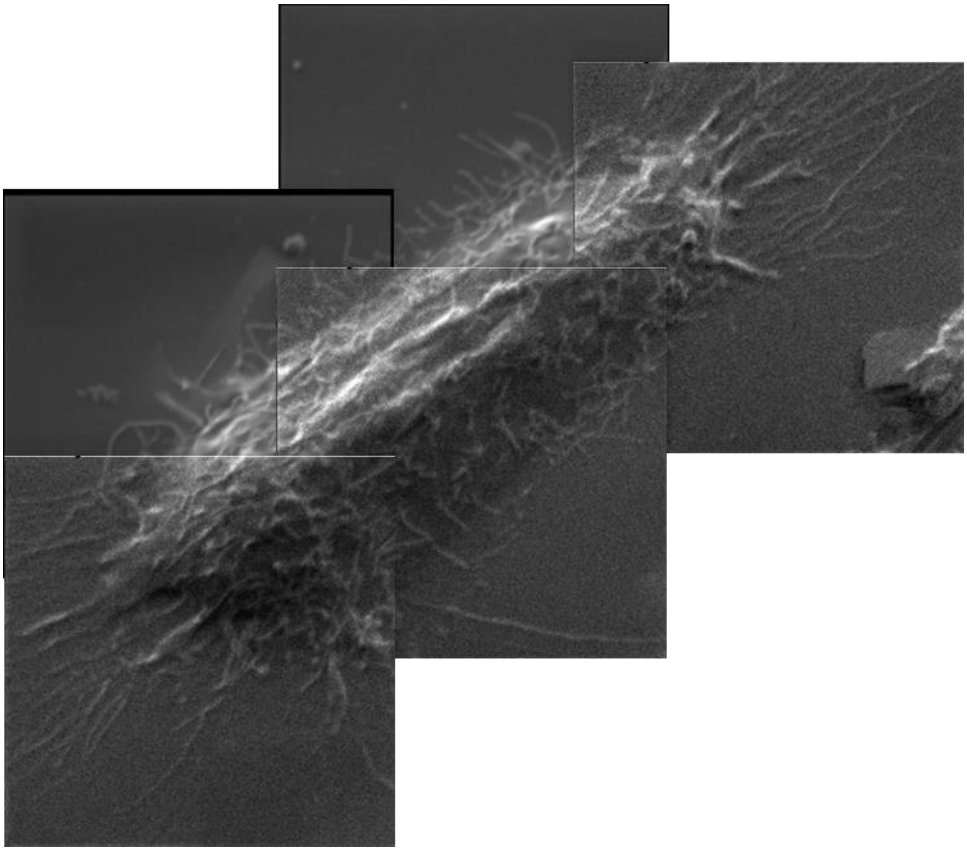

Figure 5.1 Secondary electron image of a murine fibroblast cell disrupted with BFA.

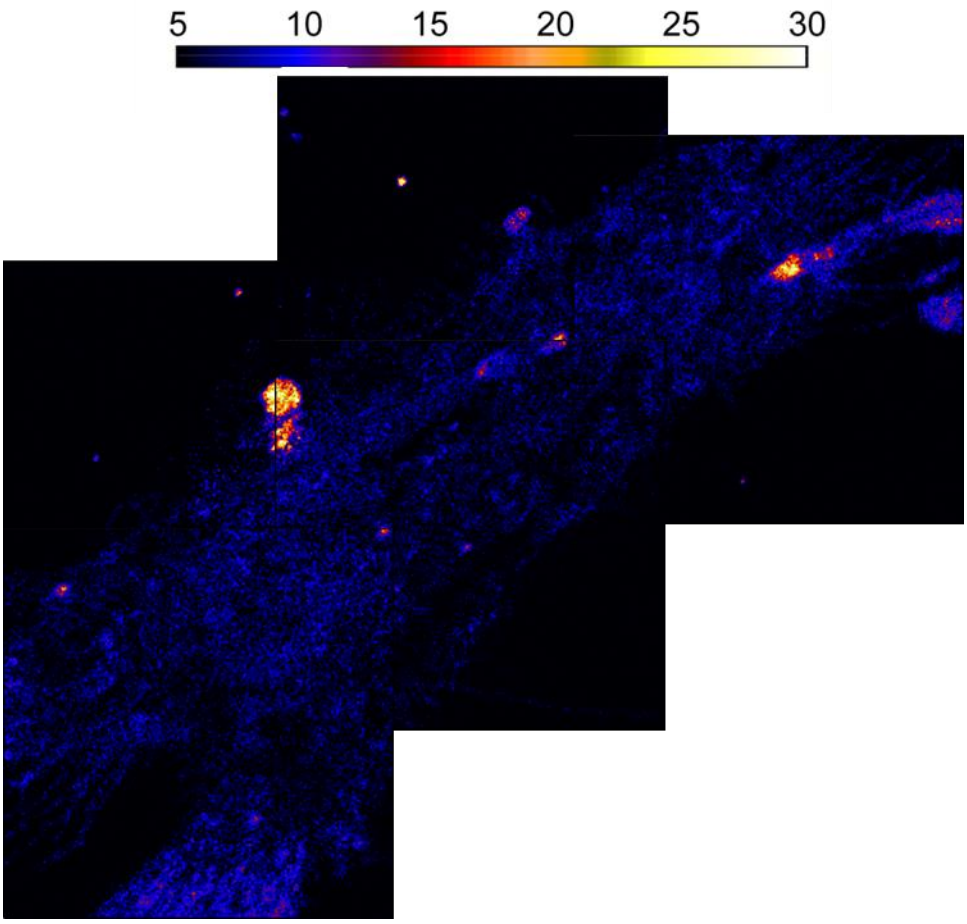

Figure 5.2 ^{15}N-Enrichment image of a murine fibroblast cell disrupted with BFA. Sphingolipid abundance is lower, and the existence of sphingolipid domains is difficult to determine compared to previously analyzed non-drug treated cells.

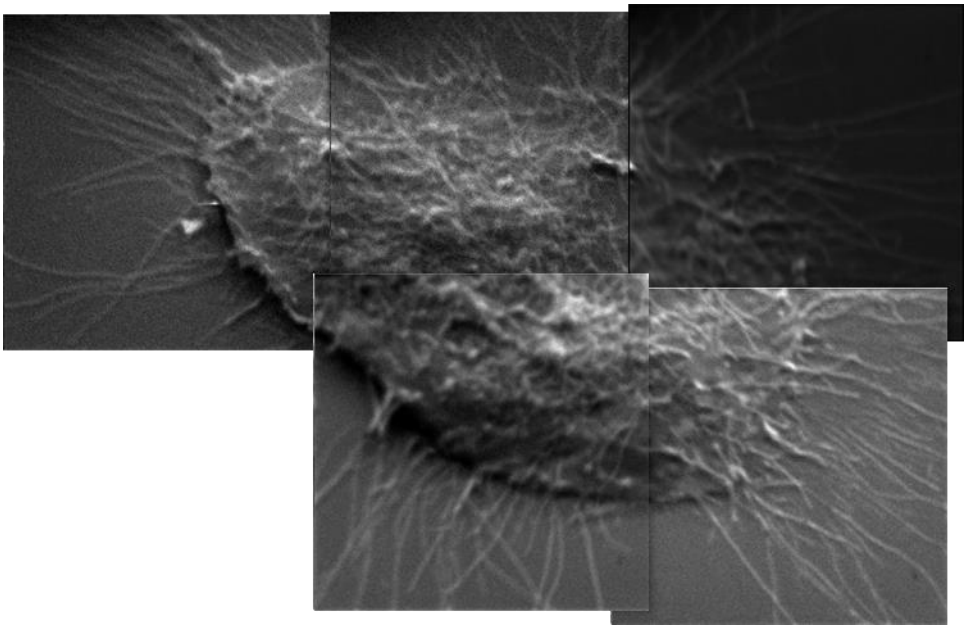

Figure 5.3 Secondary electron image of a murine fibroblast cell disrupted with nocodazole.

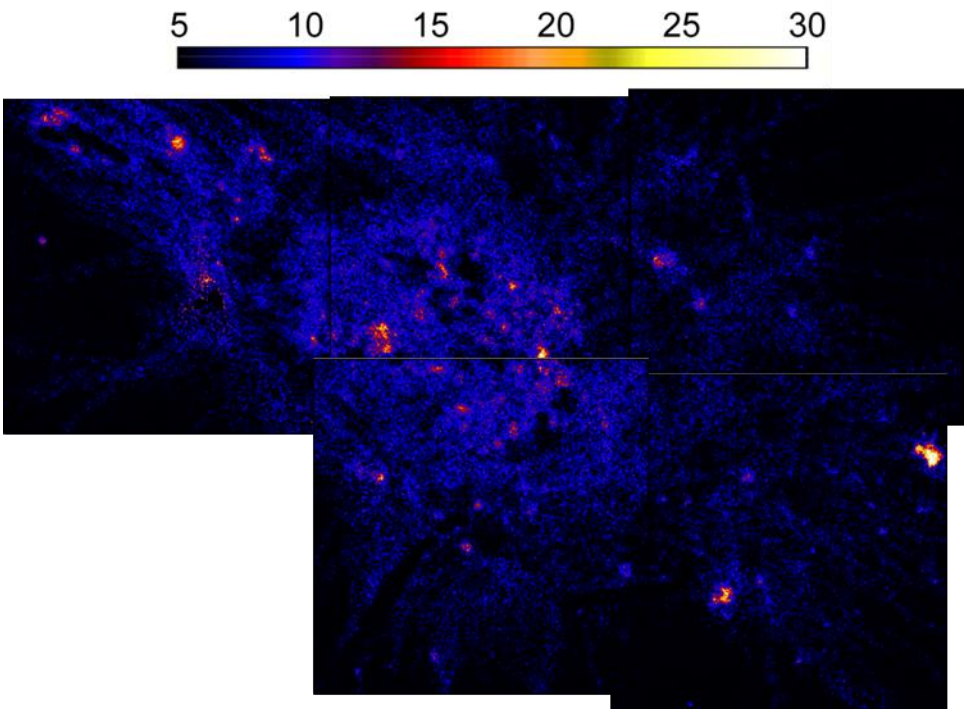

Figure 5.4 ^{15}N-Enrichment image of a murine fibroblast cell disrupted with nocodazole. Sphingolipid abundance is lower, and the prevalence of sphingolipid domains appears to be lower than previously analyzed non-drug treated cells.